Débora de Souza António

Bachelor of Science

Dose assessment and reconstruction algorithm optimization in simultaneous breast and lung CT imaging

Dissertation submitted in partial fulfillment
of the requirements for the degree of

Master of Science in
Biomedical Engineering

Adviser: Phd. Salvatore Di Maria, Researcher, Centre for Nuclear Sciences and Technologies - C2TN

Co-advisers: Phd. Nuno Miguel de Pinto Lobo e Matela, Associate Professor, Faculty of Science of University of Lisbon

Phd. José Pedro Miragaia Trancoso Vaz, Main Researcher, Center for Nuclear Sciences and Technologies - C2TN

Examination Committee

Chairperson: Phd. Carla Maria Quintão Pereira, Auxiliar Professor, FCT - UNL
Raporteurs: Phd. Susana Evaristo Oliveira Branco, Adjunct Professor, ESTeSL
Phd. Salvatore Di Maria, Researcher, C2TN

FACULDADE DE
CIÊNCIAS E TECNOLOGIA
UNIVERSIDADE NOVA DE LISBOA

September, 2018

Dose assessment and reconstruction algorithm optimization in simultaneous breast and lung CT imaging

This document was created using the (pdf)LaTeX processor, based in the "novathesis" template[1], developed at the Dep. Informática of FCT-NOVA [2].
[1] https://github.com/joaomlourenco/novathesis [2] http://www.di.fct.unl.pt

Aos meus pais, Fernando e Dalva António
e à minha avó Maria Alcine Fernandes

Acknowledgements

First of all, I would like to express my profound gratitude to my adviser, Salvatore Di Maria and co-adviser, Nuno Matela, for their patience, dedication and efforts in bringing this dissertation project to existence. Not only would this investigation not exist without them, but the synergy of their combined skills, expertise, and insights was crucial at every stage of the development of this project.

I would also like to express my sincere gratitude to my co-adviser José Pedro Trancoso Vaz and Octávia Monteiro Gil for their support and assistance both in a professional and personal level. To all the colleagues whom I encountered throughout my journey to accomplish this project, namely Mariana Baptista, Ana Belchior, Yuriy Romanets and Sandra Vieira, I am thankful for the assistance and time dedicated in providing me with crucial knowledge and advice of some software programs and equipment applied throughout the project. I would like to thank the C^2TN, the *IBEB* and the Champalimaud Clinical Centre, whose collaboration enabled me to undertake a dissertation project in a field of my personal preference and that I adore.

To my father, Fernando, my mother, Dalva, and my godmother Maria Alcine, who not only endured my many absences during the development of this project, but also provided me with their total support and encouragement, I offer my most heartfelt love, appreciation and apology. I'm also profoundly grateful to my brother, Francisco, for his patience in listening to my daily problems, and for the laughs and pranks that would always make me smile. A great vote of appreciation goes to my aunt Ilda, and my uncle Mario, for their great support and thoughtful and encouraging words.

While all my fellow companions and friends with whom I've shared this journey have been very helpful and supportive, namely Jaime Teyller, Luana, Romulo, Emil, Bilena, João Pombo and Pedro Pestana, a few individuals deserve special recognition. Foremost, I'm specially grateful to my goddaughter Inalinda, for her sisterhood from the very beginning of this journey, her support and motivational words. I'm also profoundly grateful to my dear friend Joana Reis, for her companionship, and great moments of joy; to my friend Paula Concha, for the great laughs and adventures and to my friend Jorge Borbinha with whom I had the honor to initiate and complete the journey of this course.

Thank you all for making the college experience and this chapter of my life worthwhile.

"One day in retrospect, the years of struggle
will strike you as the most beautiful"
- Sigmund Freud

Abstract

Cancer is the second leading cause of death in the world, and therefore, there is an undeniable need to ensure early screening and detection systems worldwide. The aim of this project is to study the feasibility of a Cone Beam Computed Tomography (CBCT) scanner for simultaneous breast and lung imaging. Additionally, the development of reconstruction algorithms and the study of their impact to the image quality was considered.

Monte Carlo (MC) simulations were performed using the PENELOPE code system. A MC geometry model of a CBCT scanner was implemented for energies of 30 keV and 80 keV for hypothetical scanning protocols. Microcalcifications were inserted into the breast and lung of the computational phantom (ICRP Adult Female Reference), used in the simulations for dose assessment and projection acquisition. Reconstructed images were analyzed in terms of the Contrast-to-Noise Ratio (CNR) and dose calculations were performed for two protocols, one with a normalization factor of 2 mGy in the breast and another with 5 mGy in the lungs. Both, MC geometry model and reconstruction algorithm were validated by means of on-field measurements and data acquisition in a clinical center. Dosimetric and imaging performances were evaluated through Quality Assurance phantoms (Computed Tomography Dose Index and Catphan, respectively).

Results indicate that the best implementation of the reconstruction algorithm was achieved with 80 keV, using the *Hanning* filter and linear interpolation. More specifically, for a spherical lung lesion with a radius of 7 mm a 30% CNR gain was found when the number of projections varied from 12 to 36 (corresponding to a dose increase of a factor of 3).

This research suggests the possibility of developing a CBCT modulated beam scanner for simultaneous breast and lung imaging while ensuring dose reduction. However further investigation regarding the number of projections needed for image reconstruction is required.

Keywords: Cone Beam Computed Tomography, Cancer Detection, Monte Carlo Simulation, Organ Dose, Medical Image Reconstruction, Lung and Breast Imaging

Resumo

O cancro é a segunda principal causa de morte no mundo, e portanto, há uma necessidade incontestável de garantir sistemas de rastreio e de diagnóstico precoce a nível mundial. Este projeto pretende estudar a viabilidade de um exame de Tomografia Computadorizada de Feixe em Cone (CBCT) na aquisição simultânea de imagens da mama e do pulmão.

Recorrendo ao sistema de código PENELOPE, realizaram-se simulações por métodos de Monte Carlo (MC). Implementou-se um modelo de geometria de um exame de CBCT, para energias de 30 keV e 80 keV, para possíveis protocolos de aquisição de imagem. Inseriram-se microcalcificações na mama e no pulmão do fantoma computacional (de Referência do ICRP) utilizado nas simulações, para avaliação de dose e aquisição de projeções. Desenvolveram-se algoritmos de reconstrução e as imagens reconstruídas foram analisadas através da Razão Contraste-Ruído (CNR). Realizaram-se cálculos de dose para protocolos com fator de normalização de 2 mGy na mama e de 5 mGy no pulmão.

Tanto o modelo de geometria como o algoritmo de reconstrução, foram validados através de medições e aquisição de dados reais em ambiente clínico. Os desempenhos dosimétricos e de qualidade de imagem foram avaliados recorrendo a fantomas de Controlo de Qualidade (CTDI e Catphan, respetivamente).

Constatou-se que a melhor implementação do algoritmo de reconstrução foi alcançada com 80 keV. Nomeadamente, para uma lesão pulmonar esférica de raio 7 mm, alcançou-se um ganho de 30% de CNR variando o número de projeções de 12 para 36 (correspondendo ao aumento da dose de um fator de 3).

Este estudo sugere a possibilidade de se desenvolver um feixe modulado de CBCT para aquisição simultânea de imagens da mama e do pulmão, garantindo uma redução da dose administrada. É, contudo, necessária mais investigação relativamente ao número de projeções requeridas para a reconstrução da imagem.

Palavras-chave: Tomografia Computadorizada de Feixe em Cone, Deteção de Cancro, Simulações de Monte Carlo, Dose em Órgãos, Reconstrução de Imagem Médica, Imagem da Mama e do Pulmão

Contents

List of Figures xvii

List of Tables xix

Acronyms xxi

1 Motivation 1
- 1.1 Cancer Incidence and Mortality . . . 1
- 1.2 Screening and Diagnostic Methods . . . 3
  - 1.2.1 Breast Cancer . . . 3
  - 1.2.2 Lung Cancer . . . 5
- 1.3 Purpose of the project . . . 6

2 Theoretical Concepts 7
- 2.1 Cone Beam Computed Tomography . . . 7
- 2.2 X-ray Radiation . . . 9
  - 2.2.1 X-ray tubes . . . 11
  - 2.2.2 X-ray spectrum . . . 12
  - 2.2.3 Interaction of photons with matter . . . 17
  - 2.2.4 X-ray linear and mass attenuation coefficients . . . 20
  - 2.2.5 X-ray dosimetry . . . 23
- 2.3 Medical Image Reconstruction . . . 31
  - 2.3.1 Radon Transform . . . 33
  - 2.3.2 Backprojection . . . 35
  - 2.3.3 Filtered Backprojection . . . 37
  - 2.3.4 Inverse Radon Transform . . . 38
  - 2.3.5 Image Quality . . . 40

3 Methodology 41
- 3.1 Monte Carlo Methods . . . 41
  - 3.1.1 Geometrical Model Construction . . . 41
  - 3.1.2 Monte Carlo Simulations . . . 43
  - 3.1.3 Validation of the MC Simulations . . . 48

3.2 Image Reconstruction 49
3.2.1 From Projections to Reconstructed Images 49
3.2.2 Image Quality Analysis 51
3.2.3 Validation of the Reconstruction Algorithm 51

4 Results and Discussion **55**
4.1 CBCT Model Validation 55
4.1.1 MC Simulations Validation 55
4.1.2 Reconstruction Algorithm Validation 57
4.2 Acquired Projections and Reconstructed Images 58
4.3 Absorbed Dose Analysis 60
4.4 Image Quality Analysis 61

5 Conclusions and Future Work **67**

References **71**

A Detector Rotation and Source position and direction **77**
A.1 Calculations of the Detector Rotation and Positioning 77

B PenEasy files for performing the Monte Carlo Simulations **91**
B.1 PenEasy.geo File 91
B.2 PenEasy.in File 94
B.3 Description for each entry of the penEasy.in File 99

C PenEasy files for the PMMA Monte Carlo Simulations **105**
C.1 The geometry file: PMMA.geo File 105
C.2 The configuration file: PMMA.in File 110

D Code system used in the Image Reconstruction milestone **117**
D.1 Import data matrix 117
D.2 Cube data matrix 120
D.3 Division of the cube matrices 120
D.4 Reconstruction Algorithm 120

E Code system used in the validation of the reconstruction algorithm using Catphan **123**
E.1 Import data matrix file 123
E.2 Import data into cube data matrix 123
E.3 Catphan Reconstruction Algorithm 124
E.4 Catphan Algorithm for information acquisition 124

I Annex 1. List of media and their elemental compositions **125**

List of Figures

1.1 World cancer incidence by sites. 2
1.2 World cancer incidence and mortality rates. 2

2.1 Fan Beam CT vs Cone Beam CT. 8
2.2 Arc-shaped detector vs Flat panel detector 9
2.3 X-ray tube. 11
2.4 Anode focal point 13
2.5 X-Ray spectrum 13
2.6 An atom's electronic shells 14
2.7 Characteristic x-ray emission 14
2.8 Bremsstrahlung emission 15
2.9 Bremsstrahlung spectrum 16
2.10 Compton scattering 18
2.11 Mass attenuation coefficient in function of the x-ray energy 22
2.12 Standard PMMA dosimetry phantoms 28
2.13 ICRP adult male and female reference computational phantoms 31
2.14 Reconstructed axial image: voxel and pixel 32
2.15 Linear attenuation coefficient along the x-ray path 32
2.16 Fan-beam geometry and parallel-beam geometry 33
2.17 Projection data acquisition 34
2.18 Sinogram 35
2.19 Sinogram formation 35
2.20 Discrete backprojection with interpolation 36
2.21 *Ram-Lak*, block and triangle functions 38
2.22 *Ram-Lak*, *Shepp-Logan*, *Cosine* and *Hamming* Filters 39

3.1 Geometry used for Monte Carlo simulations 43
3.2 $CTDI_{100}$ simulated model and pencil ionization chamber configuration . . . 47
3.3 Gview2D: Simulated $CTDI_{100}$ measurement model 47
3.4 Cube data matix 50
3.5 Breast and lung microcalcifications and background ROI's 52
3.6 Apparatus of the Varian TrueBeam with the *Catphan 504* 52
3.7 *Catphan 504*: the CTP528 module 53

4.1 Graph of the $CTDI_{100}$ simulated values 56
4.3 Microcalcifications within the projections obtained with 80 keV 58
4.4 Microcalcifications within the projections obtained with 30 keV 59
4.5 Reconstructed axial slice vs computational phantom axial slice using Gnuplot 59
4.6 Reconstructed axial slices using 30 keV 60
4.7 Dose in breast and lung for diffrentent number os projections 61
4.8 Graphs of the CNR for different implementations: Breast 64
4.9 Graphs of the CNR for different implementations: Lung 64

A.1 Simplified schematic for detector rotation calculations 77
A.2 Schematic of a 10° clockwise rotation of the detector 78
A.3 The four quarters of the 360° rotation 80
A.4 Schematic of the rotation when dealing with big angles 80
A.5 Schematic of a rotation relativaly to the Original Coordinate System 81
A.6 Schematic of the right triangles regarding the Origin 81
A.7 The four quarters approach for the source geometry rotation. 83

List of Tables

2.1 Effective atomic number and relative densities of tissue, lipid and bone . . . 20
2.2 Tissue weighting factors, w_T . . . 26
2.3 Filters and brief description . . . 39

3.1 Coordinates of the centers of mass of the organs of interest: Breats and Lungs 42
3.2 Coordnates of the centers of mass for each organ of interest and central point 42
3.3 Microcalcification Composition . . . 45

4.1 Air kerma experimental measurements . . . 55
4.2 $CTDI_{100}$ experimental and reported measurements . . . 56
4.3 Air Kerma experimental and simulated values . . . 57
4.4 Reconstructed Images using Linear Interpolation . . . 62
4.5 Reconstructed Images using Cubic Interpolation . . . 63

A.1 Coordinates and angles of the point P1 for detector rotation . . . 84
A.2 Coordinates and angles of the point P2 for detector rotation . . . 85
A.3 Shift values for detector rotation . . . 86
A.4 Rectification of the shift values for both axis . . . 87
A.5 Source position . . . 88
A.6 Source direction . . . 89

I.1 Adult female reference computational phantom: elemental compositions of each organ/tissue . . . 126
I.2 Continuation of the previous Table I.1. . . . 127

Acronyms

ALARA As Low As Reasonably Achievable.

AP Antero-Posterior.

CBCT Cone Beam Computed Tomography.

CNR Contrast-to-Noise Ratio.

CP Central Point.

CRX Chest Radiography.

CT Computed Tomography.

CTDI Computed Tomography Dose Index.

DBT Digital Breast Tomosynthesis.

EM Electromagnetic.

FBP Filtered Backprojection.

FOV Field Of View.

FPD Flat Panel Detectors.

FT Fourier Transform.

ICRP International Commission on Radiological Protection.

ICRU International Commission on Radiation Units and Measurements.

IGRT Image-Guided Radiotherapy Technique.

LDCT Low-Dose Computed Tomography.

Linac Linear Accelerator.

MATLAB Matrix Laboratory.

MC Monte Carlo.

MDCT Multi-detector Computed Tomography.

MRI Magnetic Resonance Imaging.

NLST National Lung Screening Trial.

PA Postero-Anterior.

PENELOPE PENetration and Energy Loss Of Positrons and Electrons.

PET Positron Emission Tomography.

PMMA Polymethyl Methacrylate.

ROI Region Of Interest.

SID Source-Isocentre-Distance.

SNR Signal-to-Noise Ratio.

Chapter 1

Motivation

1.1 Cancer Incidence and Mortality

Throughout the years, the number of diagnosed cases of cancer has grown at an alarming rate. Cancer is the second leading cause of mortality worldwide with approximately 14 million new diagnosed cases, 8.2 million cases of cancer deaths and 32.6 million cases of people living with cancer in 2012 [1] [2]. One in six deaths worldwide, is due to cancer, [1] causing more deaths than AIDS, tuberculosis, and malaria combined [3]. It's expected that by 2030, the global burden will grow to 21.7 million new cases of cancer and that cancer deaths have reached 13 million cases [3]. According to the World Cancer Report 2014, the three most commonly diagnosed cancers worldwide were lung cancer, accounting for 1.8 million cases (13.0% of the total globally diagnosed cases), breast cancer, accounting for 1.7 million cases (11.9% of the total globally diagnosed cases), and colorectum cancer, accounting for 1.3 million cases (9.7%), as shown in Figure 1.1.

The three most commonly diagnosed cancers, among men, in 2012 worldwide, were lung (1.2 million cases, 16.7% of the total), prostate (1.1 million cases, 15%) and colorectum (746 300 cases, 10%), and among women were breast (1.67 million cases, 25.2% of the total), colorectum (614 300 cases, 9.2%) and lung (583 100 cases, 8.7%) [3] [4]. Among men, lung cancer has the highest incidence and mortality rates, followed not far behind, by prostate cancer which has the second highest incidence rate. However, the mortality rate for prostate cancer is considerably lower than that for lung cancer. Among women, breast cancer has the highest incidence rate. However, breast cancer has a relatively low fatality rate, and although it has the highest mortality rate of any other cancer among women, this is less than one third of the incidence rate for lung cancer for both genders, and not much higher than the lung cancer mortality rate, which is the next cancer site with highest mortality rate, as shown in Figure 1.2 [4].

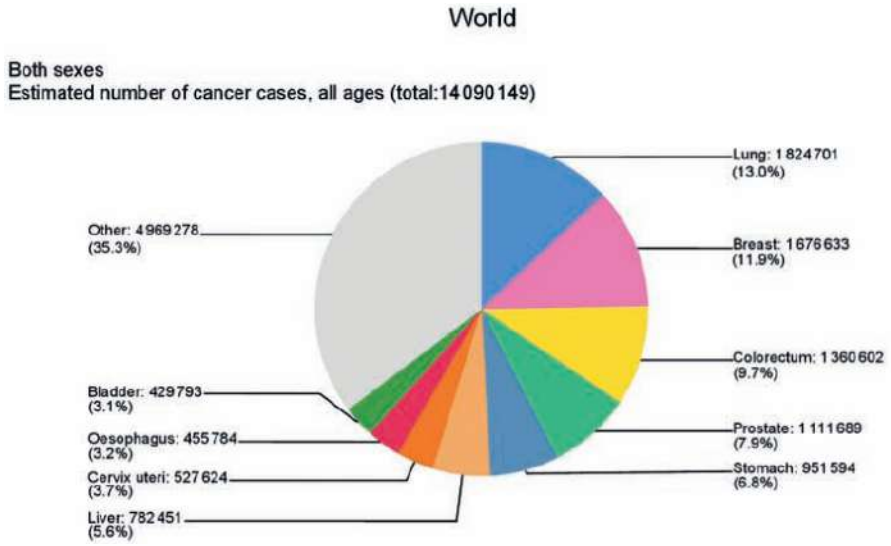

Figure 1.1: Adapted illustration of a graphic of the estimated world cancer incidence proportions by major sites in both sexes, in 2012 [4].

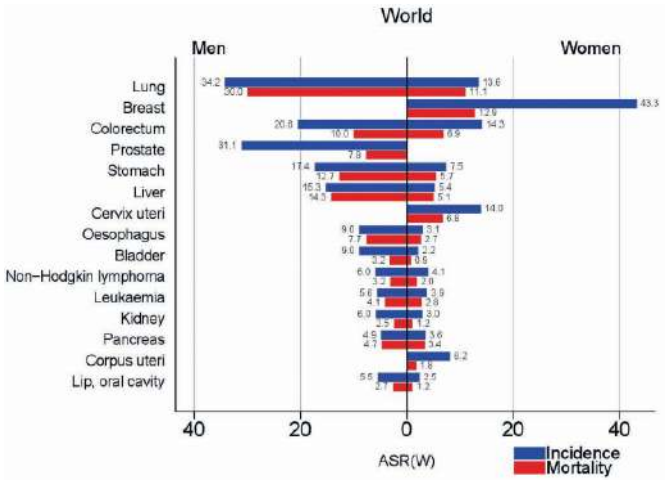

Figure 1.2: Adapted illustration of a graphic of the estimated age-standardized cancer incidence and mortality rates (ASR) per 100 000 in the world, by major sites, in men and women in 2012 [4].

In some countries, among women, lung cancer mortality rate has surpassed breast cancer mortality rate, e.g., North America, Eastern Asia, Northern Europe, Australia and New Zealand [3].

In Portugal, the five most common cancers diagnosed are: breast cancer, followed by prostate, colorectum and lung, however prostate, lung and breast are the cancer sites with highest mortality rate [5]. While the appearance of breast cancer symptoms (as a mass or a lump), isn't necessarily related to a cancer in an advanced state, lung cancer symptoms usually appear at a very advanced state of the disease, leading to a five-year survival rate [6].

1.2 Screening and Diagnostic Methods

In this section we will address screening and diagnostic methods that are currently recommended and implemented for lung and breast cancer. But first we will explain not only the main differences between screening and diagnosing a disease, but also the risks and therefore the required cautions associated to each one. There are some screening and diagnostic methods that are still under development and/or have not yet been evaluated in assessing a mortality benefit, with randomized trials, and therefore, are not yet considered a standard method for screening [7], consequently they will not be addressed in this chapter, e.g. autofluorescence bronchoscopy or exhaled breath analysis screening for lung cancer, and tomosynthesis screening for breast cancer [8]. Nevertheless, it's important to refer that some may assess in the diagnosis, for instance the Digital Breast Tomosynthesis (DBT), which is steadily increasing in prevalence in hospitals and mammography facilities [9].

Cancer screening is a crucial tool, considering that the key to reducing cancer mortality relies strongly on an early detection and diagnosis [10]. Nevertheless, these are methods which asymptomatic, healthy patients are submitted to, with intend of an early diagnosis. The majority of screened patients are likely healthy and that otherwise would carry on with their lives normally if they hadn't undergone screening, therefore the harms, risks and limitations associated to screening require crucial care and consideration in order to achieve balance between risk vs benefit [7] [11].

Contrary to imaging for screening, which asymptomatic patients are submitted to, a diagnostic evaluation is the process of assessing an existing problem or abnormality detected through screening [12]. Diagnostic imaging can be applied in two situations: a) imaging for clinical findings, i.e., if patient is manifesting symptoms that lead to cancer suspicion, as a palpable mass (in case of breast cancer) or persistent cough followed by sputum marked with blood (in case of lung cancer); b) incremental imaging after a possible abnormal screening exam [3] [12].

Although early detecting and diagnosing cancer is well known to be associated to a better prognosis and successful treatment, there are still many countries where late-stage diagnosis still occurs. This is mainly due to lack of awareness and to limited access to adequate detection and diagnostic services [3] [13].

Clinical guidelines on screening and diagnosing cancer, of all over the world, are constantly being developed, updated and reviewed, as new technological advances, new scientific investigations and new statistical data are taken in to consideration.

1.2.1 Breast Cancer

The *European Society for Medical Oncology* states that eighteen European countries have implemented mammography programs as their screening method for breast cancer. In their *Clinical Practice Guidelines 2015*, they recommend regular mammography

in women aged 50-69 years [9]. However, a recent guideline update from the *American Cancer Society* for breast cancer screening, not only recommends that women should have the possibility to start annual screening mammography exams between ages of 40 and 44 years, and start with regular annual screening mammography exams from age 45 years, but also recommends that clinical breast examination should not be performed at any age [13]. As for the *National Comprehensive Cancer Network Breast Cancer Screening and Diagnosis Guidelines*, they recommend an annual screening mammography beginning at the age of 40 [12]. Nevertheless, according to the *Portuguese National Recommendations for diagnosis and treatment of breast cancer 09*, the detection should be done through mammography exams, which still is the preferable screening method implemented in Portugal, or through prophylactic exams, e.g. Breast Self-Examination [14].

Mammography screening is basically a mechanism for breast imaging. Typically, it includes two x-ray images, being one taken from the top of the breast (craniocaudal), and the other taken from the side of the breast (mediolateral oblique) [12]. The Mammography Quality Standards Act limit is 3 mGy per view of screening mammography, for an average breast (5 cm thick and 50% glandular breast) [15]. Various studies have shown that mammography screening is associated to a reduction of breast cancer mortality, [13] however, it isn't a perfect test.

The harms associated to mammography screening are mainly due to three factors: false-positive diagnosis, false-negative diagnosis and over diagnosis [11]. A false positive diagnosis is considered to be harmful, as it can lead to patient distress, and will result in unnecessary additional procedures, radiation exposures and/or biopsy [16]. False negative results are harmful, for obvious reasons, as it leads to breast cancers not being detected, delaying diagnosis and treatment [6] [17]. This occurs due to the inherent problem associated to the machine itself, which projects into a single plan the thickness of the breast, resulting in the overlap of tissue, which may obscure an abnormally, or even, lead to a false positive diagnosis [17]. Over diagnosing a cancer is when the disease is detected through screening however it wouldn't lead to symptomatic breast cancer if it hadn't been detected in the first place, and will lead to unnecessary therapy [6] [13].

As for diagnosing breast cancer, the procedure is basically based on clinical examination, medical imaging and ultimately confirmed by pathological assessment [9]. However, this process involves a complex evaluation, and the procedures may differ from patient to patient, as it's adapted depending on each case scenario. After a first line evaluation, that is done to assess patient's general health status (e.g. clinical history, menopausal status, full blood count, among others), a second line evaluation is done, in order to assess the previously detected abnormality. For this second assessment, several exams may be conducted, such as, physical examination, another mammography, breast ultrasound, breast Magnetic Resonance Imaging (MRI) and/or biopsy for pathology determination [9].

1.2.2 Lung Cancer

As previously seen, lung cancer is the leading cause of cancer death in developed countries, exceeding breast cancer death rate in women [3]. Frequently, this is due to the fact that screening for other cancer diseases is commonly practiced (e.g. breast, prostate, colorectum), whereas it is not for lung cancer [7].

The American College of Chest Physicians Guidelines, 3rd Edition, suggest annual screening with Low-Dose Computed Tomography (LDCT), to people considered to be of high-risk, i.e., smokers or former smokers who are age 55 to 74 and who have smoked for 30 pack years (the number of packs of cigarettes smoked per day multiplied by the number of years a person has smoked) or more, and either continue smoking or have quitted within the past 15 years. Additionally they also state that screening should only be conducted in centers similar to those where the National Lung Screening Trial (NLST) was conducted, with coordinated care and complete knowledge of the screening process [7] [18]. NLST was the first randomized controlled trial which showed evidence of the benefits associated to screening with LDCT in decreasing lung cancer mortality [19] [20]. *The American Society of Clinical Oncologists* also state this same recommendation in their Guidelines: *"The Role Of Computed Tomography Screening for Lung Cancer"* [19].

Although lung cancer screening is not generally practiced worldwide, there is consensus in using LDCT technique as a screening method for individuals with high-risk factors.

LDCT is a computed tomography scan performed at low dose, using a tube voltage of 100-120 kVp and currents of 40-60 mAs or less [6]. The mean effective dose is 1.5 mSv for LDCT, as for a standard Computed Tomography (CT), is 7 mSv, however when compared to a Chest Radiography (CRX), the dose delivered with a LDCT is greater (about 10 times greater) [17]. Alike mammography screening, LDCT screening also has risks inherent to it. The harms associated to LDCT are the same as described above in subsection 1.2.1 *Breast Cancer*, for mammography screening (false-positive results, false-negative results and over-diagnosis) [6].

For the diagnosis of lung cancer it may be detected through initial screening LDCT, follow-up or annual screening LDCT and this will determine the next procedures. Depending on the nodules' nature (solid, part-solid, non-solid or multiple non-solid), diameter, and presence of infection/inflammation, furthermore exams and procedures for evaluating the findings can be conducted. The next procedures include follow-up LDCT, Positron Emission Tomography (PET)/CT, Chest CT plus contrast, biopsy or surgical excision, bronchoscopy, pulmonary function tests and/or pathologic mediastinal lymph node evaluation [6] [21].

1.3 Purpose of the project

There is an undeniable need to develop screening and diagnostic methods that are ever more accurate and with better performance, leading to a more precise and faster diagnosis. By assisting physicians with better medical information of their patients we will be increasing the chances of early cancer detection and consequently increasing the survival rate. One way to accomplish this is to focus on the flaws and limitations of other pre-existing methods. This study emerged in attempt to respond to the nonexistence of a technique which allows medical imaging acquisition, simultaneously of the breast and lung. This method will allow reduction of the dose administrated to the patient during image acquisition, in agreement with the principle that patient doses need to be kept As Low As Reasonably Achievable (ALARA) [22]. This can be achieved, not only due to the intrinsic properties of the Cone Beam Computed Tomography (CBCT), which requires only one full rotation to acquire data of the Field Of View (FOV), but also through a modulated beam, that will vary the energy according to the angles for which the image was acquired. Furthermore, reconstructive algorithms were developed in order to improve image quality, and therefore, reduce the dose necessary for image acquisition.

Chapter 2

Theoretical Concepts

In this chapter all theoretical concepts relevant for the comprehension of this project are explained. This chapter is divided into three main sections, in which the first one refers to the CBCT system, where a brief description of this mechanism and it's main components, is made. The second section refers to *X-ray Radiation* and in this section all important concepts regarding x-ray radiation are described. It starts by describing the main concepts of particle collisions (e.g., Elastic and Inelastic collisions). In a second subsection, the instrumentation and x-ray production is described (*X-ray tubes*), followed by a subsection describing the x-ray spectrum and the physics underlying such radiation (*Characteristic x-rays* and *Bremsstrahlung*). The fourth subsection approaches the *Interactions of photons with matter*, in which *Rayleigh Scattering*, *Compton Scattering* and *Photoelectric Effect* are explained. This is followed by the subsection where *X-ray linear and mass attenuation coefficients* is referred to, in which *Cross-sections* are also explained. The last subsection is *X-ray dosimetry*, where three main sections are found: *Measurements and units in photon dosimetry*; *Computed Tomography Dosimetry*, where CT and CBCT dosimetry systems are referred to; and *Monte Carlo Computation*, where Monte Carlo simulations and voxelized phantoms will be addressed.

The last section, *Medical Image Reconstruction*, is a section in which not only the physics regarding data acquisition from CT scans are explained, but also some reconstruction algorithms. This section is finalized with *Image Quality* in which the measurement for analyzing the reconstructed images is described.

2.1 Cone Beam Computed Tomography

In 1982, the first CBCT scanner was built for angiography purposes. Subsequently in the 1990s several teams also developed CBCT systems, differing in their capabilities and

features, but always aiming for angiography purposes. It was only in the late 1900s, early new millennium, that CBCT systems started to emerge for dental and maxillofacial radiology purposes and for radiotherapy guidance (Image-Guided Radiotherapy Technique (IGRT)). Despite the CBCT concept not being a new discovery, it is an emerging technology, and its use in clinical practices is gradually increasing. CBCT systems nowadays have a variety of medical applications that range from research to clinical applications. Ongoing studies are also being conducted to build a dedicated CBCT-based imaging system for mammography [23] [24] [25] [26]. For clinical applications it can be found, for example, for dental and maxillofacial imaging, head and neck imaging, high-resolution bone imaging (for orthopedic purposes), radiotherapy (IGRT), and intra-operative and interventional imaging (for angiographic CT). This strong rise in CBCT systems is due to recent technological advances, which made possible the development of clinical CBCT systems that are sufficiently inexpensive and sufficiently small to be used in operating rooms, clinics, intensive care units and emergency rooms [26].

A CBCT scanner is a subcategory of CT scanners, however it's different from Multidetector Computed Tomography (MDCT) systems which are the industry standard for CT, with certain design features and application domains that are very specific and consequently the image quality differs from that of an MDCT. One of the most characteristic feature of a CBCT system is the shape of its beam, which is in a cone shape rather than in a fan shape, as shown in Figure 2.1. The tomographic physics based on which CBCT operates, are basically the same as a MDCT [27] [26].

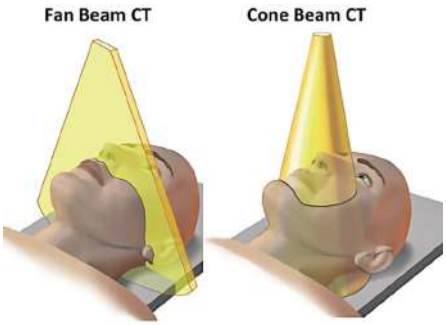

Figure 2.1: Adapted illustration of a fan beam CT scan on the left, and a cone beam CT scan on the right [28].

Another, very characteristic feature is it's detector. CBCT scanners make use of Flat Panel Detectors (FPD), as shown in Figure 2.2, instead of an arc detector, as found in MDCT. The FPD system leads to a 2D bank of detectors which have no curvature, allowing higher spatial resolution and larger volume coverage in a single, or partial, rotation. However, this requires demanding reconstruction mathematics in order to apply correction methods accounting for the different distances from source to detector [27] [26].

The gantry of a CBCT system differs depending on its applicability, hence the variety of applications in which CBCT systems are found. The different types of gantry include:

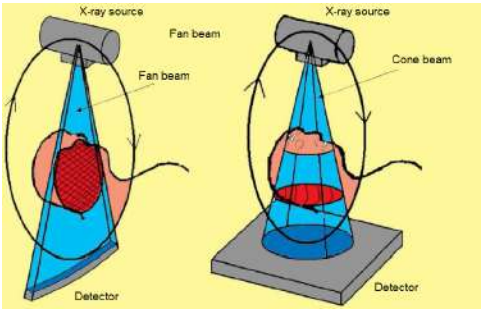

Figure 2.2: Adapted illustration showing the differences between the arc-shaped detector used in conventional CT systems on the left and the flat panel detector, used in CBCT systems, on the right [29].

c-arm-based CBCT, CT-gantry-based CBCT, co-integrated systems and CBCT in IGRT.

In radiotherapy (IGRT), a CBCT system is used for precise alignment of the patient on the table of the Linear Accelerator (Linac) and there are two different modes, the kV CBCT and the MV CBCT. The kV CBCT system is a separate system, consisting of an x-ray source, where the x-rays are produced using a conventional x-ray tube operating in the kV range, and a FPD. Both, x-ray tube and FPD come coupled to the Linac gantry, as they are mounted on retractable arms opposite to each other and positioned perpendicularly to the Linac's beam. Despite the fact that a Linac gantry can only perform a 360° rotation, after which it must be rotated back, the CBCT system enables a large FOV to be imaged by scanning the target volume asymmetrically. This is accomplished by shifting the FPD laterally [27] [26] [30].

2.2 X-ray Radiation

X-rays are a type of Electromagnetic (EM) radiation that appears on the more energetic (smaller wavelength) end of the EM spectrum along with Gamma Rays, and their wavelength can range from 0.001 to 10 nm, corresponding to an energy range of approximately 0.052 to 129.544 keV [31].

This high energy EM radiation, not only exhibits wave-like behavior but also behaves as single particle-like "packets of energy"or *quanta* of energy, called photons. The energy of a photon is given by

$$E = h\nu = \frac{hc}{\lambda} \tag{2.1}$$

where h is the Planck constant ($h = 6.626 \times 10^{-34}$ J.s $= 4.136 \times 10^{-18}$ keV.s), ν is the frequency of the photon, c is the speed of light in vacuum ($c = 2.998 \times 10^8$ m/s $\approx 3 \times 10^8$ m/s) and λ is the photon's wavelength [32].

For energy expressed in keV and the wavelength expressed in nm, $h.c = 1.2397 \times 10^{-6}$ eV.m, hence obtaining the following equation

$$E(\text{keV}) = \frac{1.24}{\lambda(\text{nm})} \tag{2.2}$$

This is useful given that photon energies are usually expressed in electron volts (eV), which is a common unit of energy [27]. Electron volts is defined as the energy acquired by a single electron when submitted to an electrical potential difference of one volt, in vacuum, this is 1 eV = 1.602×10^{-19} J [33].

Gamma rays are also photons and their energy range is usually of 100 to 10 000 keV. Despite the overlap of energies, x-rays and gamma rays are distinguishable by evaluating the photon's origin. Therefore photon emissions that originate from the atom's nucleus are identified as gamma rays, as for x-rays they have their origin in the rearrange of the atom's electronic cloud or in the interaction of outer photons or particles with the the atom [34].

X-ray radiation is produced by x-ray tubes and it's the outcome of the combination of two main interactions: bremsstrahlung and characteristic x-rays as we will see further on in section 2.2.2 *X-ray Spectrum*. Nevertheless we will first address certain concepts, as inelastic and elastic interactions as well as excitation and ionization, in the following section 2.2.0.1 *Ionizing and non-ionizing interactions*, as they are relevant concepts for further comprehension.

2.2.0.1 Ionizing and non-ionizing interactions

An inelastic collision occurs when a photon or any particle interacts with an atom and energy is transferred between the two, causing the ionization of the atom or leaving it in an exited state, in other words the interaction leads to a change in the atom's internal structure and in the particles' energy. Two examples of inelastic collisions are Ionization and Excitation. As for in an elastic scatter there's no energy being transferred due to the interaction, only the particle's trajectory is altered, in other words the particle is scattered but there's no change to atom's internal structure nor to the particle's energy [35].

Ionization is the process by which one or more electrons are ejected from the atom or molecule as a result of the interaction with outer particles or photons. Excitation however, doesn't imply the loss of electrons, but rather their transfer to a higher energy level, i.e., to an outer electron orbit, further from the atom's nucleus, as a result of the interaction. Particles or photons with less energy are less likely to ionize an atom and will transfer their energy through excitation or elastic scattering which are processes that require less energy [36]. The minimum energy required to remove an electron, i.e., to ionize an atom is known as the ionization potential [37]. Charged and uncharged particles or photons that interact with an medium resulting in it's ionization are considered Ionizing Radiation. Nevertheless, ionization and excitation are processes which cannot be separated, due to the fact that one given energy can result in the ionization of a given element but only lead to the excitation of another element. Therefore a pragmatic approach is usually used, in which a threshold for the energy (also known as a cutoff energy) is established. Below that energy particles and/or photons can be assumed to be not ionizing, given that it establishes the minimum energy that can be transferred to the medium [36].

2.2.1 X-ray tubes

The device whereby the x-ray beam is generated and emitted is called the X-ray tube. It's an equipment specialized to produce x-ray beams and it's main components are typically contained within an evacuated envelope made of Pyrex glass or metal [31]. The main components, this is, the minimum requirements for x-ray production are: an electron source (cathode), an evacuated path for electron acceleration (evacuated envelope), a target (anode), and an external power source (x-ray generator) supplying the power which provides a high potential difference for accelerating the electrons. In Figure 2.3 a schematic of an x-ray tube's main components is illustrated. The x-ray generator allows the selection of the three major parameters that determine the x-ray beam characteristics: the tube voltage (kV), the tube current (mA) and exposure time (s). Usually the product of the tube current and exposure time are considered as one entity, the milliampere-second (mAs) [27].

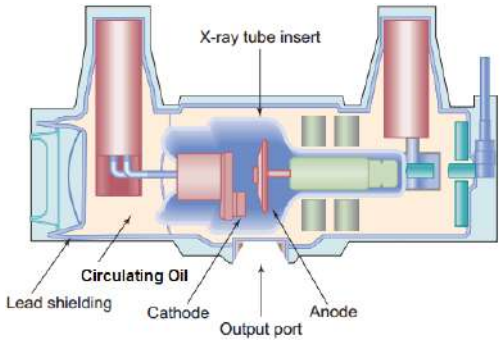

Figure 2.3: Adapted illustration of an x-ray tube with it's major components: the evacuated envelope, which in the figure is represented as the x-ray tube insert, the cathode, the anode, the output port from where the beam is emitted and the circulating oil and lead shield which are essential to ensure the safety and efficiency of the x-ray tube [27].

The cathode is the source of electrons, consisting of a filament and a focusing cup. The filament is a spiral tungsten wire through which an electric current, up to 7000 mA and voltage of approximately 10 V, passes by. Heat is then generated through the resistance to electron flow through the filament, leading to a process in which the electrons of the filament's material have sufficient energy and are released from it's surface called *thermionic emission*. By adjusting the filament current and consequently by the filament temperature, the number of electrons that are released can be controlled. The electron beam produced is emission-limited, this is, the filament current determines the x-ray tube current, meaning that the x-ray flux is proportional to the tube current, regardless of the tube voltage. However, it's only when the potential difference (tube voltage) is applied between the cathode and the anode, within the evacuated envelope, that the released electrons flow [27] [38].

The tube voltage, this is, the electric potential difference, applied between the cathode and the anode, for diagnostic radiology purposes is of 20 to 150 kV. This potential difference is usually called accelerating voltage or kilo-voltage peak (kVp). As electrons travel

from the cathode to the anode they are accelerated due to the potential difference and attain kinetic energy. This kinetic energy is equal to the product of the electrical charge and the potential difference. As previously mentioned, the electron volt (eV) is a unit of energy which is equal to the energy acquired by an electron when accelerated through a potential difference of 1 V, therefore the kinetic energy of an electron accelerated by a potential difference of 50 kV is 50 keV [27].

The target metal is called the anode, and it's maintained at a large positive potential difference relative to the cathode in order to accelerate the electrons towards it. As electrons interact with the anode their kinetic energy is converted into other forms of energy, like x-rays as mentioned before, but this only represents approximately 1% of the electron's energy, the majority is converted into thermal energy and therefore generating very high temperatures in the anode. To avoid heat damage the duration of x-ray production must be limited. Due to it's high melting point of 3370°C and high atomic number Z =74, tungsten is the most commonly used anode material. Nevertheless an anode rotor is attached to the anode which rotates at speeds of approximately 3000 rpm ensuring that the electron beam doesn't strike the anode always at the same point and therefore reducing the localized heating. Additionally, within the tube housing, insulating circulating oil surrounding the whole envelope works as a cooling mechanism as shown in Figure 2.3 [27].

To guarantee a well defined small area in which the electrons will strike, the anode has a trapezium shape with an angle between 8° to 17° being 12° to 15° the usual range. Two of the major factor which are influenced by the anode angle are: the size of the focal point, the x-ray beam coverage and the x-ray beam intensity [38].

The focal point size (f) is given by:

$$f = F \sin\theta \tag{2.3}$$

where F is the width of the electron beam and θ is the anode's angle, as shown in Figure 2.4. The focal point size range from 0.3 mm for digital mammography and 0.6 to 1.2 mm for planar radiography and CT. For small anode angles the focal point (f) becomes smaller for the same electron beam width (F), providing better spatial resolution. Therefore the optimal anode angle depends on the clinical imaging application given that a small anode angle is preferable when dealing with a small FOV, which requires a smaller beam coverage, but for a large FOV, using a larger anode angle is more useful [38].

2.2.2 X-ray spectrum

As previously seen, x-ray tubes are the mechanism responsible for generating x-ray beams, and they have a wide range of energies. An x-ray spectrum is basically a plot of the relative number of photons produced as a function of their energy, as represented in Figure 2.5. The production of X-rays for medical imaging, can occur through two main mechanisms: through the transition of electrons between the atom's shells (named

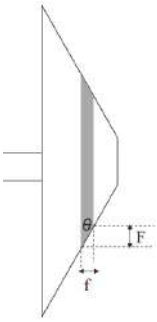

Figure 2.4: Adapted illustration of the anode, showing the correlation between the electron beam width F, the anode's angle θ and the focal point size f [38].

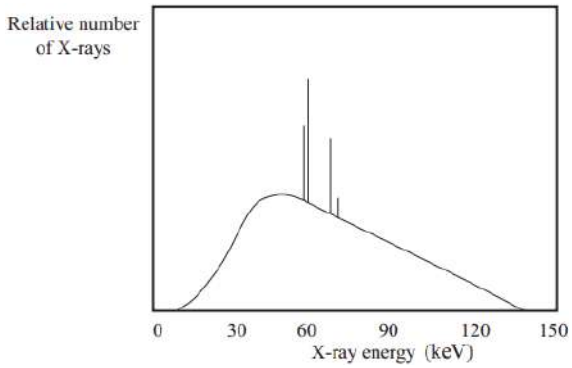

Figure 2.5: Adapted illustration of an x-ray spectrum, showing the contributions of both interactions, bremsstrahlung and characteristic x-rays, to the produced x-ray beam [38].

characteristic X-rays) resulting in the production of x-rays with distinct energies that can be identified as distinct sharp lines in the plot of the energy spectrum, and through the interaction of electrons with the atomic nuclei causing their sudden deceleration (named Bremsstrahlung) resulting in the production of x-rays with an expanded spread of energies [32]. Both mechanisms will be discussed with greater detail in the following sections: 2.2.2.1 *Characteristic x-rays* and 2.2.2.2 *Bremsstrahlung*.

2.2.2.1 Characteristic x-rays

In the atom, each electron has a discrete energy state, according to the electron shell it occupies and each shell is denoted by a letter (K,L,M,N,...). The atom's most inner shell is the K shell, for which the electrons have the lowest energy and therefore it's the shell which requires the most energy to remove an electron from, as shown in Figure 2.6.

The shells can also be referenced by their quantum numbers (1,2,3,4,...), whereas the quantum number 1 refers to the K shell, the number 2 to the L shell and so on. Each shell can hold $2n^2$ electrons, where n is the shell's assigned quantum number, for instance, the L shell (n=2) can hold 8 electrons, as for the K shell (n=1), it can only hold 2 electrons [27].

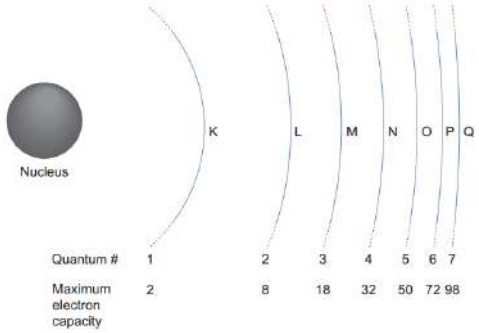

Figure 2.6: Adapted illustration of an atom's electronic shells, their designations and the electron capacity per shell [27].

The interaction of outer electrons with an atom may result in the removal of an electron creating a vacancy in one of the atom's shell, and therefore, ionizing the atom. This is only possible if the energy transferred during their interaction is equal or greater than the atom's orbital binding energy [27]. As a result, the atom is left in a very unstable state, for it will be lacking an electron in its electronic cloud, making it very unstable and therefore the vacant is rapidly filled by an electron from an outer shell. The transition of this electron between atomic shells will result in the emission of a single photon with energies in the x-ray range as shown in Figure 2.7.

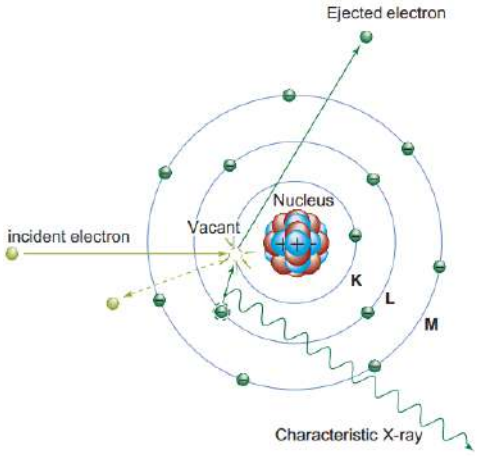

Figure 2.7: Adapted illustration of the interaction that results in the emission of characteristic x-rays. The incident electron interacts with the K-shell electron, ejecting it. The created vacancy is rapidly filled with an outer electron that had to transit from it's original shell and therefore emits energy, creating the characteristic x-rays [27].

The produced x-ray's energy (E_{x-ray}) is given by the difference between the electron binding energies (E_b) of both vacant shell and initial shell:

$$E_{x-ray} = E_{bvacant} - E_{binitial} \tag{2.4}$$

This photon has an energy which is characteristic of the particular metal used to produce the x-rays, for it will have a distinctive energy according to the difference in

binding energies between the inner and outer shells involved in the process. Physicists call these kind of x-rays Characteristic X-rays and it can assume any energy typically from 0.052 to 129.544 keV. Given the fact that the atom's shells only allow distinct energies, characteristic x-rays can only assume discrete energies [31] [27].

Characteristic x-rays are differentiated according to the shell where the vacancy is located, for instance, when a vacancy in the K shell is filled, the resulting x-ray is called a K-characteristic x-ray. If the same vacancy is filled by an electron which transited from an adjacent shell, the x-ray is considered an alpha (e.g. an L to K transition will result in a K_α characteristic x-ray). As for x-rays resulting from electrons which transited from nonadjacent shells, they are considered beta (e.g. an M to K transition will result in the emission of a K_β characteristic x-ray) [27].

2.2.2.2 Bremsstrahlung

Despite most electrons interacting with the atom's electronic shell as they pass through matter, some undergo inelastic interactions with the atom's nuclei. As a result of the interaction of these electrons with the positively charged nucleus, they suffer electrical (Coulombic) forces of attraction causing a deflection in their path and resulting in a kinetic energy loss which is instantaneously emitted as photons (i.e., x-rays). The kinetic energy lost by the electrons are equal to the energy of the radiation emitted and therefore energy is conserved. Due to this association between the electron deceleration and the photon emission, this process of x-ray production is called Bremsstrahlung which means 'brake radiation' in German [37] [27].

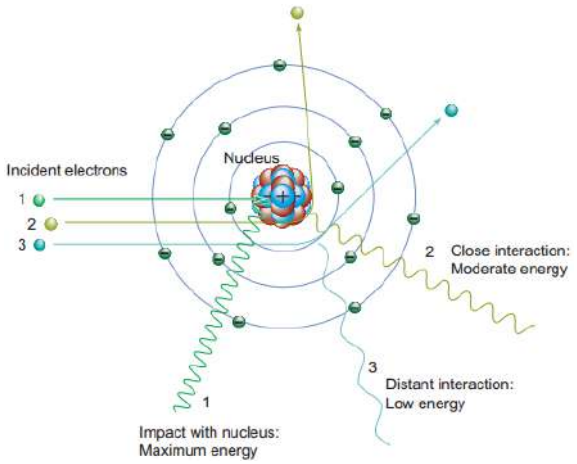

Figure 2.8: Adapted illustration of the different x-ray energies that may be produced through bremsstrahlung, regarding the different distances for which the incident electrons (1,2 and 3) approach the atom's nucleus [27].

This interaction of electrons with the atomic nuclei is weak at relatively large distances given that the Coulombic force is proportional to the inverse of the square of the distance and therefore producing low x-ray energies. As the distance gets smaller, the forces interacting on the electron increases, causing greater deceleration and therefore

producing higher x-ray energies, as shown in Figure 2.8. The highest x-ray energies are produced when the electron and atomic nuclei are the closest (or when impact occurs), however these close interaction has a very low probability of occurring and therefore the number of high energetic photons produced is very low. [27].

The produced x-rays can have energies that range from zero up to, and including, the entire energy the deflected electron had, originating a continuous spectrum that will cover that same range of energies. Usually the bremsstrahlung spectrum is filtered, this is, there's a removal of the less energetic x-rays when the beam goes through materials which are inherent to the x-ray tube (e.g., the tube's glass window) or through purposefully placed materials in order to adjust the spectrum to the wanted energies (e.g., aluminum or copper sheets) [27]. A bremsstrahlung spectrum can be seen as the probability distribution of x-ray photons as a function of the energies for those same photons as shown in Figure 2.9, where the highest x-ray energy is determined by the peak voltage (kVp), as mentioned in section 2.2.1 *X-ray tubes* [37] [27].

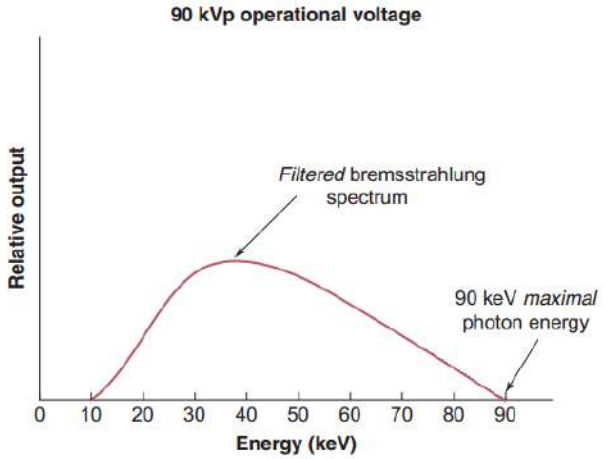

Figure 2.9: Adapted illustration of a filtered bremsstrahlung spectrum plot, for a $90kVp$ operational voltage [27].

The probability of bremsstrahlung emission is proportional to the atomic number of the absorber, which is given by the value Z^2 but it is inversely proportional to the square of the mass of the incident particle, this is, Z^2/m^2. Therefore the higher the material's atomic number, such as tungsten ($Z = 74$), the higher the probability of bremsstrahlung. Due to the high influence of the incident particle's mass, heavier charged particles (e.g., protons and alpha particles) have less than one millionth of the probability electrons have of bremsstrahlung production [37]. The majority of the x-rays used for medical imaging are produced through bremsstrahlung given that the x-ray tubes uses electrons as the interacting particle and usually uses tungsten, molybdenum or rhodium as the anode, as previously seen in section 2.2.1 *X-ray tubes* [37] [27].

2.2.3 Interaction of photons with matter

The interaction of the x-rays with matter as it leaves the x-ray tube and encounters tissue, for medical imaging purposes will be discussed in this section. In order to generate a medical image in radiology, there must be an interaction of some kind of energy with the body, which means that this energy must also be capable of penetrating tissues. In diagnostic radiology (e.g., mammography and CT), one kind of energy used are x-rays. As the x-rays pass through the body and are detected, they will contain information regarding the internal anatomy, due to interactions with the various tissues in it's path. Therefore, when using x-rays, there's always a compromise between the dose delivered to the patient and the image quality, given that for relatively higher x-ray energies, which leads to higher dose delivered to patient, better x-ray images can be developed [27].

Photons are electrically neutral and do not steadily lose energy as they penetrate matter, like charged particles do. Therefore, they can travel relatively long distances before interacting with an atom. The distance that a given photon can penetrate matter is dictated statistically by a probability of interaction per unit distance traveled, which depends on the properties of the matter traversed and on the photon energy. When the photon interacts, it might be absorbed or it might be scattered, changing its direction, with or without energy loss [39].

There are four main types of photon interactions with matter: Rayleigh Scattering, Compton Scattering, Photoelectric Effect, and Pair Production. Rayleigh Scattering, Compton Scattering and Photoelectric Effect will be discussed in the following sections 2.2.3.1, 2.2.3.2 and 2.2.3.3, respectively. Pair Production won't be addressed since it's an interaction that only occurs with very high energy photons (exceeding 1.02 MeV), which isn't in the diagnostic radiology range.

2.2.3.1 Rayleigh Scattering

Rayleigh scattering or Coherent scattering is an interaction in which the incident photon's energy is absorbed by an atom and immediately released again in a form of a new photon with the same energy but traveling in a different direction. Therefore it is a non-ionizing interaction and it mainly occurs with very low energy photons (<30 keV). The lower the energy, the higher the scattering angle. In the diagnostic energy range this interaction has a very low probability of occurring. In soft tissue, Rayleigh scatter accounts for less than 5% of photon interactions above 70 keV and at most only accounts for about 10% of interactions at 30 keV. However, for mammography, the energy is lower (15-30 keV) and Rayleigh scatter cannot be neglected [34] [27].

2.2.3.2 Compton Scattering

Compton scattering is an interaction in which the incident photon leads to the ejection of an electron, most likely from an outer electronic shell (usually the valence-shell).

It's the predominant interaction of x-rays photons with tissue, regarding the diagnostic energy range of 30 to 80 keV [27] [38]. After the interaction, an electron is ejected from the atom and the scattered photon, not only is deflected with an angle of θ from it's original path but is also left with a lower energy, as shown in Figure 2.10.

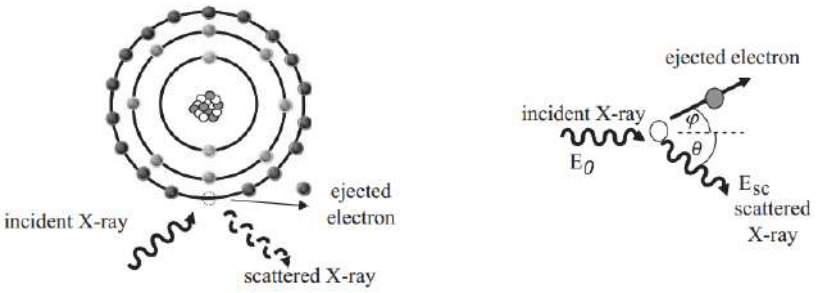

Figure 2.10: Adapted illustration of the compton scattering interaction in which an electron from the atom's outer shell is ejected due to an incident photon (on the left) and the photon is then scattered at an angle θ regarding it's initial trajectory (on the right) [38].

Both energy and momentum must be conserved, as with all types of interactions, and therefore the variation in the photons' wavelength (energy) can be determined by the following equation:

$$\Delta\lambda = \frac{h}{mc}(1 - \cos\theta) \tag{2.5}$$

where h is the Planck constant ($h = 6.626 \times 10^{-34}$ J.s), m is the mass of the electron, c is the speed of light in vacuum ($c = 3 \times 10^8$ m/s) and θ is the photon's scattering angle, regarding its initial trajectory [38]. Also, the energy variation (ΔE) involved in Compton scattering can be calculated by:

$$\Delta E = E_0 - E_{sc} = \frac{hc}{\lambda_0} - \frac{hc}{\lambda_{sc}} \tag{2.6}$$

where E_0 is the energy of the incident photon, E_{sc} is the energy of the scattered photon, λ_0 is the wavelength of the incident photon and λ_{sc} is the wavelength of the scattered photon [38]. Therefore, the energy of the scattered photon can be easily determined by converting the previous equation 2.6, resulting in:

$$E_{sc} = \frac{E_0}{1 + (\frac{E_0}{mc^2})(1 - \cos\theta)} \tag{2.7}$$

where $mc^2 = 511$ keV [38].

For higher incident photon energies, not only do the angles for which the scattered photons and emitted electrons decrease (making these photons more likely to reach the detector) but also the majority of the energy is transferred to the scattered electron. For instance, when $E_0 = 100$ keV and $\theta = 60°$, the scattered photon energy (E_{sc}) is 90% of the E_0 but only 17% when $E_0 = 5$ MeV. When Compton scattering occurs for lower x-ray energies (i.e., x-ray energy of 20 to 80 keV), the majority of the incident photon energy is transferred to the scattered photon. For instance, when $E_0 = 80$ keV the minimum energy

of E_{sc} is 61 keV, allowing scattered photons to have relatively high energies and tissue penetrability. The detection of these scattered photons isn't favorable to the production of medical imaging for these photons result in the degradation of the image contrast. The probability of occurring Compton interactions depends not only on the energy of the incident photon, but also on the electron density, this is, the number of electrons per gram density, of the absorber. Nevertheless, hydrogenous materials, such as adipose tissue, have higher probability of Compton scattering than anhydrogenous materials of equal mass. This is due to the absence of neutrons in the hydrogen atom, which results in an approximate doubling of the electron density [27].

The Compton scatter linear attenuation coefficient is proportional to:

$$\mu_{Compton} \propto \rho N \frac{Z}{A} \tag{2.8}$$

where ρ is the mass density of the tissue in a voxel, N is Avogadro's number (6.023×10^{23}), Z is the atomic number and A is the atomic mass. The primary constituents of soft tissue are carbon, hydrogen, oxygen and nitrogen, and the ratio Z/A for all these elements is 1/2, with exception to hydrogen, which is 1. This leads to the conclusion that hydrogenous tissues, such as adipose tissue would have higher $\mu_{Compton}$, however this doesn't apply in reality, given that the range of fluctuation in hydrogen content in tissues is small and the lower density of adipose ($\rho \approx 0.94$ g.cm^{-3}) compared to soft tissue ($\rho \approx 1$ g.cm^{-3}), tends to dominate the equation 2.8, when differentiating soft tissue and adipose tissue. Therefore, adipose tissue appears darker (has lower $\mu_{Compton}$) than soft tissue [27].

2.2.3.3 Photoelectric Effect

The photoelectric effect is an interaction in which the incident photon's energy is totally transferred to an electron, resulting in it's ejection with a certain kinetic energy. Part of the incident photon's energy is used to overcome the electron's binding energy (ionizing the atom), and the rest of the energy is transferred to the photoelectron as kinetic energy. The photoelectron's energy (E_{pe}) is given by:

$$E_{pe} = E_o - E_b \tag{2.9}$$

where E_o is the incident photon's energy and E_b is the electron's binding energy [31] [27].

Therefore, in order for photoelectric absorption to occur, the incident photon's energy must be greater than or equal to the electron's binding energy. As the photoelectron is ejected, a vacancy in the inner shell, from which it was emitted, is created. This vacancy is rapidly filled by an electron from an outer shell, originating another vacancy that consequently will be filled by another electron from an outer shell. Hence originating an electron cascade from outer to inner shells. The energy from the difference in binding energies can be released as characteristic x-rays or as Auger[1] electron emission. However,

[1] Energy is transferred to an orbital electron in the same shell as the cascade electron, hence ejecting it.

if characteristic x-rays are emitted, they have very low energies (a few keV) and are absorbed by the surrounding tissue, making it impossible to reach the image detector. In the other hand, if Auger electron emission occurs, it will also be absorbed by the surrounding tissue. Therefore photoelectric interaction is advantageous due to the lack of scattered photons, which would degrade the medical image, providing a reduction of the contrast in the x-ray images [27] [38].

The probability of photoelectric interaction (P_{pe}) occurring is proportional to:

$$P_{pe} \propto \rho \frac{Z_{eff}^3}{E^3} \tag{2.10}$$

where ρ is the tissue density, Z_{eff} is the effective atomic number and E is the energy of the incident photon [38]. The effective atomic number and relative densities of the main compounds for which x-rays interact, regarding medical imaging purposes, are shown in Table 2.1. Therefore, based on the equation 2.10, for low energy x-rays, the photoelectric effect produces high contrast between bone (high attenuation) and soft tissue (low attenuation), but for high energy x-rays the contrast is decreased [38].

Table 2.1: The effective atomic number (Z_{eff}) and relative densities (ρ) of the main compounds found in the human body, which are: tissue, lipid and bone [38].

	Tissue	Lipid	Bone
Z_{eff}	~ 7.4	~ 6.9	~ 13.8
ρ	1	0.9	1.85

Nevertheless, issues regarding image contrast, image quality and image reconstruction will be further discussed and explained in section 2.3 *Medical Image Reconstruction*.

When dealing with low energies (less than about 30 to 40 keV), the photoelectric effect prevails over compton scattering. Given that the effective atomic number Z_{eff} (which is the average atomic number calculated for a compound or mixture) for bone is approximately twice of the Z_{eff} for tissue, there is far more attenuation in bone than in tissue, and excellent tissue contrast [38] [27]. However, for higher x-ray energies, the contribution from Compton scattering becomes more important, and therefore, contrast drops as described further in section 2.2.4 *X-ray linear and mass attenuation coefficients* [38].

2.2.4 X-ray linear and mass attenuation coefficients

Attenuation is the process for which an x-ray beam loses photons as it passes through matter [27]. As previously mentioned, in the diagnostic energy range, there are two main processes of photon interactions: being absorbed (Photoelectric Effect) or scattered (Compton Scattering). Therefore, these are the two main causes of attenuation.

The ***linear attenuation coefficient*** (μ) is the fraction of photons removed from a monoenergetic[2] x-ray beam per unit thickness of material it's passing through, and it's units

[2] A beam containing a single quantum energy.

is inverse centimeters (cm^{-1}). For a beam with N incident photons, passing through a material with thickness Δx, the number of removed photons n is given by the following equation [27] [38]:

$$n = \mu N \Delta x \tag{2.11}$$

In other words, the number of photons attenuated depends on the thickness of the absorber and a "constant of proportionality"which is determined by the homogeneous properties of the absorber which will differ for different types of radiation and materials. This constant μ is known as linear attenuation coefficient and is given by:

$$\mu = \frac{\Delta N}{\Delta x} \tag{2.12}$$

where ΔN is the variation in the number of transmitted photons [40].

However for a larger thickness, it would require multiple calculations using several small thickness material Δx, and therefore, in order to simplify this process an alternative calculus can be applied. The attenuation of a monoenergetic photon beam, striking a given material with thickness x, has been experimentally determined to be an exponential process. Therefore the correlation between the number of incident photons N_0 and the number of transmitted photons N, is given by [27] [38]:

$$N = N_0 e^{-\mu x} \tag{2.13}$$

The linear attenuation coefficient is the sum of the individual contributions from each type of interaction, and given that for diagnostic energies only Photoelectric interaction and Compton Scatter contribute to energy transfer, μ is given by [27]:

$$\mu = \mu_{photoelectric\ effect} + \mu_{compton\ scatter} \tag{2.14}$$

The linear attenuation coefficient for soft tissue ranges from approximately 0.35 to 0.16 cm^{-1} for photon energies of 30 to 100 keV. For a given thickness of material, the probability of interaction depends on the number of atoms the x-rays encounter per unit distance, therefore the density (ρ, in $g.cm^{-3}$) of the material affects this number. For example, if the density is doubled, the photons will encounter twice as many atoms per unit distance through the material [27]. Therefore, the linear attenuation coefficient is proportional to the density of the material, for instance:

$$\mu_{water} > \mu_{ice} > \mu_{water\ vapor} \tag{2.15}$$

Mass attenuation coefficient (μ_m) is a measurement of the x-ray attenuation in matter and it's given by the linear attenuation coefficient μ (in units of cm^{-1}), divided by the density of the absorber ρ (in units of $g.cm^{-3}$). The mass attenuation coefficient is then given by $\mu_m = \mu/\rho$ and it is expressed in units $cm^2.g^{-1}$ [27]. In addition to the linear and mass attenuation coefficients, other two related attenuation coefficient are also used for describing photon beam attenuation characteristics: the atomic attenuation coefficient,

which is given by ${}_a\mu = \mu \backslash N_a$ (units m^2 per atom); and the electronic attenuation coefficient, which is given by ${}_e\mu = \mu \backslash N_e$ (units m^2 per electron), given that N_a is the number of atoms per volume of the absorber and N_e is the number of electrons per volume of the absorber [32].

Figure 2.11 shows two plots regarding the variation of the mass attenuation coefficient in function of the x-ray energy. For low photon energies the photoelectric effect dominates the attenuation process, however when dealing with higher photon energies and low Z_{eff} materials (e.g., tissue), Compton scattering dominates. For low photon energies, bone has the higher mass attenuation coefficient. Given that the mass attenuation coefficient is defined as $\mu_m = \mu/\rho$, the higher density of the bone, which is approximately 2 to 3 times greater than adipose or soft tissue (see Table 2.1)), further increases the bone's linear attenuation coefficient (reminding that μ is given by the mass attenuation coefficient μ/ρ multiplied by the density ρ). As the photon energy increases, the values of the mass attenuation coefficient become much lower for all tissues and for energies greater than 80 keV the difference in mass attenuation coefficients between bone and soft tissue is less than a factor of 2 [38] [27].

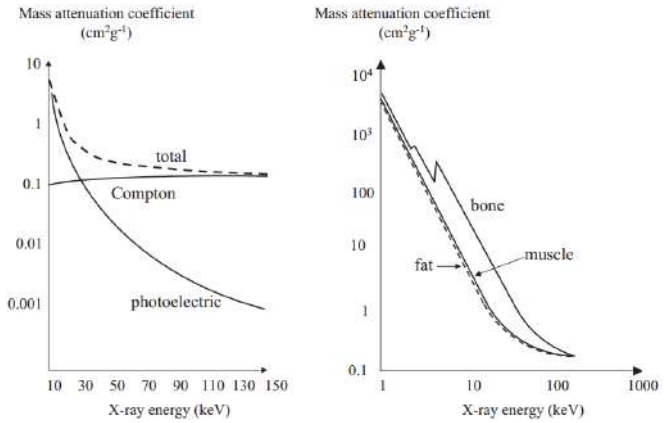

Figure 2.11: Adapted illustration of two plots. The one on the left is a plot regarding the individual contributions from photoelectric attenuation and compton scatter, adding up to a net tissue linear attenuation coefficient, represented in the plot as total (the specific data are shown for water); the one on the right is a plot regarding the mass attenuation coefficient of lipid, muscle and bone in function to the x-ray energy [38].

2.2.4.1 Cross-sections

A cross-sectional area is a measure of the probability of interaction of a given particle or photon with a secondary particle or photon. For instance, considering the electronic cross section, we can visualize the attenuation coefficient in terms of the "effective" cross sectional area of an electron in its interactions with an incoming photon. Therefore it's common to refer to attenuation coefficients in terms of *cross section*. If an atom's electron, of a given material, has a certain area or cross section for interaction with a photon, then this area multiplied by the number of electrons in a cubic centimeter of the material,

would be the total effective area of the electrons in the cubic centimeter, and this is equal to the electronic attenuation coefficient ($_e\mu$) [40].

2.2.5 X-ray dosimetry

In order to obtain medical images with x-ray imaging, there must be interactions of radiation with the human body, allowing information of the internal structures to be acquired. Dosimetry is the subject that estimates and evaluates the energy transferred by radiation to matter.

2.2.5.1 Measurements and units in photon dosimetry

The energy that is transferred as photons strike an object, is responsible for atomic, molecular and structural changes within that same object, which for instance in physiological means, can result in cell death or abnormal cell proliferation (as tumors). Therefore it is important to have dosimetric quantities and measurements for estimating and quantifying this energy deposition. Dosimetry is crucial in many aspects of the application of radiation, from diagnostic radiology to radiation protection of staff and patients [37].

In order to fully describe a radiation field, the information regarding the number of particles N, their temporal distribution and their distributions in energy and direction is required. Therefore, the measurement used to quantify a radiation field at a given point P is called ***Fluence*** **(Φ)** and it's basically a quantity that describes the number of particles or photons passing through a unit cross-sectional area. *Fluence* is expressed in units of cm^{-2} and can be calculated by:

$$\Phi = \frac{dN}{da} \tag{2.16}$$

where dN is the number of incident particles striking a unit cross-sectional area da [41].

The rate for which photons or particles pass through a unit area per unit of time, also known as the fluence rate, is called ***Flux*** **($\dot{\Phi}$)** and it's given by:

$$\dot{\Phi} = \frac{\Phi}{dt} \tag{2.17}$$

where Φ is the *Fluence* per unit of time dt. *Flux* is a useful measurement when dealing, for instance, with a photon beam that has been irradiating for long periods of time and it is expressed in units of $cm^{-2}.s^{-1}$ [27].

The ***Energy fluence*** **(Ψ)** refers to the amount of energy passing through a unit cross-sectional area. Therefore, for a monoenergetic beam of photons the *Energy fluence* is given by:

$$\Psi = \Phi \times E \tag{2.18}$$

where Φ is the *Fluence* in units m^{-2} and E is the energy per photon (energy/photon) in J, and therefore Ψ is expressed in units $J.m^{-2}$, for it is a measurement of energy per unit area [27].

Nevertheless, the first measurement established to quantify an interaction of radiation through matter, was the measurement that is associated to the ability of a photon beam to ionize air, called ***Exposure***, or more specifically ***Exposure Dose***, as it was established by the International Commission on Radiation Units and Measurements (ICRU) in 1957. More recently an alternative measurement appeared called ***Kerma*** **(***K***)** which stands for *"kinetic energy released in matter"* and it's a more general quantity recommended for dosimeter calibration purposes [37] [41]. *Kerma* is a measurement associated to the energy transferred from those uncharged particles per unit mass of matter, with SI units of joule per kilogram ($J.kg^{-1}$) or more commonly used, gray (Gy), where 1 Gy = 1 $J.kg^{-1}$ [41]. It can be determined by the following equation:

$$K = \frac{dE_{tr}}{dm} \tag{2.19}$$

where dE_{tr} is the mean sum of the initial kinetic energies of all the charged particles liberated in a mass dm of material, as a result of the incident photon interaction on dm [41].

However, for a monoenergetic photon beam with energy fluence Ψ and energy E, *kerma* can be calculated by:

$$K = \Psi \left(\frac{\mu_{tr}}{\rho_o} \right)_E \tag{2.20}$$

where $\left(\frac{\mu_{tr}}{\rho_o} \right)$ is the ***Mass energy transfer coefficient*** and it describes the fraction of the mass attenuation coefficient that gives rise to the initial kinetic energy of electrons in a small volume of absorber [27].

When *kerma* is measured in air, it is called *air kerma* and it refers to the energy absorbed in a kilogram of air. In medical imaging it is common to find *air kerma* with units of milligray (mGy), given that Gy is a rather large unit (1 mGy = 10^{-3} Gy) [37].

Nevertheless, the measurement that indicates the radiation energy imparted on a given material, or physiological matter as an organ or tissue, is the ***Absorbed Dose (D)*** or simply ***Dose***. It's the basic physical dose quantity used in radiological protection, radiation biology, and clinical radiology and it's determined by:

$$D = \frac{d\bar{\varepsilon}}{dm} \tag{2.21}$$

where $d\bar{\varepsilon}$ is the mean energy imparted by ionizing radiation, expressed in joule (J), to matter of mass dm, expressed in kilogram (kg), and therefore it has the same units as kerma, i.e., joule per kilogram ($J.kg^{-1}$) or gray (Gy). It's defined to give a specific value at any point in matter [41]. As absorbed dose is established for a specific point, in practical applications, the absorbed doses are usually an average over a large tissue volume, like an organ. Therefore the ***mean absorbed dose***, D_T, in a large volume, as an organ or a tissue T is determined by:

$$D_T = \frac{1}{m_T} \int_{m_T} D dm \tag{2.22}$$

where m_T is the mass of the organ or tissue, and dm is the mass element where D_T is being calculated. And from the equation 2.22, we can obtain the following equation, given that the mean absorbed dose D_T, is equal to the ratio of the mean energy imparted ($\bar{\varepsilon}_T$) to an organ or tissue (T) with mass m_T:

$$D_T = \frac{\bar{\varepsilon}_T}{m_T} \tag{2.23}$$

The unit of mean absorbed dose is also joule per kilogram (J.kg^{-1}), or gray (Gy) [41].

Alike kerma, absorbed dose can also be related to the energy fluence Ψ of a monoenergetic photon beam with energy E, by the following equation:

$$D = \Psi \left(\frac{\mu_{en}}{\rho_o} \right)_E \tag{2.24}$$

where $\left(\frac{\mu_{en}}{\rho_o} \right)$ is the ***Mass energy absorption coefficient***. The absorbed dose describes the fraction of the mass attenuation coefficient that accounts for the transferred energy that is locally absorbed, therefore, particles that may escape the small volume of interest are not accounted for [27].

Despite the fact that *kerma* and *absorbed dose* are expressed in the same units, they are different measurements. One of the differences lies in the volume of interest for which these quantities are measured; for kerma, the volume of interest is where energy from uncharged particles (photons) is transferred to charged particles (electrons); for absorbed dose, it is where the kinetic energy of charged particles is spent. For *kerma*, only the energy transferred regarding uncharged particle interactions within the volume is included, whereas *absorbed dose* will account for all the contributions that impart energy in the volume of interest, even if there's charged particles entering the volume that originated from a radiation coming from another distant region. However, charged particles ejected by a photon in the volume of interest may leave it, carrying away part of their kinetic energy and this energy is included in kerma but doesn't contribute to the absorbed dose [37] [41].

The biological damage caused by ionizing radiation depends on the kind of radiation in consideration. In order to take into account the effectiveness of the type of radiation in producing biological damage, the International Commission on Radiological Protection (ICRP) established a ***Radiation weighting factor*** **(w_R)**, as a part of an overall system for radiation protection. Therefore, the measurement ***Equivalent dose*** **(H)** takes into account the capability that different radiations have, of causing more or less biological damage, and is given by:

$$H_T = \sum_R w_R D_T \tag{2.25}$$

where H_T is the equivalent dose in an organ or a tissue T, D_T is the mean absorbed dose, as we've seen before w_R is the radiation weighting factor, for a given radiation R. The sum is performed over all types of radiations involved [27] [41]. The units for equivalent dose is J.kg^{-1} and it's special name is *sievert* (Sv), where 1 Sv = 1 J.kg^{-1}. Radiation used

in diagnostic imaging (photons), as well as electrons that are ejected due to interactions with the incident photons, have a w_R of 1, and therefore the equivalent dose for a photon beam is equal to the *absorbed dose* [27].

Just like there was a need to take into consideration the effectiveness of biological damage according to the type of radiation, the sensitivity of biological tissues to ionizing radiation also differs and had to be accounted for. The ICRP also established a ***Tissue weighting factor*** **(w_T)** as a part of their radiation protection system to assign each particular organ or tissue T the proportion of damage from stochastic effects from irradiation. Therefore the ***Effective Dose*** **(E)**, introduced in 1991, in ICRP *Publication 60*, is the sum of the products of the equivalent dose H_T to each organ or tissue irradiated and the corresponding weighting factor w_T for those same organs or tissues [41]:

$$E = \sum_T w_T \sum_R w_R D_T = \sum_T w_T H_T \tag{2.26}$$

The organs and tissues for which the tissue weighting factor values are specified, according to the 2007 Recommendations (ICRP, 2007) are given in Table 2.2 [41].

Table 2.2: Tissue weighting factors, w_T, according to the 2007 Recommendations (ICRP, 2007).

Tissue	w_T	$\sum w_T$
Red bone marrow, colon, lung, stomach, breast, remainder tissues[3]	0.12	0.72
Gonads	0.08	0.08
Bladder, oesophagus, liver, thyroid	0.04	0.16
Endosteum[4], brain, salivary glands, skin	0.01	0.04
Total		1.00

The units for *effective dose* is the same as for *equivalent dose*, that is *sievert* (Sv). In medical imaging it is common to find *effective* and *equivalent dose* expressed in units of mSv or μSv and *absorbed dose* in mGy or μGy, therefore w_T and w_R are expressed in mSv.mGy^{-1} [27].

2.2.5.2 Computed Tomography Dosimetry

As CT scanners grew in complexity, there was a need to ensure dosimetry systems to monitor the performance of such scanners. In this section, dosimetry systems for monitoring CT scanners and the variation used for CBCT will be discussed.

A dosimeter is a device used to measure ionizing radiation. There is a variety of dosimetric instruments [37], however we will only be addressing the one relevant for this particular project.

Ionization chambers are a type of dosimeters used in diagnostic radiology for the measurement of air kerma or air kerma rate and they are classified as active dosimeters,

[3] adrenals, extrathoracic region, gall bladder, heart, kidneys, lymphatic nodes, muscle, oral mucosa, pancreas, prostate, small intestine, spleen, thymus, and uterus/cervix.

[4] bone surface.

for the dose value is directly displayed. Some commercial dosimeters automatically perform conversion in order to display the actual air kerma value instead of the air kerma rate, due to internal sensors for measurement of the environmental temperature and pressure, and therefore perform the corrections for the air density automatically.

Ionization chambers are the standard instruments used for diagnostic radiology dosimetry as they are used for measurements involving scatter radiation (e.g., patient exit dose) and CT phantom measurements. A ionization chamber is an air filled chamber, when exposed to ionizing radiation, the air contained within the chamber is ionized, and therefore, charges are liberated and collected by an existing electric field, which is formed by a polarizing voltage across two electrodes present in the chamber. The increase in the current is measured by an electrometer[5], which is used to calculate the increased charge ($dq = idt$ units in *Coulomb*) and then multiplied by the mean energy required to produce an ion pair in dry air ($\bar{W}$ = 33,97 eV/ion pair = 33,97 J.C^{-1}), therefore resulting in the energy transferred dE_{tr} for calculating the air kerma (see equation 2.19). The cylindrical (pencil) type ionization chamber is a cylindrical ionization chamber, resembling a pencil, therefore it is also known as pencil ionization chamber, however there are several sizes and they vary in their active volumes, which range between 0.1 and 1 cm^3. They usually have an internal length not greater than 25 mm and an internal diameter not greater than 7 mm. The wall material is of low atomic number with thickness of less than 0.1 g.cm^{-2} and it has an aluminum central electrode of about $1mm$ to ensure energy dependence [30] [37]. However, CT and CBCT dosimetry systems are described in the following points:

- **CT Dosimetry:** The main dosimetry system for monitoring and evaluating dose performance in CT scans is the Computed Tomography Dose Index (CTDI). It's an *index* or indicator of the dose received by a patient undergoing a CT scan. Throughout the years it has suffered modifications and not only was enhanced and established as the standard dosimetry method for CT scans, but also has differentiated into new approaches in order to address new variations of the standard CT scanner (e.g., dose descriptor for CBCT) [27].

  The $CTDI_{100}$ characterizes a CT scanner by integrating a dose profile resulting from a single axial rotation [42]. For this, dose measurements are performed within standard Polymethyl Methacrylate (PMMA) phantoms, which is previously set up at the isocenter[6], parallel to the rotation axis. By inserting a standard cylindrical (pencil) ionization chamber with an active length of 100 mm, into the central axis and the four peripheral positions, dose measurements are acquired [43] [27]. The $CTDI_{100}$ requires integration of the radiation dose profile from a single axial scan over specific integration limits, and therefore it's defined as:

$$CTDI_{100} = \frac{1}{N \times T} \int_{-50\text{mm}}^{50\text{mm}} D(z)dz \tag{2.27}$$

[5]Device for measuring small currents of the order of 10^{-9} A [30].
[6]Center of rotation of the CT gantry.

where the integration limits are ±50 mm, which corresponds to the 100 mm active length of the pencil ionization chamber, N is the number of slices obtained in a single axial scan, T is the nominal width of a single slice, and $D(z)$ is the dose profile along the axis of a single axial rotation [43] [22].

There are two standard PMMA dosimetry phantoms, although both are 150 mm long, the adult body phantom has 32 cm of diameter and the adult head phantom has 16 cm as shown in Figure 2.12. Although only one peripheral hole is represented

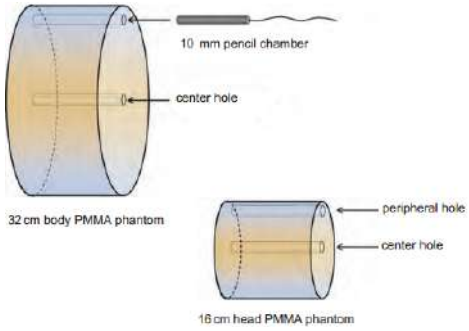

Figure 2.12: Adapted illustration of both standard PMMA dosimetry phantoms: the adult body phantom with 32 cm of diameter along with the illustration of the insertion of a pencil ionization chamber in a peripheral position (on the left); and the adult head phantom with 16 cm of diameter (on the right) [27].

in each phantom in Figure 2.12, they both have three more peripheral holes each, meaning each phantom has a total of four peripheral holes that are positioned 1 cm below the phantom's surface and 90 degrees apart. The head phantom also serves as pediatric body phantom [27].

- **CBCT Dosimetry:** A dosimetry method for monitoring and evaluating the dose delivered to a patient undergoing a CBCT scan, hasn't yet been established. There are drawbacks by using the $CTDI_{100}$ as a dosimetry system for CBCT scanners, due to the x-ray beam of a CBCT scan being sometimes wider than the active length of the 100 mm pencil ionization chamber and wider than the standard 150 mm long standard PMMA phantoms and several approaches have been proposed to overcome these drawbacks. One of these approaches state that the $CTDI_{100}$ for CBCT scan is given by:

$$CTDI_{100} = \frac{1}{W} \int_{-50mm}^{50mm} D(z)dz \tag{2.28}$$

where W is the nominal beam width of the scan and is used instead of $N.T$, given that in a CBCT scan, the Region Of Interest (ROI) is scanned with a single detector and single a rotation [43].

However, the pencil ionization chamber, of active length l, is not in fact measuring air kerma, but rather the integral of a single rotation dose profile $D(z)$, and therefore the measured value, referred to as "meter reading"is in fact the average air kerma

over the chamber length l. The meter reading is then calculated by:

$$MeterReading = \frac{1}{f \times l} \int_{-l/2}^{l/2} D(z)dz \tag{2.29}$$

where f is the f-factor [22]. When an ion chamber measurement is given in air kerma (mGy), the f-factor used depends on the material which is irradiated:

- 1.06 mGy/mGy for dose to tissue;
- 1.00 mGy/mGy for dose to air;
- 0.90 mGy/mGy for dose to PMMA [22].

Another dosimetry measurement used is a weighted $CTDI_{100}$ ($CTDI_W$) which takes into account the dose variation within the phantom, and is defined by:

$$CTDI_W = \frac{1}{3}CTDI_{100,c} + \frac{2}{3}CTDI_{100,p} \tag{2.30}$$

where $CTDI_{100,c}$ is measured at the center of the phantom and $CTDI_{100,p}$ is calculated as an average of the four measurements taken at the peripheral positions of the PMMA phantom [43].

2.2.5.3 Monte Carlo Computation

Monte Carlo (MC) is a computational technique used in x-ray dosimetry, with reference to the stochastic nature of gambling in the Principality of Monaco, Monte Carlo. MC calculations use computer simulation to study the dose deposition during x-ray exposure and are a strong alternative to experimental calculations in many areas of research, such as diagnostic and medical physics [27]. Computer programs, also known as MC codes, produce random probabilistic values which then produce a probability distribution based on these values. MC simulations compute a three-dimensional dose distribution based on the known physics of x-ray interactions as a function of the x-ray angle, energy, the geometrical model (including the simulated patient, or computational phantom, referred to further on in this section) and the random number generated. It first simulates the random emissions of the photons or particles, with the established energy and direction. The interactions and path of the radiation in the irradiated geometry are simulated by randomly choosing, from appropriate probability distributions, the values of the energy, direction, and path for those same particles or photons. Based on the physics of the interactions the particle's or photon's fate are determined by comparing interaction probabilities for every geometrical ROI. This rather extensive process is repeated for an extremely large number of particles (depending on the number of simulated particles - number of histories simulated) and each particle or photon is tracked in the 3D anatomical model and ends when it's absorbed, leaves the ROI or no longer has sufficient kinetic energy to be of interest [27] [41] [44]. Given that photons deposit energy primarily through photoelectric effect and compton scattering (regarding energies used in diagnostic radiology as

mentioned in section 2.2.3), the probability of a photon interaction occurring within an organ or tissue is determined by the cross section (discussed in 2.2.4.1), which depends on the photon beam energy ($h\nu$), the tissue electron density and the tissue chemical composition (Z_{eff} and ρ). Despite the fact that several numerical computational methods, including finite difference, finite element, discrete ordinates and MC, are able of solving radiation problems, described by various differential, integral, and integro-differential equations, only MC methods are able of accounting for all aspects of particle interactions within a three-dimensional computational phantom [44].

Given the rise of computer power in the last few years, the use of MC methods for dose estimation has increased as well as the simulations complexity, allowing many simulated photons or particles to be performed (typically 10^6 to 10^8), which reduces statistical uncertainty in the computation [27]. The statistical uncertainty can be constrained to be less than 1%, which is often more precise than experimental results from physical phantoms using a dosimeter (regarding absorbed dose). However, experiments performed with physical phantoms are needed to validate the MC calculations [44]. There are several MC code systems used to simulate radiation transport (e.g., MCNPX - Monte Carlo N-Particle eXtended [45], EGS - Electron-Gamma-Shower [46], PHITS - Particle and Heavy Ion Transport code System [47]), nevertheless we will only refer to the code used in this particular project, the PENetration and Energy Loss Of Positrons and Electrons (PENELOPE) [48], which is a code system for MC simulation of electron and photon transport. Despite the fact that in the PENELOPE acronym there's no reference to photons, this is due to photon simulations only being introduced into the code system later on [49]. The main program used for PENELOPE is penEasy, which is general-purpose, well structured, main program that includes several source models, tallies, variance reduction techniques and the possibility of combining quadric and voxelised[7] geometries [50].

As previously mentioned there are different dosimetric quantities used to calculate and measure the energy deposition, however, the quantities *equivalent dose* and *effective dose* aren't directly measurable. The evaluation of the equivalent dose and effective dose is based on the use of computational models or phantoms [41]. Various anatomically realistic models (Voxel Phantoms[8]) were developed throughout the years since the early 1980s. Thanks to computational power and medical imaging (CT and MRI) evolution, a series of so called voxel phantoms were constructed. A total of 84 phantoms were developed throughout the years, varying in their complexity, size, age specific, gender, and consisting of a whole-body or only parts (e.g., only torso and head). In the past the ICRP didn't specify a particular phantom, however, nowadays ICRP and ICRU adopted the adult male and female reference computational phantoms as the phantoms for computation of the ICRP/ICRU reference conversion coefficients and the calculation of organ and tissue absorbed doses [44].

The reference computational models are digital three-dimensional representations of

[7] Composed by voxels.

[8] The phantoms are composed of small three-dimensional volume elements.

the human anatomy based on computed tomographic data, however their organ volumes and tissue densities have been adjusted in order to approximate the reference organ masses to the data on Reference Male and Female referenced in *ICRP Publication 89 (ICRP, 2002)*, and therefore these models are computational representations of the Reference Male and Reference Female [51] [52] [53] [41]. Figure 2.13 shows frontal views of the male and female reference computational phantoms.

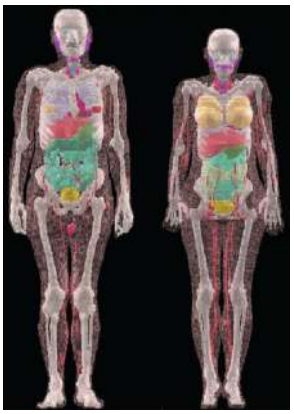

Figure 2.13: Adapted illustration of both adult male and female reference computational phantoms, based on earlier work [44].

Both reference computational phantoms contain all target regions relevant for studying human exposure to ionizing radiation and are extensively described in ICRP *Publication 110* (ICRP, 2009) [53], however we will only refer to the adult female reference computational phantom from now on, for it is the one relevant for this project in particular.

The adult female reference computational phantom is composed of approximately 3.89 million tissue voxels (excluding the voxels representing the surrounding vacuum), each with a slice thickness of 4.84 mm, which corresponds to the voxel height, and voxel depth and width of 1.775 mm, corresponding to a voxel volume of approximately $15,25$ mm^3. The body height and mass are 1.63 m and 60 kg, and it has 346 slices. The number of individually segmented structures is 136, and 53 different tissue compositions have been assigned to them, as described in Annex I [41] [53].

2.3 Medical Image Reconstruction

In this chapter we will approach the physics that underlay medical image reconstruction using CT scans. Medical imaging is an important tool in screening and diagnosing diseases, therefore the better the image quality, the more accurate the diagnosis.

The reconstruction process of CT scans is basically the process of converting raw acquired data into a series of CT images, usually reconstructed into a series of axial images. Each axial image is a 2D image made of a matrix of pixels[9], however these pixels

[9] Picture elements.

correspond in reality to a 3D cross section of the body. Therefore a 2D pixel corresponds in reality to a 3D voxel with dimensions of length and height of $\Delta x, \Delta y$ and width of Δz, as shown in Figure 2.14.

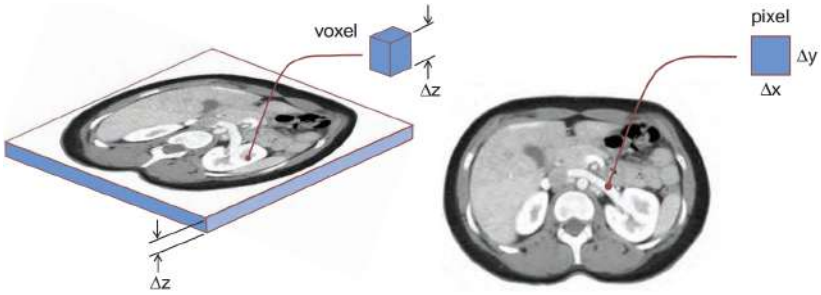

Figure 2.14: Adapted illustration of an axial CT image showing the correlation between a voxel and a pixel [27].

However, the process of obtaining the reconstructed axial CT images isn't as trivial as one may think.

As we've seen in section 2.2.4 *X-ray linear and mass attenuation coefficients* with the equation 2.13, there's a correlation between the linear attenuation coefficient, the incident x-ray beam and the thickness of the absorber. If we have a heterogeneous sample of material (e.g., the human body), we should replace the attenuation coefficient in the equation 2.13 with the integral of the attenuation coefficient over the path through which the radiation passes. For a one-dimensional path, the equation obtained is:

$$I = I_0 \, e^{-\int_0^x \mu(x)\, dx} \tag{2.31}$$

where I_0 is the initial x-ray intensity, I is the x-ray intensity after traveling a distance of x through the human body and $\mu(x)$ is the function defining the attenuation coefficient distribution along the path of the radiation, as shown in Figure 2.15.

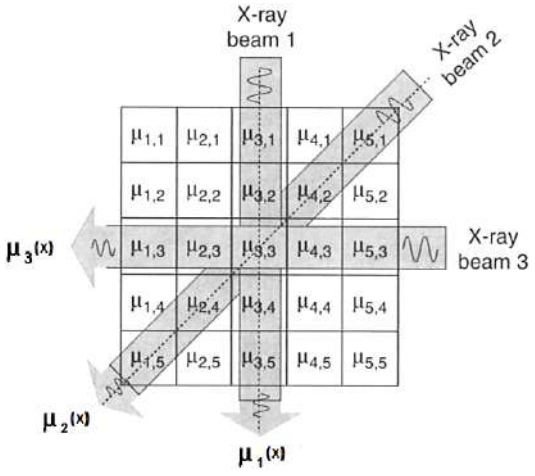

Figure 2.15: Adapted illustration of a schematic showing the attenuation coefficient distribution along the x-ray beam path [54].

By determining $\mu(x)$, it is possible to define the spacial structures within the human body in terms of the ability of its individual layers to attenuate radiation. It's possible to distinguish the body tissues in a tomographic image, given that the different tissues and organs are characterized by the distinct properties of their constituent elements and compounds (e.g., water, calcium, sodium) [31].

2.3.1 Radon Transform

To understand the physical processes involved in the x-ray imaging technique, we must first analyze the equation 2.31 from the point of view of the transmission of an x-ray beam, where $\mu(x)$ is the function defining the spacial distribution of the attenuation coefficient in the sample the radiation went through. It is the knowledge of this spacial distribution of the attenuation coefficient that makes it possible to obtain an image of the arrangement of the organs and tissues within the body and therefore diagnose a possible injury. By applying the logarithm to both sides of the equation 2.31, we obtain [31]:

$$\ln\left(\frac{I_0}{I}\right) = \int_0^x \mu(x)\, dx \tag{2.32}$$

Despite nowadays CT scanners use fan-beam geometries, and CBCT use cone-beam geometries, we will adopt a parallel-beam geometry, as shown in Figure 2.16, for it is more intuitive for the understanding of the reconstruction techniques and mathematically simpler.

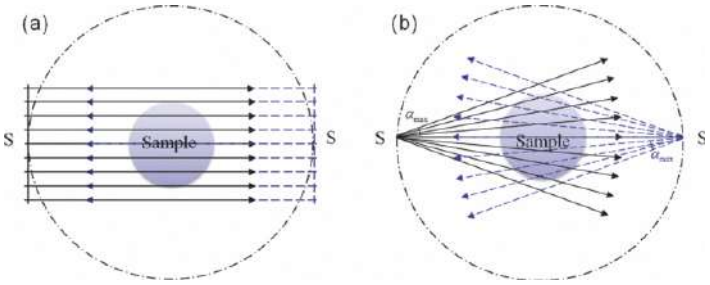

Figure 2.16: Adapted illustration of two different beam geometry. A parallel-beam geometry is represented in a), as for b) represents a fan-beam geometry [55].

Therefore, with the parallel-beam geometry, for each position S of the source, the x-ray beams travel parallel to each other and they all strike the detector perpendicularly, originating a projection, which is the image produced on the detector by the transmitted x-rays, after these have passed through the patient's body. Figure 2.17 shows how each acquired data, regarding the attenuation coefficient along the path of the incident x-ray, gives form to a projection acquired at a given angle θ. This data is given by a function $p(s,\theta)$ that depends on the angle θ, which is the angle for the projection acquisition, and s which is the distance from the center of rotation to the path through which each x-ray beam passed through, and $f(x,y)$ is the function that describes the object through the coordinates (x,y) [31] [57]. In this case a new coordinate system (s,u) is defined, by

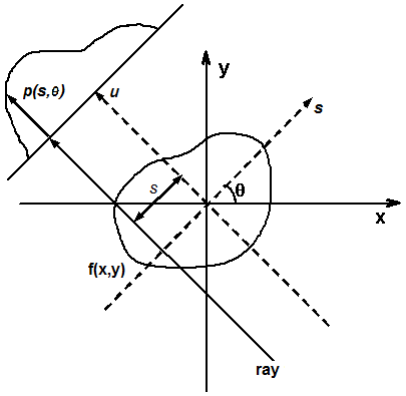

Figure 2.17: Adapted illustration of the acquisition of a projection, specifying the data acquisition $p(s,\theta)$, as a result of a given ray passing through an object $f(x,y)$ [56].

rotating (x,y) over the angle θ, giving the following transformation formulas [34]:

$$\begin{bmatrix} s \\ u \end{bmatrix} = \begin{bmatrix} \cos\theta & \sin\theta \\ -\sin\theta & \cos\theta \end{bmatrix} \begin{bmatrix} x \\ y \end{bmatrix}$$
$$\begin{bmatrix} x \\ y \end{bmatrix} = \begin{bmatrix} \cos\theta & -\sin\theta \\ \sin\theta & \cos\theta \end{bmatrix} \begin{bmatrix} s \\ u \end{bmatrix} \tag{2.33}$$

When θ assumes a fixed value, the measured intensity profile as a functions of s is given by:

$$\begin{aligned} I_\theta(s) &= I_0\, e^{-\int_{L_{s,\theta}} \mu(x,y)\, du} \\ &= I_0\, e^{-\int_{L_{s,\theta}} \mu(s.\cos\theta - u.\sin\theta, s.\sin\theta + u.\cos\theta)\, du} \end{aligned} \tag{2.34}$$

where $L_{s,\theta}$ is the line that makes an angle θ with the y-axis at a distance s, in other words, it is the trajectory through which the ray passed through. Each intensity profile can be converted into an attenuation profile, therefore:

$$\begin{aligned} p_\theta(s) &= -\ln \frac{I_\theta(s)}{I_0} \\ &= \int_{L_{s,\theta}} \mu(s.\cos\theta - u.\sin\theta, s.\sin\theta + u.\cos\theta)\, du \end{aligned} \tag{2.35}$$

where $p_\theta(s)$ is the projection of the function $\mu(x,y)$ along the fixed angle θ that can assume values from 0 to 2π [34].

Consequently, various projections $p(s,\theta)$ for the various angles θ are acquired and by stacking all these projections, we obtain a 2D data-set of $p(s,\theta)$ called ***sinogram***, as shown in Figure 2.18. The transformation of any function $f(x,y)$ into its ***sinogram*** $p(s,\theta)$, in mathematics is called the ***Radon transform***. Essentially it's given by the equation 2.35, however, formally structured for any function $f(x,y)$, it takes the following form [34] [57]:

$$\begin{aligned} p(s,\theta) &= \mathcal{R}\{f(x,y)\} \\ &= \int_{-\infty}^{\infty} f(s.\cos\theta - u.\sin\theta, s.\sin\theta + u.\cos\theta)\, du \end{aligned} \tag{2.36}$$

Figure 2.18: Adapted illustration of a sinogram, which is a 2D data-set $p(s,\theta)$ [34].

for $-\infty < s < \infty$, $0 \leqslant \theta < \pi$.

2.3.1.1 Sinogram

As previously mentioned a sinogram is the result of the ***Radon transform*** when applied to any function $f(x,y)$ describing any object. A sinogram is essentially a 2D data-set $p(s,\theta)$ obtained through the stacking of all the projections $p_\theta(s)$ acquired for all angles θ. For instance, the Figure 2.19 shows how a sinogram is obtained. As the x-rays pass through the object, represented as a red dot, a projection is obtained and the data regarding the attenuation coefficient distribution along the path of the radiation is stored in the location represented by a white square. This process is repeated for different angles of

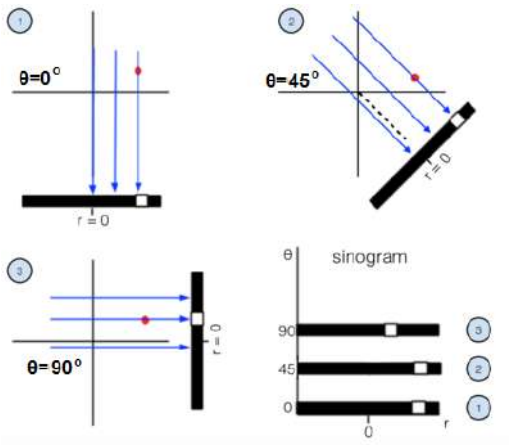

Figure 2.19: Adapted illustration of an schematic describing in simple terms, the formation of a sinogram, showing the stacking of all the projections $p_\theta(s)$ acquired [58].

θ as shown in 1, 2 and 3. The sinogram is then obtained when the projections, in this case for $\theta = \{0, 45, 90\}$, as shown by the white squares, which start to assume a sinusoidal shape, explaining the origin of the name sinogram [34] [38].

2.3.2 Backprojection

Given the sinogram $p(s,\theta)$, the goal is to obtain the distribution $\mu(x,y)$, or, more precisely the function $f(x,y)$. Previously it was shown that to produce projection values,

knowing the content of the image, the straightforward process of forward projection is used. The reverse problem, computing the image matrix from the projections values, can be solved by backprojection. This is, considering an x-ray path (s,θ) that has a value of $p(s,\theta)$, by assigning a value to each point (x,y) along that path, and repeating this process for θ ranging from 0 to π, it is possible to know what value is attributed to each value of the image matrix. Mathematically, backprojection is given by:

$$\begin{aligned} b(x,y) &= \mathcal{B}\{p(s,\theta)\} \\ &= \int_0^{\pi} p\left(x.\cos\theta + y.\sin\theta, \theta\right) d\theta \end{aligned} \tag{2.37}$$

However, the measured projections are simply smeared back into the image matrix to compute the backprojection image, resulting in a blurred image, when compared to the original. The discrete version of the backprojection is given by:

$$\begin{aligned} b(x_i,y_i) &= \mathcal{B}\{p(s_n,\theta_m)\} \\ &= \sum_{m=1}^{M} p\left(x_i.\cos\theta_m + y_j.\sin\theta_m, \theta_m\right) \Delta\theta \end{aligned} \tag{2.38}$$

Nevertheless, the values $(x_i\cos\theta_m + y_j\sin\theta_m)$ generally do not coincide with the discrete positions s_n, as shown in Figure 2.20, and therefore ***Interpolation*** is required. The inter-

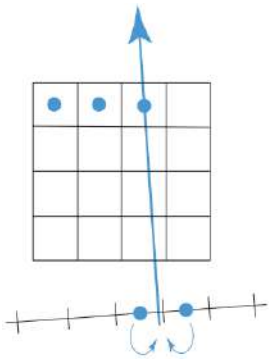

Figure 2.20: Adapted illustration showing that the discrete positions on the detector doesn't coincide with the line (s,θ). Therefore the intersection of the beam's path (s,θ) with the detector is computed and the corresponding projection value is calculated by interpolation between its neighboring measured values [34].

section of the line (s,θ) (given by beam's path), with the detector array is then computed, and the corresponding projection value is calculated by interpolation between its neighboring measured values [34] [27].

Reconstructing an image using backprojection will result in a characteristic $1/r$ blurring of the image, where r is the distance of a given point P, located on the line (s,θ), to the center of rotation of the object as shown in Figure 2.17. This can be corrected applying a mathematical filtering operation, which will be discussed in section 2.3.3 *Filtered Backprojection* [27] [57].

2.3.2.1 Interpolation Methods

Interpolation is a mathematical process of using known data to estimate values at unknown locations. There are various interpolation methods, however we will only address the *Linear* and *Cubic* interpolation method, for they were the most relevant for this project.

- **Linear Interpolation:** For this interpolation method, the values considered to be the four nearest neighbors are used in the calculations to estimate the desired value. If (x, y) correspond to the position to which the value $v(x, y)$ is to be estimated, the linear interpolation is given by:

  $$v(x, y) = ax + by + cxy + d$$

  where,a, b, c and d are four coefficients determined from the four equations in four unknowns that can be written using the four nearest neighbors of point (x, y) [59];

- **Cubic Interpolation:** This interpolation method is very similar to the previous one, however it has a higher complexity given that it involves the sixteen nearest neighbors of a point. The value $v(x, y)$, is estimated by:

  $$v(x, y) = \sum_{i=0}^{3} \sum_{j=0}^{3} a_{ij} x^i y^j$$

  where the sixteen coefficients are determined from the sixteen equations in sixteen unknowns that can be written using the sixteen nearest neighbors of point (x, y) [59].

2.3.3 Filtered Backprojection

The process of backprojection has an inherent problem resulting in the $1/r$ blur function as previously mentioned, however this effect can be reduced by applying an appropriate filter function to each projection before backprojection and it's applied via convolution[10] [34].

Mathematically speaking, the function $f(x, y)$ can be reconstructed by backprojecting $p^*(s, \theta)$, which is the inverse 1D Fourier Transform with respect to k of $P^*(k, \theta)$. The function $P^*(k, \theta)$ is obtained by multiplying $P(k, \theta)$ by the filter function $h(s)$ which is represented as $H(k)$ in the Fourier domain. This explains the name Filtered Backprojection (FBP). Given that the mathematical process of convolution is computationally intensive and time consuming, the filtered backprojection is carried out in the spatial frequency domain (also known as Fourier domain), using fast Fourier transform methods. A multiplication in the Fourier domain corresponds to a convolution in the original domain (also called spatial domain) and a multiplication is much less time consuming than a convolution [34] [38] [57]. Therefore the reconstruction scheme is given by [34]:

[10] Is an integral calculus procedure that mathematically describes the effect of the blurring process [27].

1. Filter the sinogram $p(s,\theta)$:

$$\forall\theta \quad p^*_\theta(s) = p_\theta(s) * h(s), \text{ or} \tag{2.39}$$

$$P^*_\theta(k) = P_\theta(k) \cdot H(k) \tag{2.40}$$

2. Backproject the filtered sinogram $p^*(s,\theta)$ [34]:

$$f(x,y) = \int_0^\pi p^*(x\cos\theta + y\,sin\theta, \theta)\, d\theta \tag{2.41}$$

The filter applied can differ according to the image it's applied to. A *ramp filter* or also known as ***Ram-Lak*** filter $|k|$, isn't the most useful filter due to it's divergent properties. Given that for discrete projection data, the useful Fourier content is limited to frequencies smaller than k_{max}, the *Ram-Lak* filter $|k|$ is limited to those frequencies and cut off at k_{max}. This filter is the result of the difference between a block and a triangle function as shown in Figure 2.21 [34]. However this filter is very sensitive to the noise in the projections,

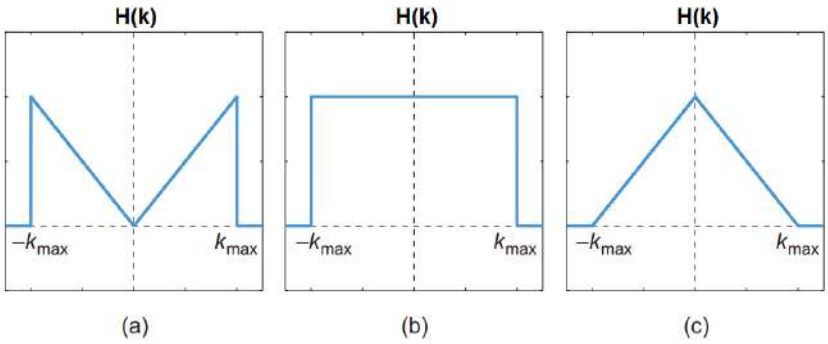

Figure 2.21: Adapted illustration of three filter plots. (a)*Ram-Lak* filter, which results from the difference between a block function (b) and a triangle function (c) [34].

due to the high frequencies it doesn't cut off. Therefore, other filters are also often used to suppress these high frequencies. Table 2.3 lists other filters frequently used. and how these filters are obtained from the *Ram-Lak* filter, and Figure 2.22 shows the different functions of the filters and how these filters cut-off high frequencies when applied. For the filters *Hamming* and *Hanning*, they are given by [34] [60]:

$$H(k) = \begin{cases} \alpha + (1-\alpha)\cos\left(\dfrac{\pi\, k}{k_{max}}\right) & \text{for} \quad |k| < k_{max} \\ 0 & \text{for} \quad |k| \geqslant k_{max} \end{cases} \tag{2.42}$$

2.3.4 Inverse Radon Transform

Another way to solve the problem of obtaining the distribution $\mu(x,y)$, or, more precisely the function $f(x,y)$ from the sinogram $p(s,\theta)$ is by inverting the process of Radon

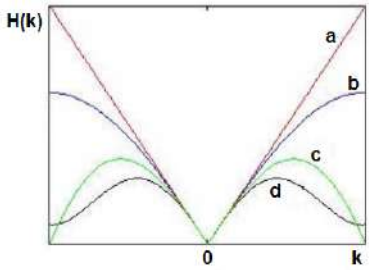

Figure 2.22: Adapted illustration of the filters: (a) *Ram-Lak* (b) *Shepp-Logan* (c) *Cosine* and (d) *Hamming* [61].

Table 2.3: Filters used for frequency domain filtering following a description of how they are obtained [60].

Filter	Description
Shepp-Logan	Multiplies the *Ram-Lak* filter by a *sinc*[11] function.
Cosine	Multiplies the *Ram-Lak* filter by a *cosine* function.
Hamming	Multiplies the *Ram-Lak* filter by a window with $\alpha = 0.54$.
Hanning	Multiplies the *Ram-Lak* filter by a window with $\alpha = 0.5$.

transform, therefore a mathematical equation for the inverse Radon transform is needed:

$$f(x,y) = \mathcal{R}^{-1}\{p(s,\theta)\} \tag{2.43}$$

A solution to this is by the ***Projection Theorem***, also known as ***central slice theorem***. Given $F(k_x,k_y)$ which is the 2D Fourier Transform (FT) of $f(x,y)$, described by:

$$F(k_x,k_y) = \int_{-\infty}^{\infty}\int_{-\infty}^{\infty} f(x,y)\, e^{-2\pi i(k_x x + k_y y)}\, dx\, dy \tag{2.44}$$

and $P_\theta(k)$ the 1D FT of $p_\theta(s)$

$$p_\theta(k) = \int_{-\infty}^{\infty} p_\theta(s)\, e^{-2\pi i(k.r)} \tag{2.45}$$

for which θ is variable, and then $P_\theta(k)$ becomes a 2D function $P(k,\theta)$. The projection theorem states that:

$$P(k,\theta) = F(k_x,k_y) \tag{2.46}$$

$$\text{with} \quad \begin{cases} k_x = k.\cos\theta \\ k_y = k.\sin\theta \\ k = \sqrt{k_x^2 + k_y^2} \end{cases} \tag{2.47}$$

this is, the 1D FT with respect to variable s of the Radon transform of a 2D function is the 2D FT of that function. Therefore, based on all the projections $p_\theta(s)$, $0 < \theta < \pi$, it's possible to obtain $f(x,y)$ for each point (x,y) [34] [27].

[11] The Fourier transform of a rectangular function is a *sinc* function [57].

2.3.5 Image Quality

After a medical image is yielded, it's important to access image quality in terms of determining how well it conveys anatomical and/or functional information to the physician, contributing to an accurate diagnosis, for the accuracy of a clinical diagnosis depends critically upon image quality. However diagnostic medical images involving ionizing radiation require important trade-offs in which image quality is not necessarily maximized, but rather optimized to assess in the diagnostic task. In order to evaluate in a quantitative manner a medical image, the three most important criteria to take into account are: spatial resolution, Signal-to-Noise Ratio (SNR) and Contrast-to-Noise Ratio (CNR). However, in the following section we will only address CNR for it is the only measurement for assessing image quality relevant for this project [27][38].

2.3.5.1 Contrast-to-noise ratio

Although the SNR of a given image might be very high, it's only diagnostically useful if it has a CNR high enough to distinguish between different tissues, more precisely between healthy and pathological tissue. The CNR is a measure of the signal level in the presence of noise and is defined as:

$$CNR = \frac{\left|\bar{x}_s - \bar{x}_{bg}\right|}{\sigma_{bg}} \tag{2.48}$$

where $\bar{x_s}$ is the average gray scale in a ROI defined inside an object, $\bar{x_{bg}}$ is the average gray scale in a ROI defined in the background and σ_{bg} is the standard deviation of the background. This metric is most suitable when test objects generate a homogeneous signal(when the mean gray scale in the signal ROI is representative of the entire object), given that CNR is determined using the difference between mean values of the signal region and background region. Some examples of the use of this metric include optimizing the kV of an imaging study to maximize bone contrast at a fixed dose level or computing the dose necessary to achieve a given CNR for a given object [38] [27].

One of the main factors that affects the CNR causing its reduction is the relative contribution of Compton scattered x-rays. The probability of Compton scattering occurring depends not only, as previously mentioned, on the x-ray energy, but also on the thickness of the body part being imaged. The thicker the section, the larger the contribution from Compton scattered photons, and therefore the lower the number of x-rays detected [38].

CHAPTER 3

METHODOLOGY

In this chapter the procedures and the different steps leading to the development of this project are described, as well as all the software programs and methods applied. This project can be divided into two core milestones: the 3.1 *Monte Carlo Methods*, and the 3.2 *Image Reconstruction*, which are the two following sections that will be addressed and explained.

3.1 Monte Carlo Methods

This section is divided into three main subsections. On the first subsection, 3.1.1 *Geometrical Model Construction*, are described the calculations regarding the construction of the quadric geometry used for the MC simulations; in the second subsection, 3.1.2 *Monte Carlo Simulations*, are described the MC code system used, regarding the source model and tallies for acquiring the projections and dose values and in the last subsection, 3.1.3 *Validation of the MC simulations* the methods for validating those same simulations are described and explained.

3.1.1 Geometrical Model Construction

In order to run MC simulations for CBCT projection acquisition and obtain absorbed dose values, the adult female reference computational phantom was employed. The dimensions of the flat panel detector and the distance of the detector to the phantom were determined according to the FOV. Therefore, in order to optimize the FOV for acquiring images simultaneously of the lung and breast, not only did a Central Point (CP) within the computational phantom be established, but also the detector dimensions were determined.

The CP was established based on the orientation of the three-dimensional voxels regarding the organs of interest (lungs and breast), listed in the ICRP *Publication 110* (ICRP, 2009) [53]. Table 3.1 lists the centers of mass in terms of coordinates of those organs for the adult female reference computational phantom.

Table 3.1: Centers of mass of the organs of interest: Breasts and Lungs, for the adult female reference computational phantom [53].

Organ ID	Organ/tissue	Center of mass Coordinates (cm)		
		x	y	z
62	Breast, left, adipose tissue	33.68	6.39	131.20
63	Breast, left, glandular tissue	34.56	6.47	130.10
64	Breast, right, adipose tissue	20.25	6.44	131.10
65	Breast, right, glandular tissue	19.29	6.10	129.40
96	Lung, left, blood	31.91	17.40	130.20
97	Lung, left, tissue	32.87	15.54	131.70
98	Lung, right, blood	21.93	15.69	130.00
99	Lung, right, tissue	21.03	14.41	131.00

By calculating the average of the coordinates of the adipose and glandular tissues for each left and right breast, and also calculating an average of the left and right lung tissue, we obtained the following coordinates, as described in Table 3.2

Table 3.2: Coordinates of the centers of mass for each organ of interest: Breasts and Lungs after calculating the average for both organs and the coordinates for the Central Point.

Organ/tissue	Center of mass Coordinates (cm)		
	x	y	z
Left Breast	34.12	6.43	130.65
Right Breast	19.77	6.27	131.25
Lung tissue	26.95	14.98	131.35
Central Point	26.95	14.98	131.30

Despite the fact that the average value regarding the y axis for the breast tissue ($y = 6.35$) differs from the one of the lung, it was decided that the coordinates for the CP would be those of the lung, given that it's the most voluminous of the two organs.

The dimensions regarding the detector were 40 cm of height, 64 cm of length and 0.025 cm of thickness and the projections were acquired for a full 360° rotation differing by 10° which makes a total of 36 projections that were acquired. Figure 3.1 shows a schematic of the geometry used for the projection acquisition in which the distances from the source to the CP and from the CP to the detector are shown.

The position for both flat panel detector and source regarding each angle were calculated by assuring that the detector and the x-ray source were centered with the CP and that the detector was perpendicular to the computational phantom.

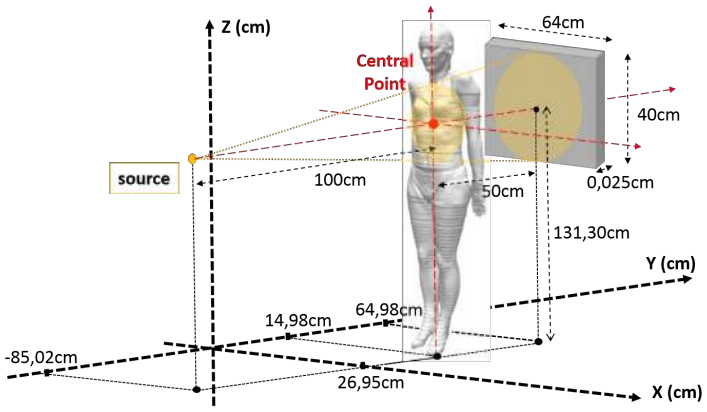

Figure 3.1: Illustration of the geometry regarding the distances and dimensions used for the MC simulations. The coordinate system is represented in black and represented in red is the rotational coordinate system with it's origin on the CP.

Given that the coordinate system for the adult female reference computational phantom isn't centered within the phantom, calculations had to be done to determine the correction values (which we will refer to as "shifts") in order to guarantee that the rotation of the source and the detector was made relative to the CP and not to the origin of the coordinate system. In Figure 3.1 the coordinate system for the computational phantom is represented in black (which we will refer to as **Original Coordinate System**), as for the coordinate system for which the rotations will occur (which we will refer to as **Rotational Coordinate System**) is represented in red and it's origin is the CP. The calculations and methodology for determining the shift values are described in Appendix A, A.1. As for the methodology for calculating the source position and direction for each acquisition angle, they are described in Appendix A, A.1.0.1.

3.1.2 Monte Carlo Simulations

MC simulations where performed using the code system PENELOPE and the main program penEasy (v.2015-05-30). In order to operate, the system requires a configuration file (penEasy.in) and the usual PENELOPE data files (geometry and materials). Three types of simulations were carried out, being one type performed with the Computational Phantom, another type performed with the PMMA phantom and a last one performed with "no phantom", nevertheless these simulations are further described in the following sections 3.1.2.1, 3.1.2.2 and 3.1.2.3 respectively.

3.1.2.1 MC Simulations with Computational Phantom

In order to run MC simulations using the adult female reference computational phantom, this is, for simulating the CBCT model, geometry data files and configuration files were constructed and defined for each acquisition angle. In the folowing points each file is described and explained.

- **Geometry Data File:**

  Quadric geometries are defined by means of the package PENGEOM, which is included in the PENELOPE distribution. The quadric geometry file is entered in the field `QUADRICS FILE NAME` of the configuration file as presented in Appendix B, B.2. The elements (surfaces, bodies, modules) used in the geometrical model are introduced through a plain text file, named with an extension ended in GEO, according to the syntax described in the PENELOPE manual [49]. Bodies are homogeneous geometries, limited by well-defined quadric surfaces used to describe any material system. Modules are connected volumes, limited by quadric surfaces, that contain one or several bodies and are used to maximize time efficiency, by grouping the bodies of a material system into modules.

  The geometry data file for describing the geometrical model of the CBCT for an angle acquisition of 10° scan used for the simulations, can be found in Appendix B.1, where four main bodies were considered:

  - `BODY 1`: Detector;
  - `BODY 2`: Microcalcification in the left breast;
  - `BODY 3`: Microcalcification in the left lung;
  - `BODY 4`: Sphere defined as the "transparent body";
  - `BODY 5`: Sphere of air;

  Body 2 and 3, which are the microcalcifications in the left breast and left lung, were introduced for further image quality analysis. Their positioning within the the female reference computational phantom was done according to the coordinates for the center of mass of the respective organs, as previously shown in Table 3.1, section 3.1.1 *Geometry construction*. Therefore, the coordinates for the left lung microcalcification were the same as those of the center of mass for the Left Lung Tissue, as shown in Table 3.1. For the left breast microcalcification, the coordinates used were those of the Left Breast as previously shown in Table 3.2. The microcalcification in the lung is a sphere with radius of 0.7 cm as for the breast it's also a sphere, however with a radius of 0.4 cm.

  Body 4 is a sphere of air with radius of 400 cm, defined as "transparent body", in order to contain the other three previous bodies and the voxelized geometry (the female reference computational phantom). Given that the quadric geometry is the dominant one, it covers the voxelized geometry, making it 'invisible' to the transport routines. Therefore it required a unique quadric body identified as the 'transparent' body, for the voxels to become visible to the transport routines.

  Body 5 is a sphere of air with radius of 600 cm only containing the detector. This sphere is responsible for the detector rotation and therefore the rotation angle `OMEGA` is set for `-10DEG` performing a clockwise rotation of 10°. The shift values

explained in Appendix A listed in Table A.4 are introduced in the fields `X-SHIFT` and `Y-SHIFT`, and `Z-SHIFT` is maintained as `0.00`.

The materials used in the voxelized geometry file (VOX file constructed using FORTRAN code [62]) and listed in the configuration file in `[SECTION PENELOPE]`, were created according to the the elemental compositions and densities for the adult female reference computational phantom listed in Annex I [41]. The last five materials listed in the configuration file were created. Calbreast.mat and Calcification.mat are the materials of the microcalcifications of the breast and lung respectively, and their composition is listed in Table 3.3. The materials Airmodule.mat and Airtransp.mat are air and their composition were read from the file pdcampos.pen which is a file with 280 pre-defined materials [49]. The material Se.mat was also read from the same file and it's composition is Selenium.

Table 3.3: Composition of the microcalcifications inserted into the left breast and left lung, fraction by weight of element and mass density.

Composition	F_9	Ca_{20}	Density (g.cm^{-3})
Microcalcification	4.86672E-01	5.13328E-01	1.550E+00

- **Configuration File:**

The configuration file, penEasy.in is an input file where the data for penEasy is introduced and it has a defined structure, as shown in Appendix B.2. This file is divided into six main sections for simulation configuration which start with a small instruction description. Each one is structured into sections starting with a string of the type `[SECTION...]` and each section may be divided into subsections. The sections are further explained in Appendix B.3 as well as the entries for each subsection. Additional information regarding other sections can be consulted in [49] [50] [63]. It is important to refer that the simulation terminates when any of the following points are accomplished:

1. the requested `NUMBER OF HISTORIES` is reached;
2. the `ALLOTED TIME` has concluded;
3. the requested relative uncertainties of all the active tallies have been reached.

Therefore these entries must be set according to the desired simulation, given that they control the ceasing of the simulation. The simulations were performed for all 36 angles and therefore, each angle had a configuration file (e.g., penEasy10.in) and a geometry file (e.g., geometry10.geo), where the main differences between each simulated angle reside in the following entries:

- Configuration file:

* `COORDINATES OF BOX CENTER`: The coordinates for the source position were introduced according to the angle being simulated, as listed in in Appendix A, Table A.5, under the entry "Rotational Coordinate System";
* `DIRECTION VECTOR`: Appendix A, Table A.6;
* `QUADRICS FILE NAME`: Each simulation performed for each angle has it's own geometry data file.

– Geometry file:

* Body 5: The shift values were introduced according to the angle in cause, listed in Appendix A, Table A.4.

Additionally, all simulations for all 36 angles were once more performed, however, for this second batch of 36 simulations, the source's energy spectrum was set for a monochromatic beam of 30 keV. After performing a MC simulation two output files are given by both Energy Deposition and Imaging Detector tallies, the tallyEnergyDeposition.dat and tallyPixelImageDetectEI-matrix.dat respectively. Therefore from each simulated angle, for both energies (30 and 80 keV), the energy deposited per simulated history (eV/hist) for each discriminated material is obtained. The absorbed dose in both organs of interest (breast and lung) were calculated, given that:

$$Dose\,(\text{mGy/hist}) = \frac{EnergyDeposition(eV/hist) \times 1,602 \times 10^{-19}}{TissueMass\,(\text{kg})} \times 1000 \qquad (3.1)$$

3.1.2.2 MC Simulations with PMMA Phantom

MC simulations of a $CTDI_{100}$ measurement model using a PMMA phantom were performed by using the same code system and main program as the one used for simulating the CBCT scan model. Therefore a geometry and a configuration data files were defined and are listed in Appendix C. Figure 3.2 illustrates a schematic of the $CTDI_{100}$ model used in the simulations, as well as the configuration based on which the geometry for the simulated ionization chamber was defined. The patient's table was defined with a thickness of 2.5 cm and consisting of Teflon defined as polytetrafluoroethylene [49].

These simulations were performed for five different geometries regarding the ionization chamber's position within the PMMA phantom (center, 0° , 90° , 180° and 270° probe hole positions) and for four different irradiation angles (0° , 90° , 180° and 270°) for a total of 20 simulations. The source position for the simulations is listed in Appendix A.5, according to the angle of irradiation of the PMMA.

In Figure 3.3 the simulated geometry model with the ionization chamber positioned in the center is represented, using the quadratic geometry viewing program gview2D. However, some materials had to be replaced by Air material in order to maximize the time efficiency of these simulations. Therefore the materials Aluminum and Carbon Fiber were replaced by Air. For dose assessment the Energy Deposition file was analyzed regarding the discriminated material of sensitive air chamber.

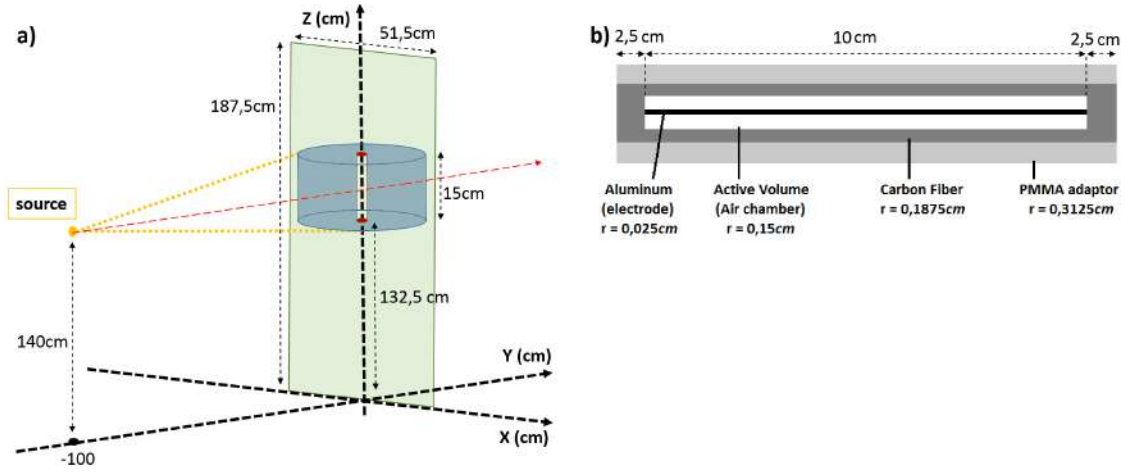

Figure 3.2: **a)** Schematic of the $CTDI_{100}$ geometry model used with an irradiation angle of 180° and for the position of the ionization chamber within the center probe hole. The patient's table was also considered in the geometry model. **b)** Configuration of a pencil ionization chamber based on which the simulated geometry model for the ionization chamber was defined.

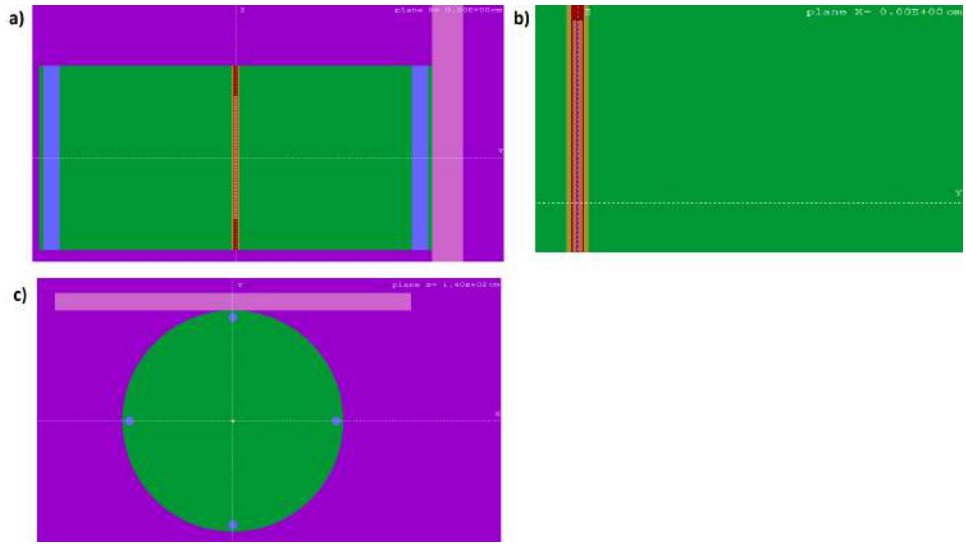

Figure 3.3: Visualization of the simulated $CTDI_{100}$ measurement model using Gview2D. **a)** Cross section of the simulated geometry model at plane x=0, where two probe holes appear in blue, the patient table appears in purple, in the middle appears the ionization chamber and in green is the PMMA phantom. **b)** A closeup visualization of the previous image, with emphasis to the central probe hole where the ionization chamber is positioned. **c)** Cross section visualization of the plane z=140.

Subsequently the data acquired from the simulations of the PMMA model (the Energy Deposition file) were analyzed in terms of validating the the MC simulations as described further in section 3.1.3.

3.1.2.3 MC Simulations with "no Phantom"

Two more batches of simulations were performed as they were helpful for accomplishing the Image Reconstruction milestone. In both of these simulations the computational

phantom was not used.

The first batch was performed using a geometrical model which only contained the air material. For this case, given that we were only simulating air, and in order to maximize the time efficiency, only one angle was simulated, the 360° angle, for both 30 keV and 80 keV energies and therefore only two tallies were obtained for each simulated energy (the tallyPixelImageDetectEI-matrix.dat files). The importance of this data will be further explained in section 3.2.1.

The second batch was performed using a geometrical model which only contained both microcalcifications of the breast and lung, and air. For this case, the simulations were performed with a 30° increment for each projection, resulting in a total of 12 projections.

3.1.3 Validation of the MC Simulations

The MC model previously described was validated by validating the simulated PMMA phantom model. For this, $CTDI_{100}$ experimental measurements were acquired and compared not only to other experimental measurements reported in the bibliography but also to the $CTDI_{100}$ obtained through the MC simulations. These calculations are further explained in the following section 3.1.3.1.

3.1.3.1 CBCT Dose Measurements

For the $CTDI_{100}$ measurements, a kV imaging system used for acquiring CBCT scans for IGRT, was employed. The kV system is incorporated into a Varian TrueBeam linear accelerator operating at the Champalimaud Clinical Centre (CCC) in Lisbon, Portugal.

In the clinic there are three CBCT scanning protocols used for IGRT: head, thorax and pelvis; however, for the CBCT dose measurements only the thorax protocol was employed. These protocols are performed with parameters (tube voltage, exposure, number of projections) that are provided by the manufacturer. With the thorax protocol the acquisition mode used is Half-fan (implying that the detector is shifted to the side relatively to the isocenter), the trajectory is a full 360° scan, and a titanium filter. The tube voltage is set for 125 kV and the exposure for 270 mAs and the collimator blades were set at $(X_1; X_2; Y_1; Y_2) = (-24.7; +3.4; -10.7; +10.7)$.

The standard PMMA adult body phantom was set at Source-Isocentre-Distance (SID) of 100 cm and a pencil ionization chamber was used for measuring the air kerma. The pencil ionization chamber used was the hybrid ion chamber designed by *RaySafe* which has the following dimensions: 200x20x12 mm, a diameter of 7,5 mm and an active length of 100 mm. Three sets of measurements were registered for each position of the ionization chamber within each of the five probe holes and an average value for each set of measurements was calculated.

From the Equation 2.29 in section 2.2.5.2 *Computed Tomography Dosimetry* we obtain

the following equation:

$$\int_{-50mm}^{50mm} D(z)dz = MeterReading \times f \times l \tag{3.2}$$

where $l = 100$ mm. And therefore the $CTDI_{100}$ is given by:

$$CTDI_{100} = \frac{1}{W} \times MeterReading \times f \times l \tag{3.3}$$

where $f = 0,90$ mGy.mGy^{-1}. Given that the dimensions of the beam width were $(Y_1; Y_2) = (-10.7; +10.7)$, we considered $W = 214$ mm.

The $CTDI_W$ was also calculated according to the Equation 2.30 in section 2.2.5.2 *Computed Tomography Dosimetry*.

3.2 Image Reconstruction

This section is divided into three main subsections. On the first subsection, 3.2.1 *From Projections to Reconstructed Images* the processing of the acquired projection's data and the reconstruction algorithms used to obtain axial CT images are described; in the second subsection, 3.2.2 *Image Quality Analysis*, the method for analyzing the image quality of the obtained axial images is explained; and in the last subsection, 3.2.3 *Validation of the reconstruction algorithm*, the methods used for validating the developed algorithm are discussed.

3.2.1 From Projections to Reconstructed Images

The output file of the Pixelated Imaging Detector Tally (tallyPixelImageDetectEI-matrix.dat) which comes in a matrix report format with the data regarding the image signal for each pixel, was transformed into a text data matrix file.

The following procedures were performed using the software Matrix Laboratory (MATLAB) which is a programming platform that uses a matrix-based language. The import of the data matrix for each angle into the MATLAB workspace was accomplished using the code listed in Appendix D. The data matrices were also transformed into their transpose, this resulted in data matrices of 600x500 for each acquisition angle. Additionally, for data analysis and processing simplification, these matrices were loaded into a structure named `MATRIZ3D` with dimensions 600x36x500 as shown in Figure 3.4, using the code listed in Appendix D.2.

The data acquired from the simulation only containing air, as previously described in 3.1.2.3 *Simulation with no computational phantom*, was replicated to obtain a total of 36 projections only containing air. The data of these air projections was also loaded to a structure of matrices, by following the same procedure as previously described, resulting in the structure `MATRIZ3D_AR`. From the Equation 2.32 in section 2.3.1 *Radon Transform* we can isolate the spatial distribution of the attenuation coefficient on one side of the

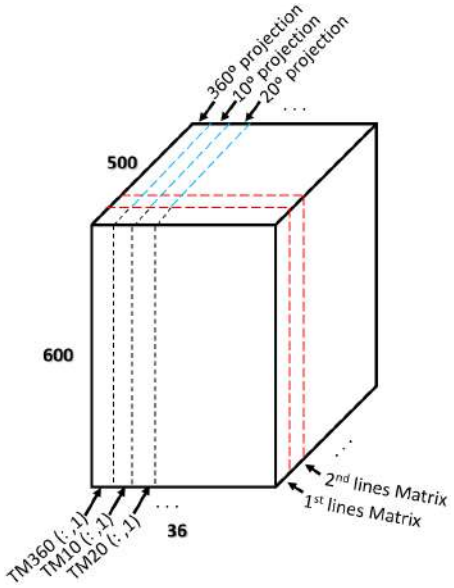

Figure 3.4: Schematic of the structure of matrices in which the data from each projection for each angle was loaded to. Note that this arrangement allows that the first line from each projection fits within a matrix of 600x36.

equation. Equivalently, this simplification was performed by applying the logarithm to the division of the `MATRIZ3D_AR` by the `MATRIZ3D` using the code listed in Appendix D.3.

Subsequently, the reconstruction was performed by assuming an approach of the cone-beam to the fan-beam. Therefore the MATLAB tool function `ifanbeam` was employed, which converts the fan-beam data to parallel beam projections and by using the filtered backprojection algorithm, performs the inverse Radon transform. This function allows the specification of several parameters that control various aspects of the reconstruction. One of the parameters is the interpolation method, that is involved in resampling, when transitioning from fan-beam to parallel-beam. The code used to perform this reconstruction, as well as the specification for each parameter are listed in Appendix D.4.

This resulted in a structure of matrices with dimensions 342x36x500. Given that the detector's height was 40 cm, corresponding to the upper and lower coordinates: z=150 and z=110, and that we obtained 500 slices, each slice is 0.08 cm apart from each other. Since the coordinates of the center position of each microcalcification in the breast and lung, in the z axis are:

$$\begin{cases} Breast : z = 130.65; \\ Lung : z = 131.70; \end{cases}$$

the axial slice containing each microcalcification can be determined by determining the distance from the bottom of the detector to the position of each microcalcification and

then dividing that distance by the distance between slices, and therefore:

$$\begin{cases} Breast : \frac{(130.65-110)}{0.08} = 258.13 \\ Lung : \frac{(131.70-110)}{0.08} = 146.25 \end{cases} \Leftrightarrow \begin{cases} Breast : \text{slice 258 or 259} \\ Lung : \text{slice 146 or 147} \end{cases}$$

By these means the axial slices to be acquired and analyzed, regarding each microcalcification in each organ were concluded to be:

$$\begin{cases} Breast : \text{slices } 257, 258, 259, 260 \\ Lung : \text{slices } 270, 271, 272, 273 \end{cases} \tag{3.4}$$

Using the code listed in Appendix D.4, these eight slices were acquired for each different implementation of the reconstruction algorithm, and saved for further image processing and analysis using the software program *ImageJ*. The implementation varied not only according to the interpolation method applied, which were *Linear* and *Cubic*, and to the filter applied, which were *Ram-Lak*, *Shepp-Logan*, *Cosine*, *Hamming* and *Hanning*, but also varied with the number of projections required for reconstruction, which was accomplished using 36 (10° increment), 18 (20° increment) and 12 projections (30° increment).

3.2.2 Image Quality Analysis

Calculations regarding the image quality were performed using the Equation 2.48 in Section 2.3.5.1 *Contrast-to-noise ratio*. In order to establish a ROI for each microcalcification, the simulations with no phantom, only containing both microcalcifications were used. The reconstruction algorithm using the *Linear* interpolation method and the *Ram-Lak* filter was applied to these simulations.

The reconstructed images regarding the previously mentioned slices 258 for the breast and 271 for the lung were acquired and then analyzed using the software program *ImageJ*, which is an image processing program designed for scientific multidimensional images. The ROI chosen for both slices regarding the object and the background region are shown in Figure 3.5.

Therefore the CNR was calculated for all eight slices, for all different implementations of the reconstruction algorithm.

3.2.3 Validation of the Reconstruction Algorithm

In order to validate the Reconstruction Algorithm that was developed, the same equipment used for the $CTDI_{100}$ experimental measurements, was employed, which is, the Varian TrueBeam linear accelerator operating ate the CCC in Lisbon. Figure 3.6 shows the experimental data acquisition apparatus employed.

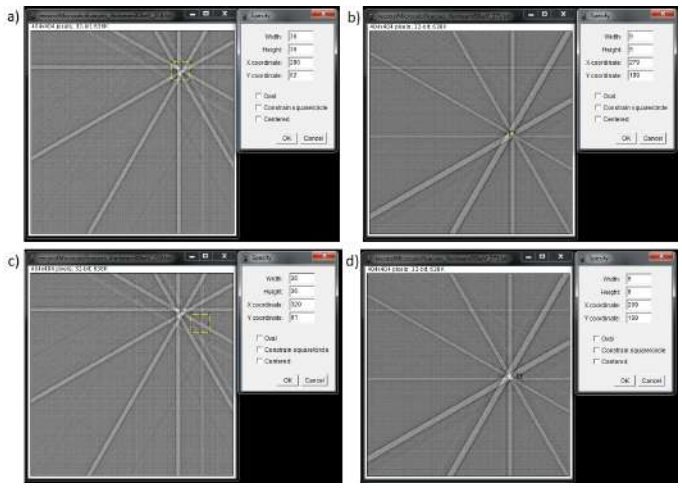

Figure 3.5: Visualization of the axial slices and the ROI's regarding not only the object, **a)** in the breast and **b)** in the lung, but also the background **c)** for the breast and **d)** for the lung.

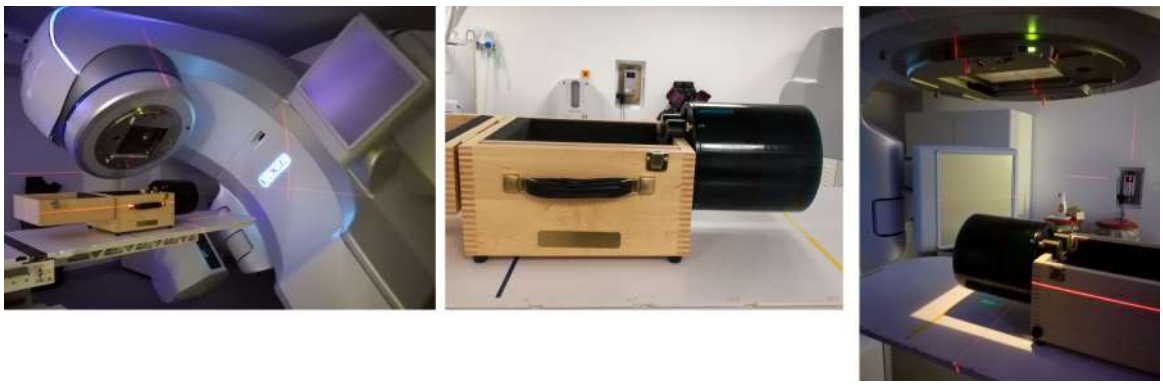

Figure 3.6: **Left:** Apparatus of the Varian TrueBeam linear accelerator and phantom employed for the experimental data acquisition; **Middle:** *Catphan 504* phantom; **Right:** Assembly and alignment of the *Catphan 504* on the linear accelerator.

The data was acquired using a specific phantom recommended by the manufacturer for image Quality Assurance: the *Catphan 504*. This phantom consists of several modules that cover all required CBCT imaging tests [64]. However, only the CTP528 high resolution module was relevant for this case, which is shown in Figure 3.7.

The protocol used for this acquisition was the Head Protocol, given that with the Thorax protocol the projection acquisition was made in a Half-Fan mode. With the Head Protocol a Full-Fan mode acquisition is employed, with the following characteristics: titanium filter, collimator blades set at $(X_1; X_2; Y_1; Y_2) = (-14.0; +14.0; -10.7; +10.7)$, 100 kV and 20 mA. The obtained files required a pre-processment to enable the access to the data matrix file which contains the image data. The MATLAB code function `ReadXim` [66], available on-line, was employed. The complete code system used to access the data and to transform the acquired files into a format adequate to be imported into the MATLAB workspace is listed and described in Appendix D.1. The code used for reconstructing the

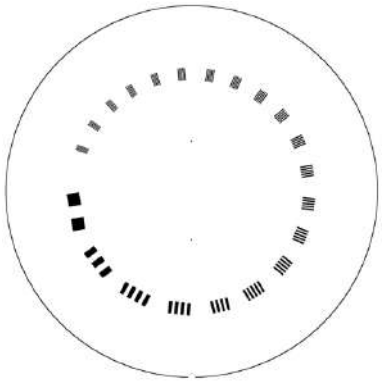

Figure 3.7: Illustration of an axial slice of the CTP528 module, which has a 1 to 21 line pair per centimeter high resolution test gauge [65].

images is listed in Appendixes E.2 and E.3. However, the Reconstruction Algorithm employed is the same as the one developed for reconstructing the images from the projections obtained from the simulations with the computational phantom. Additionally, a code was developed to access other content within the obtained files, and is listed and explained in Appendix E.4. This information was crucial given that for the reconstruction, two fundamental characteristics are needed: the distance from the beam source to the center of rotation in pixels, and the rotation angle increment. The information obtained regarding the collimator blades were $(X_1; X_2; Y_1; Y_2) = (-14.0023; +13.9999; -10.7009; +10.7008)$ and therefore the length of the detection area was determined to be 24.4 cm. Given that the dimension of the image data matrices were 768×1024, then the distance from the source to the center of rotation, that is 50 cm, corresponds to 2392.5 pixels. The information obtained regarding the rotation angle increment was of 0.406 degrees.

CHAPTER 4

RESULTS AND DISCUSSION

This chapter is divided into four sections. Section 4.1 *CBCT Model Validation* discusses and shows the results for validating the MC simulations regarding the CBCT model and the results regarding the validation of the reconstruction algorithm are presented. In the second section 4.2 *Acquired projections and reconstructed images* the obtained projections from the MC simulations are presented and discussed. In section 4.3 *Absorbed Dose Analysis*, two protocols are studied and analyzed regarding the absorbed dose in the breast and lungs. In the last section, *Image Quality Analysis*, the CNR values for different implementations of the reconstruction algorithm are presented as the number of projections differed within each one.

4.1 CBCT Model Validation

4.1.1 MC Simulations Validation

The experimental dose measurements acquired for calculating $CTDI_{100}$ are listed on Table 4.1. The uncertainty associated to the ionization chamber is 5%.

Table 4.1: Air kerma experimental measurements for $CTDI_{100}$.

Ionization Chamber Position	Air Kerma aquisition (mGy)			Average (mGy)
	1st	2nd	3rd	
Center	4.18500 ± 0.20925	3.97400 ± 0.19870	4.19300 ± 0.20965	4.11733 ± 0.20587
0°	5.88840 ± 0.29442	5.90467 ± 0.29523	5.84100 ± 0.29205	5.87802 ± 0,29390
90°	5.88700 ± 0.29435	6.00100 ± 0.30005	5.88700 ± 0.29435	5.92500 ± 0.29625
180°	4.61100 ± 0.23055	4.85500 ± 0.24275	4.62100 ± 0.23105	4.69567 ± 0.23478
270°	5.62200 ± 0.28110	5.54800 ± 0.27740	5.71400 ± 0.28570	5.62800 ± 0.28140

The experimental measurements for $CTDI_{100}$, as well as the measurements obtained and reported by Abuhaimed *et al* 2015 [43] are listed on Table 4.2. The $CTDI_{100}$ was

calculated according to the equation 3.3 and the $CTDI_W$ according to the equation 2.30.

Table 4.2: Experimental measurements and the measurements reported by Abuhaimed *et al* 2015 for $CTDI_{100}$ center, $CTDI_{100}$ average periphery and $CTDI_{100}$ weighted.

Abuhaimed *et al* 2015 $CTDI_{100}$		**Experimental measurements** $CTDI_{100}$	
125 kV, 264 mAs W = 198 mm	Adult Body Phantom (mGy)	125 kV, 270 mAs W = 214 mm	Adult Body Phantom (mGy)
Center	1.73	Center	1.73
Average Periphery	2.47	Average Periphery	2.33
Weighted	2.21	Weighted	2.13

The obtained measurements for the $CTDI_{100}$ are in agreement to the measurements reported by Abuhaimed *et al* 2015. These measurements are further compared to the values obtained from the simulations, as a validation for the MC simulations.

From the simulations of the $CTDI_{100}$ measurement using the PMMA phantom geometry model, the dose per particle (mGy/hist) was calculated for all probe holes regarding the irradiation angles 0° , 90° , 180° and 270° , using Equation 3.1, where the mass of the sensitive air chamber ($M_{sensChamber}$) is given by:

$$M_{sensChamber}(\text{kg}) = \left((\pi \times r^2 \times l) \times \rho\right) \times 0.001 \tag{4.1}$$

where $r = 0.15$ cm, $l = 10$ cm and $\rho = 1.20479 \times 10^{-3}$ (g.cm^{-3}).

Figure 4.1 illustrates the graph obtained after mathematical interpolation of the dose per particle as a function of the irradiated angle, relative to the center probe hole geometry. By these means the dose per particle was obtained regarding the other angles that weren't simulated.

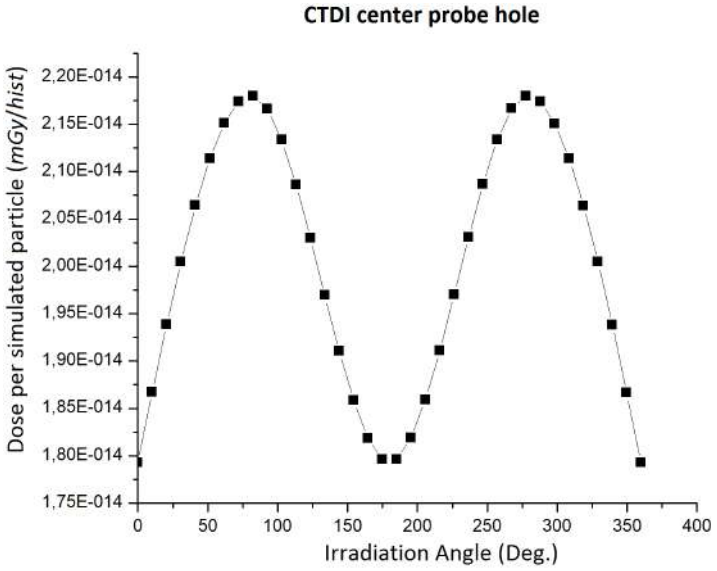

Figure 4.1: Graph of the dose per particle as a function of the irradiated angle for the center probe hole.

Dose values were obtained by normalizing the data to a number of particles. The number of particles were determined based on the method of Boone et al. [67] where by inserting the beam characteristics of 125 kV, 270 mAs, a tungsten anode, an inherent filter of 2.7 mm and a beam hardening filter of titanium with a thickness of 0.89 mm, we obtained the spectrum energy, and subsequently the number of particles that effectively reached the phantom (N_{SP}). Based on the following Equation 4.2 we determined the normalization factor ($Norm\ Factor$) for obtaining those same particles.

$$Norm\ Factor = \frac{N_{SP}}{A} \times AirKerma \tag{4.2}$$

N_{SP} is the number of particles, $A = 3.20 \times 10^7$ mm^2 is the FOV during a CBCT scan and $AirKerma$ is the experimental measurements of the $CTDI_{100}$.

Table 4.3: Air kerma experimental measurements and the values obtained from the simulations for the center, 0° and 90° probe hole.

Air Kerma				
125kV, 270mAs		Experimental Dose (mGy)	Simulated Dose (mGy)	Percent Error $(\frac{\lvert error \rvert}{E_{Dose}}) \times 100$
Probe hole	Center	4.12	4.2	1.94%
	0 degrees	5.88	6.88	17.01%
	90 degrees	5.93	6.80	14.67%

Table 4.3 lists the air kerma values from the simulated PMMA model and the values obtained experimentally for the center, 0° and 90° positions of the ionization chamber. It is important to refer that the simulated geometry was a simplified model of the apparatus for $CTDI_{100}$ measurements, as the simulated pencil ionization was a simplified geometry and the beam was simulated as a Full-Fan, with no filter, no collimator, among other devices that are found within a CBCT scanner.

By taking into consideration that the uncertainty associated to the ionization chamber is 5%, the uncertainty associated to the Siemens Tool used for obtaining the spectrum is 10% [68] [69] (corresponding to a total of 15%) and other approximations associated to the simplification of the simulated geometry, we concluded that the MC simulations were successfully validated.

4.1.2 Reconstruction Algorithm Validation

The reconstructed images of the CTP528 module of the *Catphan 504* phantom were obtained. Figure 4.2 illustrates the reconstructed axial slice number 234.

According to the Quality Assurance protocol for assessing image quality of the kV system incorporated into the linear accelerator employed in this project, six pairs of lines must be visible in the reconstructed axial slice of the CTP528 high resolution module. By observing the reconstructed axial image obtained using the developed algorithm (shown

Figure 4.2: Reconstructed axial slice of the CTP528 high resolution model of the *Catphan 504*, obtained by using the developed algorithm.

in Figure 4.2) we can visualize at least seven pair of lines, and therefore we concluded that the developed algorithm was successfully validated.

4.2 Acquired Projections and Reconstructed Images

The projections obtained as a result of the MC simulations using the monochromatic energy of 80 keV are shown in Figure 4.3, more specifically, the one's acquired at 0° and 180° , corresponding to Postero-Anterior (PA) and Antero-Posterior (AP) geometries, respectively.

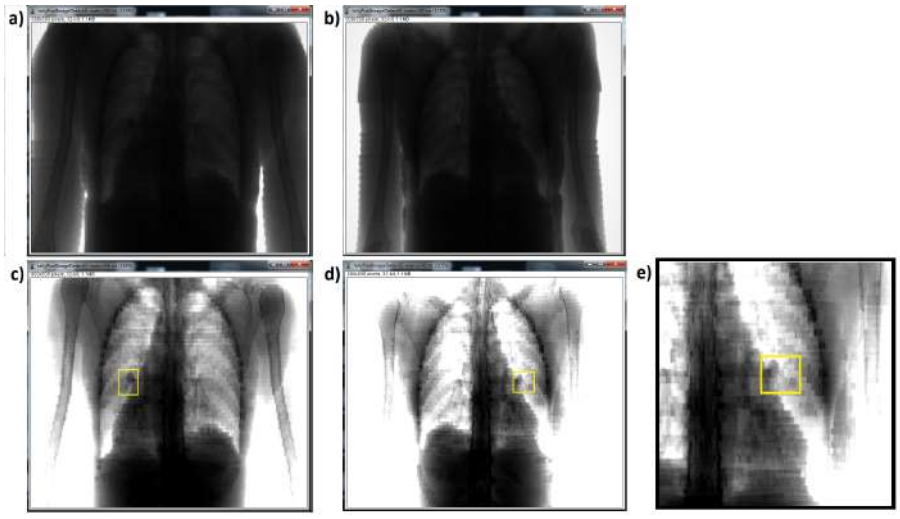

Figure 4.3: Visualization of the projections acquired using 80 keV energy, at 0° shown in **a)** (corresponding to a PA geometry) and 180° shown in **b)** (corresponding to an AP geometry). The brightness and contrast were altered in **c)** and **d)** for microcalcification visualization, which correspond to 0° and 180° respectively. In **e)** a closeup of both breast and lung microcalcifications obtained from **d)** is shown.

In Figure 4.4 the projections obtained for the same angles as previously mentioned,

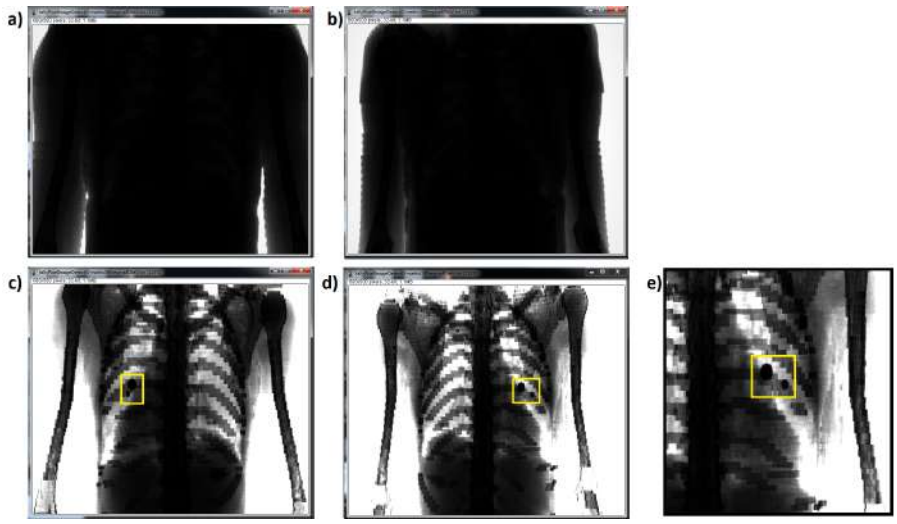

Figure 4.4: Visualization of the projections acquired using 30 keV energy, at 0° shown in **a)** (corresponding to a PA geometry) and 180° shown in **b)** (corresponding to an AP geometry). The brightness and contrast were altered in **c)** and **d)** for microcalcification visualization, which correspond to 0° and 180° respectively. In **e)** a closeup of both breast and lung microcalcifications obtained from **d)** is shown.

however using the monochromatic energy of 30 keV, are shown with emphasis to the visualization of both microcalcifications.

The projections for both energies were obtained with relative uncertainties of 1%, which is a criteria inserted into the configuration file used for stopping the simulations.

In figure 4.5 a reconstructed image obtained using 36 projections, obtained with the 80 keV beam energy and using the linear interpolation method and the *Ram-Lak* filter is shown, alongside a slice obtained directly from the adult female reference computational phantom using the *Gnuplot* tool. The reconstructed slice appears to have some

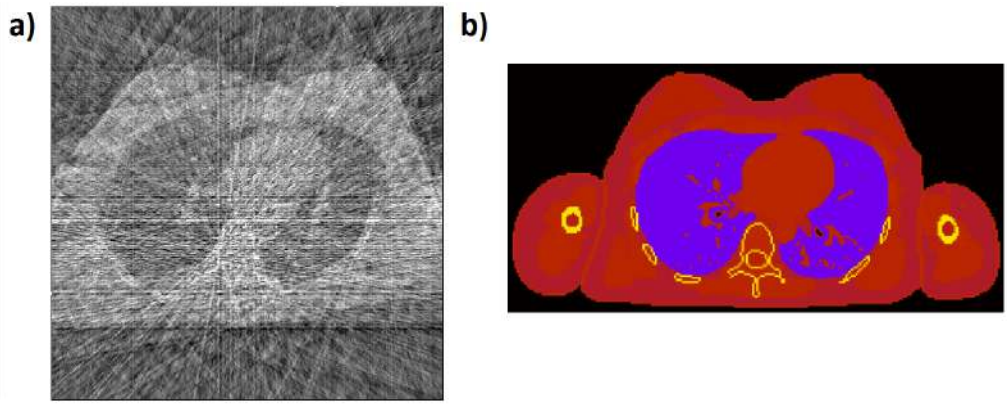

Figure 4.5: Visualization a reconstructed axial obtained with 80 keV energy beam, using linear interpolation and *Ram-Lak* filter in **a)** and **b)** is an axial image obtained directly from the computational phantom using the *Gnuplot* tool.

reconstruction artifacts, nevertheless this reconstruction was accomplished using only 36 projections (corresponding to a 10° angle increment between acquisitions) and even so,

some main organ structures can be distinguished: as the lungs, the heart, the breasts and the spine.

As for the projections acquired with 30 keV, using the same reconstruction algorithm as the one used with the 80 keV projections and the same number of projections, these yielded reconstructed images that were merely composed by reconstruction artifacts, as shown in Figure 4.6.

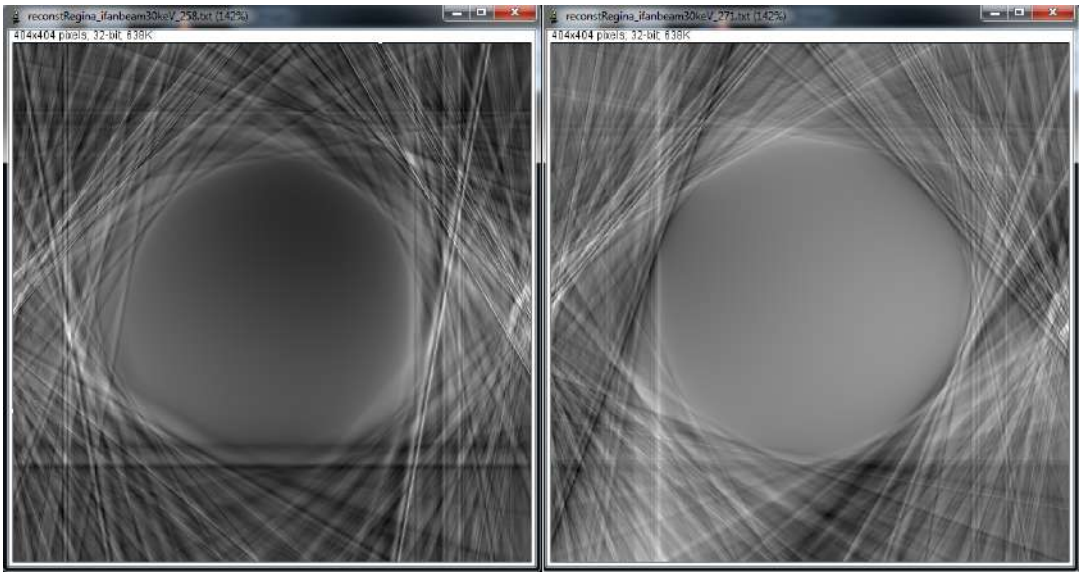

Figure 4.6: Visualization of the reconstructed images yielded using the 30 keV projections. **Left:** reconstructed axial slice number 258, corresponding to the breast's microcalcification slice. **Right:** reconstructed axial slice number 271, corresponding to the lung's microcalcification slice.

These results suggest that a tube voltage of 30 keV wasn't sufficiently energetic to yield reconstructed images when using only 36 projections, this is, when using a 10° angle increment between acquisitions.

4.3 Absorbed Dose Analysis

The Energy Deposition file for each simulated projection with the 80 keV energy, was analyzed in terms of the energy deposited within both organs (breast and lung). This data was converted into absorbed dose per simulated particle by applying equation 3.1. The Tissue Mass values for both organs were:

$$\begin{cases} Breast : 9.50010 \times 10^{-1}\ \text{kg} \\ Lung : 2.00000 \times 10^{-1}\ \text{kg} \end{cases}$$

For the breast, only the glandular tissue was taken into account.

The Dose was calculated for two distinct protocols. One with a normalization factor of 2 mGy in the breast, given that, in average this is the dose received by the patient when submitted to a mammography scan, regarding one view (craniocaudal or mediolateral).

The other one was established to a dose of 5 mGy in the lung, given that that is typically the dose received by a patient submitted to a LDCT scan. In both protocols, these doses were considered to be obtained with 36 projections, nevertheless, Figure 4.7 illustrates two graphs, showing the dose values in the breast and lung for each distinct protocol, when the number of projections used for images acquisition differed.

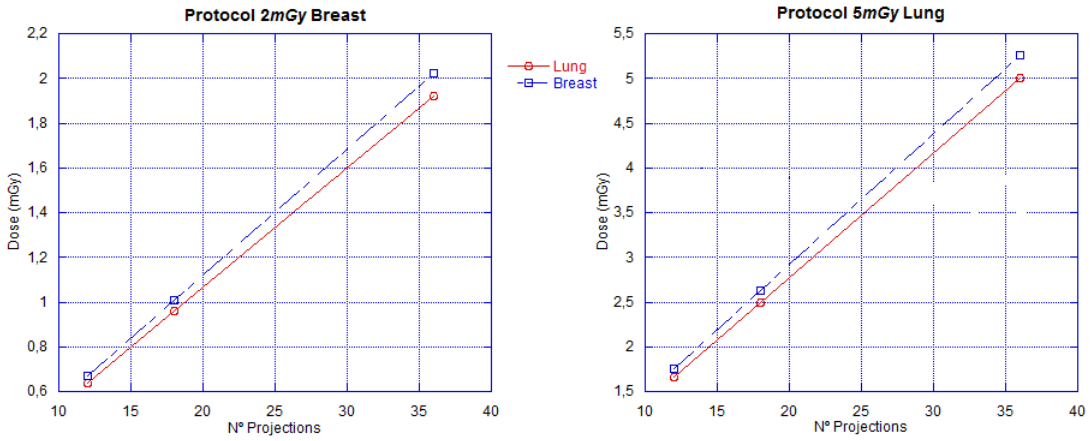

Figure 4.7: Graphs of the Dose values in both organs, for both protocols, when the number of projections required for image acquisition differs. **Left:** Graph using the protocol that establishes a 2 mGy dose in the breast, when using 36 projections; **Right:** Graph using the protocol that establishes a 5 mGy dose in the lung, when using 36 projections.

With both protocols, there is a linear increase of the dose within both organs, as the number of projections increases. When the number of projections varies from 12 to 36, there is a dose increase of a factor of 3.

Namely, for each chosen protocol (breast or lung), MC simulations showed that the absorbed dose in the two target organs are very similar. This issue is mainly due to the fact that the energy deposited in the breast (denser tissue) is greater than the one deposited in the lung. However, when considering the absorbed dose, the masses of the two organs introduce a compensation factor between the two dose values. Also, this trend could simplify the best protocol strategy to follow for this type of examination, since for each protocol the absorbed dose would be similar.

4.4 Image Quality Analysis

The reconstructed images obtained from all different implementations of the reconstruction algorithm, of the projections acquired with the 80 keV beam energy are listed in Tables 4.4, where the interpolation method applied was Linear and 4.5, where the interpolation method applied was Cubic. Only the slices number 258 and 271 relative to the microcalcifications in the breast and lung are shown in both Tables.

By visually analyzing the reconstructed slices with 12 projections we concluded that these images aren't viable as they contain a fair amount of artifacts due to the small amount of projections used for the reconstruction. However these reconstructions were

Table 4.4: Reconstructed axial slices number 258 and 271 regarding the breast and lung are shown, using Linear Interpolation and varying the type of filter applied as well as in the number of projections used for the reconstruction.

Linear Interpolation

	Number of projections					
	36		18		12	
	Breast slice 258	Lung slice 271	Breast slice 258	Lung slice 271	Breast slice 258	Lung slice 271
Ram-Lak	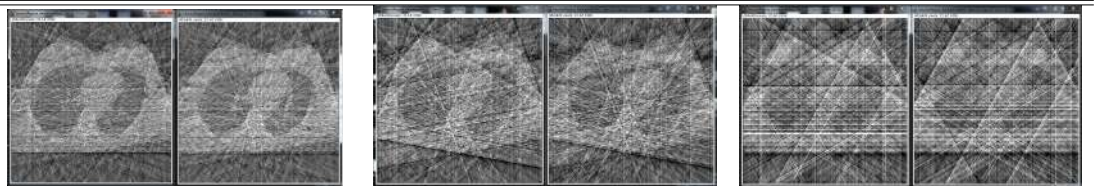					
Shepp-Logan	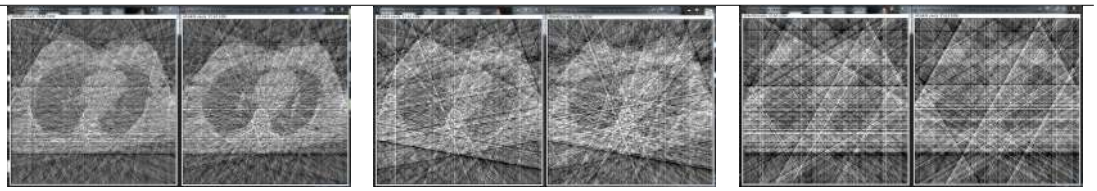					
Cosine	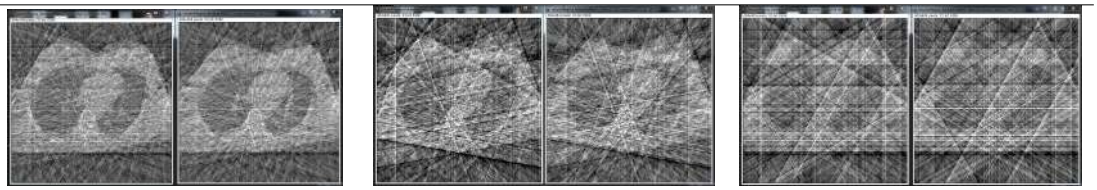					
Hamming	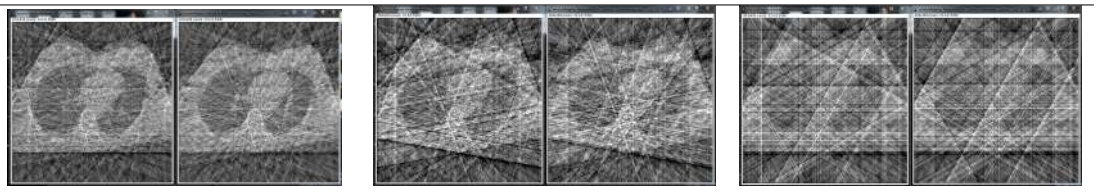					
Hanning	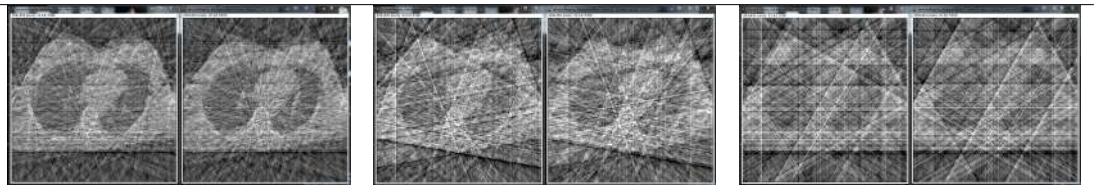					

Table 4.5: Reconstructed axial slices number 258 and 271 regarding the breast and lung are shown, using Cubic Interpolation and differing in the filter applied as well as in the number of projections used for the reconstruction.

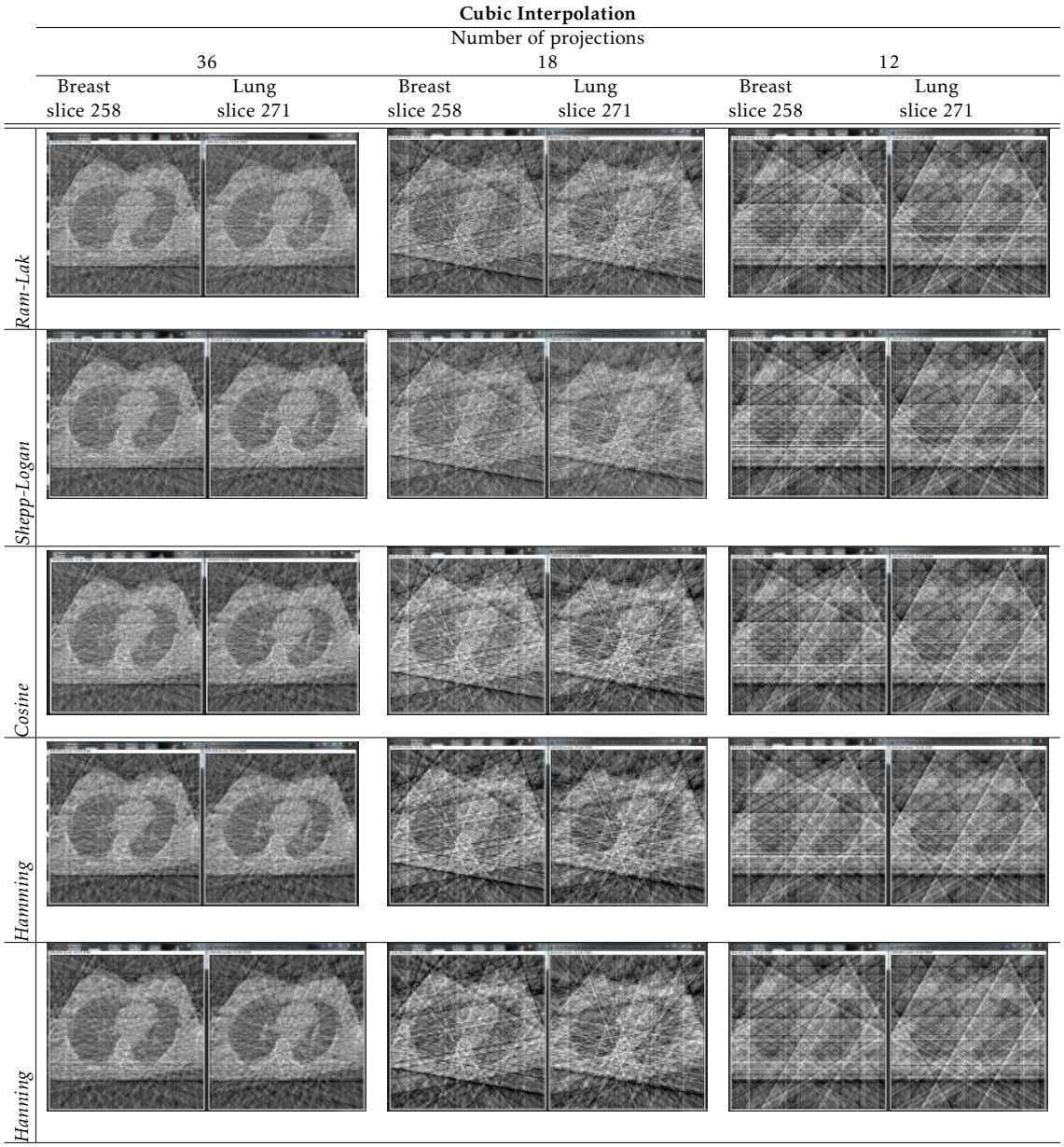

taken into consideration when studying the CNR for all eight slices as described in the equation system 3.4, in order to study the graph trend of the CNR when the number of projections for the reconstruction increased.

In order to study this trend, the CNR of all four axial slices, regarding each microcalcification site, were determined and an average of all four was calculated. By these means an average value for the CNR for each different implementation of the reconstruction algorithm, regarding both microcalcification sites, was determined. Therefore, Figure 4.8 shows the graphs obtained for the slices regarding the breast microcalcification, as for the graphs regarding the lung microcalcification, they are shown in Figure 4.9.

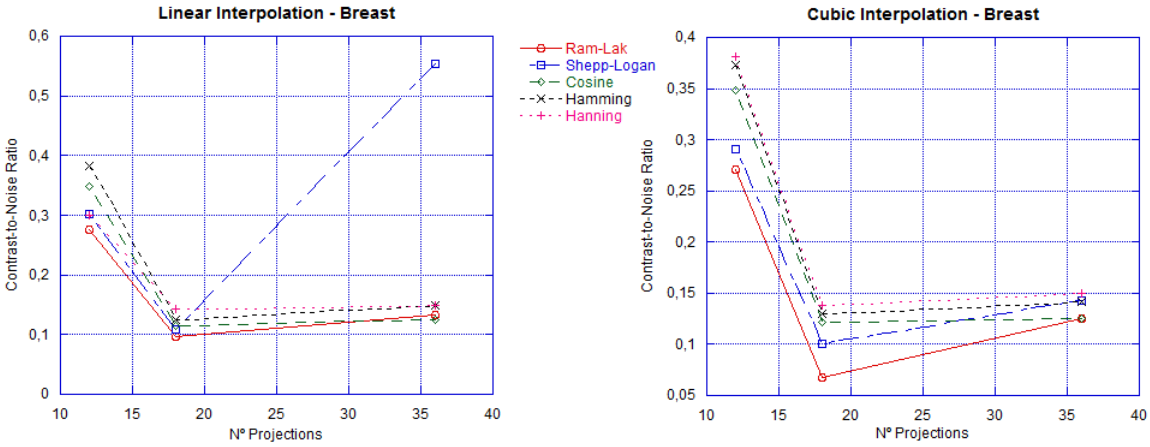

Figure 4.8: Graphs of the CNR, for different implementations of the reconstruction algorithm regarding the breast microcalcification site. **Left:** Applying the linear interpolation method; **Right:** Applying the cubic interpolation method.

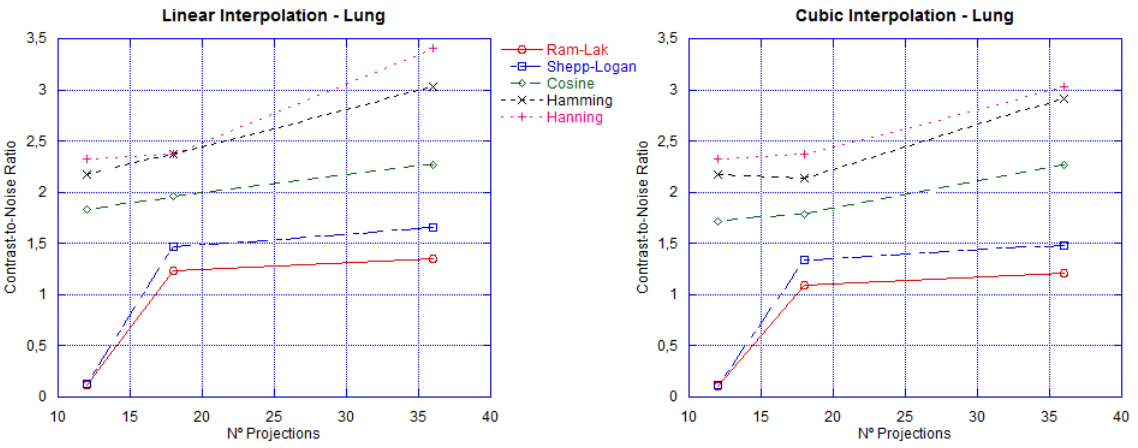

Figure 4.9: Graphs of the CNR, for different implementations of the reconstruction algorithm regarding the lung microcalcification site. **Left:** Applying the linear interpolation method; **Right:** Applying the cubic interpolation method.

Both graphs show the variation of the CNR for different implementations of the algorithm, as the number of projections increases. On both Figures, the graphs on the left

correspond to a linear interpolation, as for the one's on the right, they correspond to a cubic interpolation.

Regarding the microcalcification in the breast (Figure 4.8), in both graphs there is a significant increase of the CNR when using 12 projections, indicating that this collected data refers to artifacts and noise. This strongly suggest that the breast lesion of 4*mm* isn't detectable with any of the implementations of the reconstruction algorithm.

In the graphs regarding the microcalcification in the lung, there is a trend for an increase in the CNR as the number of projections increases and therefore as the increment angle decreases between projections. Also, in both graphs, the best implementations of the reconstruction algorithm was achieved using the *Hanning* filter. However, there is a slight improvement with this filter when the interpolation method is linear and using 36 projections. Therefore, these results indicate that the best implementation of the reconstruction algorithm was achieved with linear interpolation and *Hanning* filter.

Overall, based on the absolute values of the CNR for the lung and for the breast (for both linear and cubic interpolation), the lung presents higher values when compared to the breast, suggesting that it may be beneficial in opting for the lung protocol (for absorbed dose in the organs of interest), for a better lesion visualization.

Chapter 5

Conclusions and Future Work

This project emerged in attempt to respond to the nonexistence of a technique which allows medical imaging acquisitions, simultaneously of the breast and lung. Therefore, the feasibility of employing a CBCT scanner to fulfill this gap, by performing a modulated beam scan acquisition of both organs, was studied.

Two main milestones were established: MC simulations of a CBCT model for two distinct tube voltage protocols, and reconstruction algorithm development, for reconstructed image acquisition and analysis.

First of all, using the PENELOPE code system, the implemented MC model of a CBCT image acquisition system was successfully validated, with a maximum discrepancy of about 17% between the experimentally measured values and the simulated values for the $CTDI_{100}$. This relatively high discrepancy is due to approximations associated to the simplification of the geometrical model employed, of a CBCT scanner, and to the inherent uncertainties associated to the equipment and tools employed in the process.

Additionally, an algorithm for accessing and preprocessing files from the kV imaging system, used for CBCT scans, incorporated into a Varian TrueBeam linear accelerator was developed.

Based on the QA protocol for assessing image quality of the kV system of the linear accelerator employed, the developed reconstruction algorithm was also considered successfully validated, using the CTP528 high resolution module of the *Catphan 504*.

For the first milestone, the ICRP adult female reference computational phantom was used for projection acquisition and dose analysis. Additionally, two microcalcifications, with radius of 0,4 cm and 0,7 cm were inserted into the breast and lung respectively and these simulations were performed for two distinct tube voltages of 30 keV and 80 keV. In the acquired simulated projections for both tube energies, the microcalcifications were distinguishable and the two target organs were perceptible.

The absorbed dose in both organs (breast and lungs) were determined according to two protocols: one with a normalization factor of 2 mGy in the breast and another with a normalization factor of 5 mGy in the lungs, when performing a 10° angle increment between acquisitions.

The values show that for both protocols, the absorbed dose in the two organs of interest is the same. When determining the absorbed dose, the masses for each organ introduces a compensation factor between the two dose values. This trend assists in determining the best protocol strategy to follow, given that for each protocol the absorbed dose would be the same.

Several implementations of the developed reconstruction algorithm were employed for the reconstruction. These differed not only in the filter and in the interpolation method applied, but also in the acquisition angle increment. The reconstructed images yielded from the 30 keV projections, were merely composed by reconstruction artifacts. This suggests that a tube voltage of 30 keV isn't sufficiently energetic to yield reconstructed images of the thorax, when using a 10° acquisition angle increment, this is, when using 36 projections.

The reconstructed images yielded from the 80 keV projections, for all implementations of the reconstruction algorithm, were analyzed in terms of the CNR by determining a ROI for each microcalcification site.

The results regarding the microcalcification in the breast show that there is an increase of the CNR when using 12 projections, indicating that this collected data refers to artifacts and noise. This strongly suggests that the 4 mm breast lesion wasn't detectable with any of the implementations of the reconstruction algorithm.

The results regarding the microcalcification in the lung show an increase in the CNR, as the number of projections increases, and therefore, as the increment angle decreases. Results also indicate that the best implementation of the reconstruction algorithm was achieved with linear interpolation and *Hanning* filter

In general, based on the absolute values of the CNR, the lung presents higher values when compared to the breast. This suggests that it may be beneficial in opting for the lung protocol (for absorbed dose in the organs of interest), for a better lesion visualization.

This methodology ensures dose reduction, not only due to the fact that CBCT scans require only one (full or half-fan) rotation to acquire data of the FOV, but also when comparing to other medical imaging methods, that require two exams to obtain images of both organs, breast and lung (mammography/DBT and LDCT). Also, the data obtained with the $80keV$ tube voltage energy suggests promising results in the application of a CBCT system for simultaneous breast and lung image acquisition and the possibility of developing a CBCT modulated beam scanner.

Nevertheless, there are some perspectives of possible improvements and future work that mainly focus on the following aspects:

- Study and analyze reconstructed images using other values for the angle increment

between acquisitions, for instance 5° ;

- Study and determine the optimal tube voltage, by simulating energies of 40 and 50 keV, as a means of employing a CBCT modulated beam scanner for simultaneous breast and lung imaging;
- While this study focused on the detection and visualization of microcalcifications, other lesion should be studied, for instance tumor tissue and different lesion sizes;
- In the development of the reconstruction algorithm, an approach from Cone-beam to Fan-beam was considered, and therefore an improved reconstruction algorithm that better adjusts to the Cone-shape beam, based on Feldkamp-Daviss-Kress algorithm, should be developed.

Overall, the goals accomplished throughout this work provide a further step not only into the possibility of applying CBCT-based systems for assisting physicians with better medical information, and therefore increase the chances of early cancer detection, but also in reducing the dose administrated in medical exams when acquiring medical images of two distinct organs and in providing a possible solution for the nonexistence of a technique which allows simultaneous medical imaging, of the breast and lungs.

References

[1] World Health Organization, *Cancer*, 2018. [Online]. Available: http://www.who.int/mediacentre/factsheets/fs297/en/ (visited on 07/03/2017).

[2] International Agency for Research on Cancer, *Globocan 2012: Estimated Cancer Incidence, Mortality and Prevalence Worldwide in 2012*. [Online]. Available: http://globocan.iarc.fr/Pages/fact{_}sheets{_}cancer.aspx (visited on 07/04/2017).

[3] American Cancer Society, *Global Cancer Facts & Figures*, 3rd ed., American Cancer Society, Ed. Atlanta, 2015.

[4] B. W. Stewart and C. P. Wild, "World cancer report 2014," *World Health Organization*, 2014, ISSN: 0732-183X. DOI: 9283204298. arXiv: 1011.1669. [Online]. Available: http://www.videnza.org/wp-content/uploads/World-Cancer-Report-2014.pdf.

[5] N. Miranda, C. Portugal, P. J. Nogueira, C. S. Farinha, A. Soares, and M. I. Alves, *PORTUGAL Doenças Oncológicas em números – 2014*. 2014, ISBN: 2183-0746.

[6] National Comprehensive Cancer Network, "Lung Cancer Screening," National Comprehensive Cancer Network, Tech. Rep. 1.2018, 2017.

[7] D. Frank C., M. Peter J., N. David P., and B. Peter B., "Screeningfor Lung Cancer," *CHEST*, vol. DIAGNOSIS, e72S –e92S, 2013. DOI: 10.1378/chest.12-2350.

[8] BREASTCANCER.ORG, *Digital Tomosynthesis*, 2016. [Online]. Available: http://www.breastcancer.org/symptoms/testing/types/dig{_}tomosynth (visited on 06/04/2017).

[9] S Zackrisson, F Cardoso, and E. Guidelines, "clinical practice guidelines Primary breast cancer : ESMO Clinical Practice Guidelines for diagnosis , treatment and follow-up," *Annals of Oncology*, vol. 26, no. Supplement 5, pp. v8–v30, 2015. DOI: 10.1093/annonc/mdv298.

[10] National Cancer Institute, *Cancer Screening Overview - Patient Version*, 2017. [Online]. Available: https://www.cancer.gov/about-cancer/screening/patient-screening-overview-pdq (visited on 06/04/2017).

[11] J Jin, "Breast cancer screening guidelines in the united states," *JAMA*, vol. 314, no. 15, p. 1658, 2015, ISSN: 0098-7484. DOI: 10.1001/jama.2015.11766. [Online]. Available: http://dx.doi.org/10.1001/jama.2015.11766.

[12] National Comprehensive Cancer Network, "Breast Cancer Screening and Diagnosis," National Comprehensive Cancer Network, Tech. Rep. 1.2017, 2017.

[13] K. C. Oeffinger, E. T. H. Fontham, R. Etzioni, A. Herzig, J. S. Michaelson, Y.-c. T. Shih, L. C. Walter, T. R. Church, J. Lortet-tieulent, K. Andrews, D. Manassaram-baptiste, and D. Saslow, "Breast Cancer Screening for Women at Average Risk 2015 Guideline Update From the American Cancer Society," *Clinical Review & Education*, vol. 314, no. 15, pp. 1599–1614, 2016. DOI: 10.1001/jama.2015.12783.

[14] H. Gervásio, S. Braga, P. Pimentel, C. de Oliveira, J. L. P. Coelho, M. J. Cardoso, M. J. Cardoso, and S. Braga, *Recomendações nacionais para diagnóstico e tratamento do cancro da mama*, 9th ed., M. J. Cardoso and S. Braga, Eds. 2012. [Online]. Available: https://www.dgs.pt/documentos-e-publicacoes/recomendacoes-nacionais-para-diagnostico-e-tratamento-do-cancro-da-mama-pdf.aspx.

[15] S. S. J. Feng and I. Sechopoulos, "Clinical Digital Breast Tomosynthesis System : Dosimetric Characterization," *Radiology*, vol. 263, no. 1, pp. 35–42, 2012. DOI: 10.1148/radiol.11111789.

[16] R. A. Smith, D. Saslow, K. A. Sawyer, W. Burke, P. E. Iii, M. Work, and R. S. Foster, "American Cancer Society Guidelines for Breast Cancer Screening : Update 2003," *CA: A Cancer Journal for Clinicians*, vol. 53, no. 3, pp. 141–169, 2003.

[17] M Alakhras, R Bourne, M Rickard, K. H. Ng, M Pietrzyk, and P. C. Brennan, "Digital tomosynthesis : A new future for breast imaging?" *Clinical Radiology*, vol. 68, e225–e236, 2013. DOI: 10.1016/j.crad.2013.01.007. [Online]. Available: http://dx.doi.org/10.1016/j.crad.2013.01.007.

[18] The National Lung Screening Trial Research Team, "Reduced Lung-Cancer Mortality with Low-Dose Computed Tomographic Screening," *The New England Journal of Medicine*, vol. 365, no. 5, pp. 395–409, 2011. DOI: 10.1056/NEJMoa1102873.

[19] P. B. Bach, J. N. Mirkin, T. K. Oliver, C. G. Azzoli, D. A. Berry, O. W. Brawley, T. Byers, G. A. Colditz, M. K. Gould, J. R. Jett, A. L. Sabichi, R. Smith-bindman, and D. E. Wood, "Benefits and Harms of CT Screening for Lung Cancer A Systematic Review," *Clinician's Corner*, vol. 307, no. 22, 2012. DOI: 10.1001/jama.2012.5521.

[20] National Lung Screening Trial Research Team, "The National Lung Screening Trial: Overview and Study Design," *Radiology*, vol. 258, no. 1, 2011. DOI: 10.1148/radiol.10091808/-/DC1.

[21] N. Clinical, P. Guidelines, and N. Guidelines, "Non-Small Cell Lung Cancer," National Comprehensive Cancer Network, Tech. Rep. 8.2017, 2017. [Online]. Available: www.nccn.org/patients.

[22] AAPM Task Group 23: CT Dosimetry, *The Measurement, Reporting, and Management of Radiation Dose in CT*, 96. American Association of Physicists in Medicine, 2008, ISBN: 978-1-888340-73-0.

[23] A. O'Connell, D. L. Conover, Y. Zhang, P. Seifert, W. Logan-Young, C. F. L. Lin, L. Sahler, and R. Ning, "Cone-beam CT for breast imaging: Radiation dose, breast coverage, and image quality," *American Journal of Roentgenology*, vol. 195, no. 2, pp. 496–509, 2010, ISSN: 15463141. DOI: 10.2214/AJR.08.1017.

[24] N. J. Packard, C. K. Abbey, K. Yang, and J. M. Boone, "Effect of slice thickness on detectability in breast CT using a prewhitened matched filter and simulated mass lesions," *Medical Physics*, vol. 39, no. 4, pp. 1818–1830, 2012, ISSN: 00942405. DOI: 10.1118/1.3692176.

[25] W. A. Kalender, M. Beister, J. M. Boone, D. Kolditz, S. V. Vollmar, and M. C. C. Weigel, "High-resolution spiral CT of the breast at very low dose: concept and feasibility considerations," *European Radiology*, vol. 22, no. 1, pp. 1–8, 2012, ISSN: 09387994. DOI: 10.1007/s00330-011-2169-4.

[26] ICRP, "ICRP Publication 129: Radiological Protection in Cone Beam Computed Tomography (CBCT)," *Annals of the ICRP*, 2015, ISSN: 17962021. DOI: 10.4304/jcm.5.2.89-91.

[27] J. T. Bushberg, J. A. Seibert, E. M. Leidholdt Jr, and J. M. Boone, *The Essential Physics of Medical Imaging*, Third Edit, C. W. Mitchell, Ed. Philadelphia, Pennsylvania USA: Lippincott Williams & Wilkins, 2002, ISBN: 978-0-7817-8057-5.

[28] D. S. MacDonald-Jankowski and E. C. Orpe, "Computed tomography for oral and maxillofacial surgeons. Part 2: Cone-beam computed tomography," *Asian Journal of Oral and Maxillofacial Surgery*, vol. 18, no. 2, pp. 85–92, 2006, ISSN: 09156992. DOI: 10.1016/S0915-6992(06)80001-4. [Online]. Available: http://dx.doi.org/10.1016/S0915-6992(06)80001-4.

[29] W. C. Scarfe, a. G. Farman, and P Sukovic, "Clinical applications of cone-beam computed tomography in dental practice," *J Can Dent Assoc*, vol. 72, no. 1, pp. 75–80, 2006, ISSN: 1488-2159. DOI: 10.1016/j.tripleo.2005.07.027.

[30] IAEA, *Radiation Oncology Physics: A Handbook for Teachers and Students*, E. B. Podgorsak, Ed. Austria: International Atomic Energy Agency, 2005.

[31] R. Cierniak, *X-Ray Computed Tomography in Biomedical Engineering*. New York: Springer, 2011.

[32] E. B. Podgorsak, *Radiation Physics for Medical Physicists*, Second Edi, E. Greenbaum, Ed. Tennessee, USA: Springer, 2004, ISBN: 978-3-642-00874-0. DOI: 10.1007/978-3-642-008745-7.

[33] K. S. Krane, *Introductory Nuclear Physics*. USA: John Wiley & Sons, Inc, 1988, ISBN: 0-471-80553-X.

[34] P. Suetens, *Fundamentals of Medical Imaging*, Second Edi. New York: Cambridge University Press, 2009, ISBN: 978-0-511-59640-7.

[35] B. H. Bransden and C. J. Joachain, *Physics of atoms and molecules*. New York: Longman Scientific & Technical, 1983, ISBN: 0582444012.

[36] ICRU, "ICRU report No 85: Fundamental Quantities And Units For Ionizing Radiation (Revised)," International Commission on Radiation Units and Measurements, Tech. Rep. 1, 2011, pp. 1–35. DOI: 10.1093/jicru/ndr012.

[37] IAEA, *Diagnostic Radiology Physics: A Handbook for Teachers and Students*, D. Dance, S. Christofides, A. Maidment, I. McLean, and K. Ng, Eds. Austria: International Atomic Energy Agency, 2014, ISBN: 978-92-0-131010-1.

[38] N. B. Smith and A. Webb, *Introduction to Medical Imaging: Physics, Engineering and Clinical Applications*, W. Saltzman and S. Chien, Eds. New York: Cambridge University Press, 2011, p. 286, ISBN: 978-0-521-19065-7. DOI: 10.1017/CBO9781107415324.004. arXiv: arXiv:1011.1669v3.

[39] J. E. Turner, *Atoms, Radiation, and Radiation Protection*, Third Edit. Weinheim, Germany: Wiley-VCH Verlag GmbH & Co. KGaA, 2007, ISBN: 9783527406067.

[40] E. L. Alpen, *Radiation Biophysics*, Second Edi. California USA: Academic Press, 1990, ISBN: 0120530856.

[41] ICRP, "ICRP Publication 116: Conversion Coefficients for Radiological Protection Quantities for External Radiation Exposures," *Annals of the ICRP*, vol. 40, 2010, ISSN: 01466453. DOI: 10.1016/j.icrp.2011.10.001.

[42] IEC, "Particular Requirements for the safety of x-ray equipment for computed tomography," International Electrotechnical Commission, Tech. Rep., 2001.

[43] A. Abuhaimed, C. J. Martin, M. Sankaralingam, and D. J. Gentle, "A Monte Carlo investigation of cumulative dose measurements for cone beam computed tomography (CBCT) dosimetry.," *Physics in medicine and biology*, vol. 60, no. 4, pp. 1519–42, 2015, ISSN: 1361-6560. DOI: 10.1088/0031-9155/60/4/1519.

[44] X. G. Xu, "An exponential growth of computational phantom research in radiation protection, imaging, and radiotherapy: A review of the fifty-year history," *Physics in Medicine and Biology*, vol. 59, no. 18, 2014, ISSN: 13616560. DOI: 10.1088/0031-9155/59/18/R233. arXiv: NIHMS150003.

[45] J. Hendricks, G. McKinney, J. Durkee, M. James, D. Pelowitz, H. Trellue, and F. Gallmeier, *The MCNPX radiation transport code. M and C 2005: international topical meeting on mathematics and computation, supercomputing, reactor physics and nuclear and biological applications*, France, 2005.

[46] I. Kawrakow, D. Rogers, F. Tessier, and B. Walters, "The EGSnrc code system: Monte Carlo simulation of electron and photon transport," *PIRS Report No. 701 NRCC*, 2018.

[47] H. Iwase, K. Niita, and T. Nakamura, "Development of General-Purpose Particle and Heavy Ion Transport Monte Carlo Code," *Journal of Nuclear Science and Technology*, vol. 39, no. 11, pp. 1142–1151, 2002, ISSN: 00223131. DOI: 10.1080/18811248.2002.9715305.

[48] F. Salvat, J. M. Fernández-Varea, and J. Sempau, *PENELOPE – A Code System for Monte Carlo Simulation of Electron and Photon Transport*. Barcelona, Spain: OECD NEA, 2003, ISBN: ISBN 92-64-02145-0.

[49] F. Salvat, "PENELOPE-2014: A Code System for Monte Carlo Simulation of Electron and Photon Transport," vol. 3, no. July, 2015.

[50] J. Sempau, A. Badal, and L. Brualla, "A PENELOPE-based system for the automated Monte Carlo simulation of clinacs and voxelized geometries-application to far-from-axis fields," *Medical Physics*, vol. 38, no. 11, pp. 5887–5895, 2011, ISSN: 00942405. DOI: 10.1118/1.3643029.

[51] "Basic Anatomical and Physiological Data for Use in Radiological Protection Reference Values," *ICRP Publication 89*, vol. Ann. No. ICRP 32, 2002.

[52] "The 2007 Recommendations of the International Commission on Radiological Protection," *ICRP Publication 103*, vol. Ann. No. ICRP 37, 2007.

[53] "Adult Reference Computational Phantoms," *ICRP Publication 110*, vol. Ann. 2009.

[54] Prof. Dr. Philippe Cattin, *Computed Tomography - Biomedical Image Analysis*, 2017. [Online]. Available: https://cian.unibas.ch/BIA/08-ComputedTomography-media/figs/image{_}reconstruction.png (visited on 03/07/2018).

[55] Z. Wu, K. Gao, Z. Wang, X. Ge, J. Chen, D. Wang, Z. Pan, K. Zhang, P. Zhu, and Z. Wu, "A new method to retrieve phase information for equiangular fan beam differential phase contrast computed tomography," *Medical Physics*, vol. 40, no. 3, pp. 1–8, 2013, ISSN: 00942405. DOI: 10.1118/1.4791672.

[56] Wikipedia - The free Encyclopedia, *Tomographic reconstruction*. [Online]. Available: https://en.wikipedia.org/wiki/Tomographic{_}reconstruction (visited on 03/10/2018).

[57] T. M. Buzug, *Computed Tomography From Photon Statistics to Modern Cone-Beam CT*. Springer, 2008, ISBN: 978-3-540-39407-5. DOI: 10.1007/978-3-540-39408-2Library.

[58] Students enrolled in MDSC 689.01 at The University of Calgary in Fall Terms over 2013-15, *Image Reconstruction (CT)*. [Online]. Available: http://199.116.233.101/index.php/Image{_}Reconstruction{_}(CT) (visited on 03/13/2018).

[59] R. C. Gonzalez, R. E. Woods, A. H. Scott, and P. P. Hall, *Digital Image Processing*, M. J. Horton, M. McDonald, A. Dworkin, W. Opaluch, S. Disanno, and R. Kernan, Eds. Pearson Prentice Hall, 2008, ISBN: 9780131687288.

[60] A. C. Kak and S. M., *Principles of Computerized Tomographic Imaging*. New York: IEEE Press, 1988.

[61] Y. Haider, M. Arif, N. Rahman, and M. Haseeb, "A prototype system for infrared computed tomography for image reconstruction," *2009 IEEE 13th International Multitopic Conference*, pp. 1–5, 2009. DOI: 10.1109/INMIC.2009.5383105.

[62] J. C. Borbinha, "Organ Dose Estimates in Thorax CT: Voxel Phantom Organ Matching With Individual Patient Anatomy," Master's thesis, Faculty of Sciences and Technology, NOVA University of Lisbon, 2017.

[63] J. Sempau, *penEasy for PENELOPE 2014*, 2015. [Online]. Available: https://inte.upc.edu/en/downloads/peneasy/Readme.

[64] The Phantom Lab., *Other Catphan and CT Phantoms*, 2017. [Online]. Available: https://www.phantomlab.com/other-catphans (visited on 07/20/2018).

[65] The Phantom Laboratory, *Catphan 504 Manual*, 2013. [Online]. Available: https://static1.squarespace.com/static/5367b059e4b05a1adcd295c2/t/551ae42be4b046662454b34
1427825707349/catphan504manual.pdf.

[66] F. Nordström, *ReadXim*, 2015. [Online]. Available: https://www.mathworks.com/matlabcentral/fileexchange/53367-readxim.

[67] J. M. Boone and J. A. Seibert, "An accurate method for computer-generating tungsten anode x-ray spectra from 30 to 140 kV," *Medical Physics*, vol. 24, no. 11, pp. 1661–1670, DOI: 10.1118/1.597953. [Online]. Available: https://aapm.onlinelibrary.wiley.com/doi/abs/10.1118/1.597953.

[68] M. R. Ay, S Sarkar, M Shahriari, D Sardari, and H Zaidi, "Assessment of different computational models for generation of x-ray spectra in diagnostic radiology and mammography," *Medical Physics*, vol. 32, no. 6Part1, pp. 1660–1675, DOI: 10.1118/1.1906126. [Online]. Available: https://aapm.onlinelibrary.wiley.com/doi/abs/10.1118/1.1906126.

[69] P Meyer, E Buffard, L Mertz, C Kennel, A Constantinesco, and P Siffert, "Evaluation of the use of six diagnostic X-ray spectra computer codes," *The British Journal of Radiology*, vol. 77, no. 915, pp. 224–230, 2004. DOI: 10.1259/bjr/32409995. [Online]. Available: https://doi.org/10.1259/bjr/32409995.

APPENDIX A

Detector Rotation and Source position and direction

A.1 Calculations of the Detector Rotation and Positioning

When rotating the detector 10° clockwise using the the code system PENELOPE, the rotation would occur relatively to the **Original Coordinate System**. To correct this and to guarantee its rotation relative to the **Rotational Coordinate System**, the shift values were calculated. We started by establishing two points (*P1* and *P2*), which were located at the extremities of the detector. The detector's thickness was ignored for it wasn't relevant for these calculations and it simplified the geometrical calculations. Figure A.1 illustrates the schematic taken into consideration for the following calculations, which is a simplified schematic where the computational phantom appears represented only as the CP.

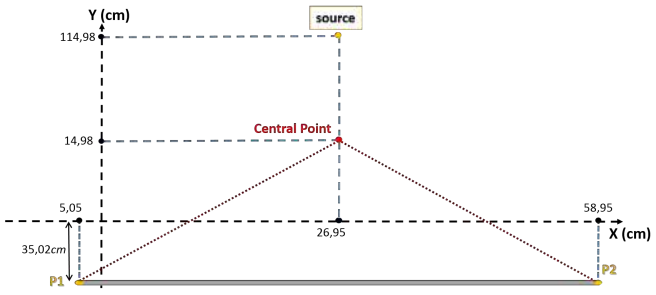

Figure A.1: This schematic is the z axis view or upper view of the computational phantom, which appears represented only as the Central Point, regarding the Original Coordinate System.

This schematic is the upper view and a more simplified version of the geometry used for the MC simulations, as previously seen in Figure 3.1. The only difference between

these two geometries is that in Figure 3.1 the source is positioned in front of the computational phantom and the detector is positioned behind it, while in the Figure A.1 the source is positioned behind the computational phantom and the detector is positioned in front of it. In order to guaranty consistency when referring to the position of the source and the detector, we used the following designation: a 0° geometry simulation is equivalent to a PA geometry, in which the radiation is incident on the back of the body [41]; and a 180° geometry simulation is equivalent to a AP geometry, in which the radiation is incident on the front of the body [41]. Therefore, Figure 3.1 represents a 180° geometry simulation while in Figure A.1 is representation of a 0° geometry simulation.

Starting with the 0° geometry (PA geometry), we calculated the coordinates assumed by the two points (P1 and P2) when these underwent a 10° clockwise rotation, therefore they would rotate 10° regarding the **Rotational Coordinate System** which has it's origin on point CP as shown in Figure A.2.

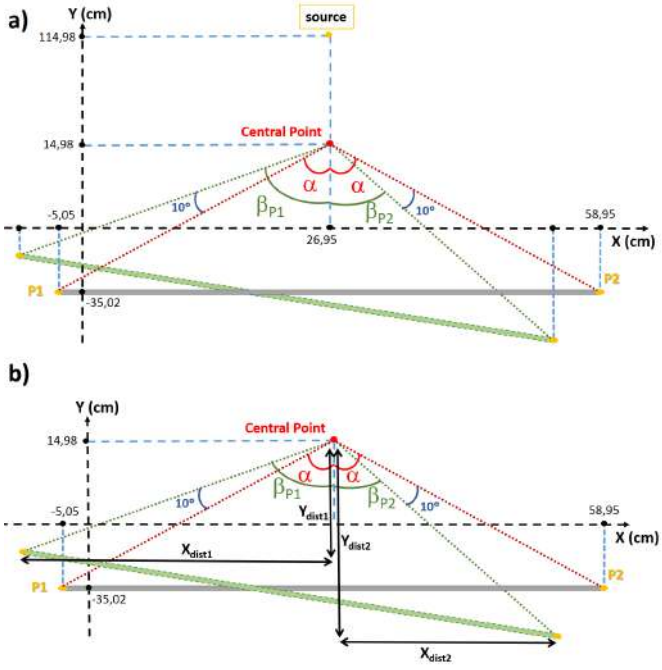

Figure A.2: Schematic of a 10° clockwise rotation of the detector shown in **a)** and the right triangles taken into consideration for calculations of the distances and final coordinates for points P1 and P2, shown in **b)**.

Given that P1 and P2 are edges of two right triangles as shown in Figure A.2 **b)**, they can be studied separately, for each right triangle assume a different angle after the rotation (β_{P1} and β_{P2}). By applying the trigonometric ratio tangent in Equation A.1 and the Pythagorean Theorem in Equation A.2 we obtain the following values for the

hypotenuse (h) and for the angle α:

$$\begin{aligned} \tan\alpha &= \frac{32}{50} \Leftrightarrow \\ \alpha &= \arctan\left(\frac{32}{50}\right) = 32.62° \quad (A.1) \\ h &= \sqrt{32^2 + 50^2} = 59.36\,\text{cm} \quad (A.2) \end{aligned}$$

Therefore, for a 10° clockwise rotation, not only will the points P1 and P2 assume new positions, but also will the angle α assume new values of β_{P1} and β_{P2} given by:

$$\beta_{P1} = \alpha + 10° = 42.62° \qquad \beta_{P2} = \alpha - 10° = 22.62°$$

and the new distances (X_{dist1}, Y_{dist1}) and (X_{dist2}, Y_{dist2}) as shown in Figure A.2 are given by:

$$\begin{cases} \sin\beta_{P1} = \frac{X_{dist1}}{h} \\ \sin\beta_{P2} = \frac{X_{dist2}}{h} \end{cases} \Leftrightarrow \begin{cases} X_{dist1} = h.\sin\beta_{P1} = 40.20\,\text{cm} \\ X_{dist2} = h.\sin\beta_{P2} = 22.83\,\text{cm} \end{cases}$$

$$\begin{cases} \cos\beta_{P1} = \frac{Y_{dist1}}{h} \\ \cos\beta_{P2} = \frac{Y_{dist2}}{h} \end{cases} \Leftrightarrow \begin{cases} Y_{dist1} = h.\cos\beta_{P1} = 43.68\,\text{cm} \\ Y_{dist2} = h.\cos\beta_{P2} = 54.80\,\text{cm} \end{cases}$$

The new coordinates of the points P1 and P2 after suffering a clockwise rotation of 10° relatively to the **Rotational Coordinate System** will be:

$$P1_{10} = \begin{cases} X_1 = 26.95 - X_{dist1} = -13.25\,\text{cm} \\ Y_1 = 14.98 - Y_{dist1} = -28.70\,\text{cm} \end{cases}$$

$$P2_{10} = \begin{cases} X_2 = 26.95 + X_{dist2} = 49.78\,\text{cm} \\ Y_2 = 14.98 - Y_{dist2} = -39.82\,\text{cm} \end{cases} \quad (A.3)$$

Note that in the system of Equations A.3 the distances (X_1, Y_1) and (X_2, Y_2) are subtracted or added to the constants $X = 26.95cm$ and $Y = 14.98cm$ depending on the angle of rotation for which we are studying. We established 4 quarters of the 360° rotation, in order to simplify calculations and denominated each one as 1st, 2nd, 3rd and 4th quarter as shown in Figure A.3.

After the points P1 and P2 suffer a rotation they will fall into one of these four quarters, and depending on which quarter they are located, we can determine their coordinates by applying the following calculations for each quarter:

$$2^{nd}Quarter \begin{cases} X = 26.95 - X_{dist} \\ Y = 14.98 + Y_{dist} \end{cases} \qquad 1^{st}Quarter \begin{cases} X = 26.95 + X_{dist} \\ Y = 14.98 + Y_{dist} \end{cases}$$

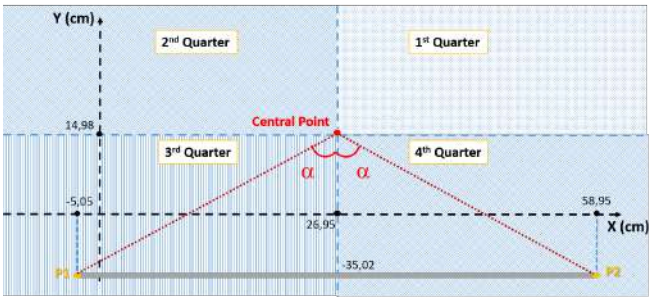

Figure A.3: Schematic of the four quarters of the 360° rotation that were established for calculation simplification purposes.

$$3^{rd}Quarter\begin{cases} X = 26.95 - X_{dist} \\ Y = 14.98 - Y_{dist} \end{cases} \qquad 4^{th}Quarter\begin{cases} X_1 = 26.95 + X_{dist1} \\ Y_1 = 14.98 - Y_{dist1} \end{cases} \tag{A.4}$$

The results for all the 36 angles regarding point P1 are listed in Table A.1 as for the results regarding point P2, they are listed in Table A.2.

However there are two variables, θ_{P1} and θ_{P2}, that appear in the data. These angles are angles used after a correction is made. When calculating bigger angles, for instance when P1 suffers a 60° clockwise rotation, given that the initial angle $\alpha = 32,62°$, $\beta_{P1} = 92,62$ and is situated in the $2^{nd}Quarter$. By subtracting 90° calculations are simplified, as the new angle $\theta_{P1} = \beta_{P1} - 90°$ and therefore we assume the schematic shown in Figure A.4.

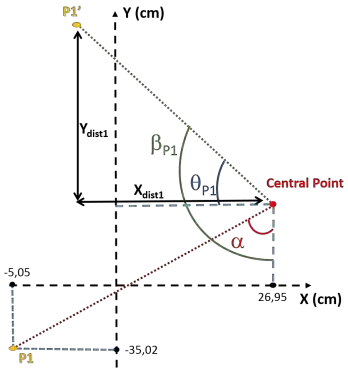

Figure A.4: Schematic of the rotation suffered by point P1 when dealing with big angles. In this case the simplification is done by establishing an angle θ_{P1} for calculating the distances and final coordinates after rotation occurs.

These simplifications in calculating θ_{P1} and θ_{P2} were also performed by subtracting 180° , 270° and in some cases 360° , as the angles β_{P1} and β_{P2} became bigger.

Now, for a clockwise rotation of 10° relatively to the **Original Coordinate System**, we will consider the schematic shown in Figure A.5, for the rotation will occur regarding the Origin of the coordinate system.

In this case P1 and P2 are also edges of two right triangles, and therefore we shall consider the triangles separately as shown in FigureA.6.

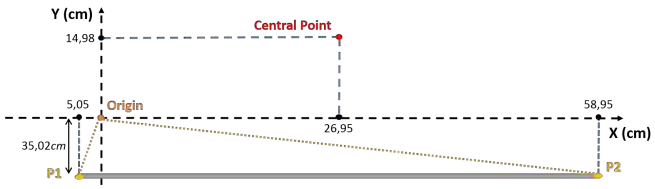

Figure A.5: Schematic of the rotation relatively to the Original Coordinate System. In this case the points will rotate relatively to the Origin.

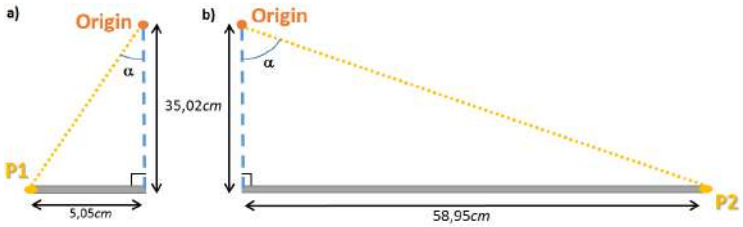

Figure A.6: Schematic of the **a)** right triangle for P1 and **b)** right triangle for P2 that were taken into consideration for further calculations.

By following the same methodology previously described we obtain the following values for both hypotenuses (h_{P1} and h_{P2}) and for the angles α_{P1} and α_{P2}:

$$h_{P1} = \sqrt{35.02^2 + 5.05^2} = 35.38 \text{ cm} \qquad h_{P2} = \sqrt{35.02^2 + 58.95^2} = 68.57 \text{ cm}$$

$$\begin{cases} \tan\alpha_{P1} = \frac{5.05}{35.02} \\ \tan\alpha_{P2} = \frac{58.95}{35.02} \end{cases} \Leftrightarrow \begin{cases} \alpha_{P1} = \arctan\left(\frac{5.05}{35.02}\right) = 8.21° \\ \alpha_{P2} = \arctan\left(\frac{58.95}{35.02}\right) = 59.29° \end{cases}$$

Therefore, for a 10° clockwise rotation regarding the **Original Coordinate System**, the new angles β_{P1} and β_{P2} are given by:

$$\beta_{P1} = \alpha_{P1} + 10° = 18.21° \qquad \beta_{P2} = \alpha_{P2} - 10° = 49.29°$$

and the new values for the P1 and P2 coordinates are given by:

$$P1_{10} = \begin{cases} X_1 = h_{P1}.\sin\beta_{P1} = 11.05 \text{ cm} \\ Y_1 = h_{P1}.\cos\beta_{P1} = 33.61 \text{ cm} \end{cases} \qquad P2_{10} = \begin{cases} X_2 = h_{P2}.\sin\beta_{P2} = 51.97 \text{ cm} \\ Y_2 = h_{P2}.\cos\beta_{P2} = 44.72 \text{ cm} \end{cases}$$

Note that in this case the calculated values are in fact the values of the coordinates for the points P1 and P2, and there was no need for adding or subtracting distances for this coordinate system is the **Original Coordinate System**. However these values need to be analyzed with caution for it hasn't been considered their position within the coordinate system and they have been treated as absolute values (or modulus values). Therefore, by analyzing Figure A.1 it's intuitive that $P1_{Orig10}$ will be found in the third quadrant and that $P2_{Orig10}$ will be found in the fourth quadrant, and so the coordinates for the points are:

$$P1_{Orig10} = \begin{cases} X_1 = -11.05 \text{ cm} \\ Y_1 = -33.61 \text{ cm} \end{cases} \qquad P2_{Orig10} = \begin{cases} X_2 = 51.97 \text{ cm} \\ Y_2 = -44.72 \text{ cm} \end{cases} \tag{A.5}$$

After calculating the coordinates for points P1 and P2 regarding the **Rotational Coordinate System** (Equation A.3) and the **Original Coordinate System** (Equation A.5), the correction values will be given by the difference between both coordinate systems for the same point, and therefore we obtain the following values:

$$Xaxis = \begin{cases} X1_{shift} = X(P1_{Orig10}) - X(P1_{10}) \\ X2_{shift} = X(P2_{Orig10}) - X(P2_{10}) \end{cases} \Leftrightarrow \begin{cases} X1_{shift} = -5.147 - (-7.34) = 2.19 \text{ cm} \\ X2_{shift} = 57.880 - 55.69 = 2.19 \text{ cm} \end{cases}$$

$$Yaxis = \begin{cases} Y1_{shift} = Y(P1_{Orig10}) - Y(P1_{10}) \\ Y2_{shift} = Y(P2_{Orig10}) - Y(P2_{10}) \end{cases} \Leftrightarrow \begin{cases} Y1_{shift} = -0.108 - 4.80 = -4.91 \text{ cm} \\ Y2_{shift} = -11.221 - (-6.31) = -4.91 \text{ cm} \end{cases}$$

As expected, the shifts for both points P1 and P2 in the X axis and in the Y axis are the same, this works as a good confirmation that there were no errors between calculations. These calculations were performed not only for the 10° rotation angle but also for all the other angles. The results obtained for all 36 angles are listed in Table A.3, where the results regarding points P1 and P2 are presented, and in Table A.4, where the shift results regarding the confirmation that there were no errors, are presented.

A.1.0.1 Source Position and Direction

The source position had to be calculated in order to account for the deviation of the phantom from the **Original Coordinate System**. Starting with the 0° geometry (PA geometry), as previously shown in Figure A.1, we easily determine that the source position is:

$$SourceCoordinates \begin{cases} X = 26.95 \text{ cm} \\ Y = 114.98 \text{ cm} \end{cases}$$

However, for a 10° clockwise rotation the answer isn't as trivial. Once again the 4 quarters approach (previously explained in Figure A.3) is used in order to simplify calculations. The source position was determined by applying the trigonometric ratio Sine and Cosine, given that in each quarter of the 360 ° rotation a right triangle can be detected regarding the angle τ, as shown in Figure A.7.

For each quarter, the distances X_{source} and Y_{source} were determined and the coordinates for the source were given by applying the calculations shown in the system of equations A.4. The results obtained for all 36 angles are listed in Table A.5.

Another important variable required for running the simulations is the source's direction. This variable is inserted into an entry within the Configuration File, for running MC simulations. To define the source's direction, the coordinates of a normalized vector for each source position, this is for each simulated angle, was calculated. In Table A.6, the vector coordinates for determining the source's direction for all 36 simulated angles are listed. The coordinates for the source position used in the MC simulations of a $CTDI_{100}$

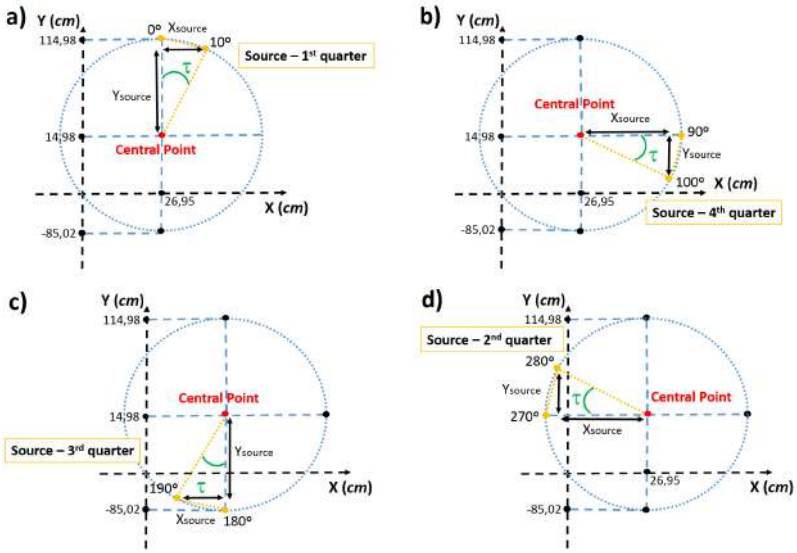

Figure A.7: Schematic of the four quarter simplification in the source rotation geometry. Schematic **a)** shows the geometry for calculating the distances X_{source} and Y_{source} in the 1^{st} quarter, **b)** shows the geometry for the 4^{th} quarter, **c)** for the 3^{rd} and **d)** for the 2^{nd}.

measurement model using a PMMA phantom, are also described, however for this model has a different angle orientation, where a 0°geometry of the simulation with the computational phantom (PA geometry), corresponds to the 180° geometry of the simulation with the PMMA phantom.

Table A.1: List of the angles and coordinates required for detector rotation, regarding point P1, according to the detector angle.

Angle	P1				Coordinates P1 (cm)	
(deg.)	β_{P1} (deg.)	θ_{P1} (deg.)	X_{dist1} (cm)	Y_{dist1} (cm)	X_1	Y_1
10	42.62	42.62	40.20	43,68	-13.25	-28.70
20	52.62	52.62	47.17	36.04	-20.22	-21.06
30	62.62	62.62	52.71	27.30	-25.76	-12.32
40	72.62	72.62	56.65	17.73	-29.70	-2.75
50	82.62	82.62	58.87	7.63	-31.92	7.35
60	92.62	2.62	59.30	2.71	-32.35	17.69
70	102.62	12.62	57.93	12.97	-30.98	27.95
80	112.62	22.62	54.80	22.83	-27.85	37.81
90	122.62	32.62	50.00	32.00	-23.05	46.98
100	132.62	42.62	43.68	40.20	-16.73	55.18
110	142.62	52.62	36.04	47.17	-9.09	62.15
120	152.62	62.62	27.30	52.71	-0.35	67.69
130	162.62	72.62	17.73	56.65	9.22	71.63
140	172.62	82.62	7.63	58.87	19.32	73.85
150	182.62	2.62	2.71	59.30	29.66	74.28
160	192.62	12.62	12.97	57.93	39.92	72.91
170	202.62	22.62	22.83	54.80	49.78	69.78
180	212.62	32.62	32.00	50.00	58.95	64.98
190	137.38	47.38	40.20	43.68	67.15	58.66
200	127.38	37.38	47.17	36.04	74.12	51.02
210	117.38	27.38	52.71	27.30	79.66	42.28
220	107.38	107.38	56.65	-17.73	83.60	32.71
230	97.38	97.38	58.87	-7.63	85.82	22.61
240	87.38	87.38	59.30	2.71	86.25	12.27
250	77.38	77.38	57.93	12.97	84.88	2.01
260	67.38	67.38	54.80	22.83	81.75	-7.85
270	57.38	57.38	50.00	32.00	76.95	-17.02
280	47.38	47.38	43.68	40.20	70.63	-25.22
290	37.38	37.38	36.04	47.17	62.99	-32.19
300	27.38	27.38	27.30	52.71	54.25	-37.73
310	17.38	-17.38	-17.73	56.65	44.68	-41.67
320	7.38	-7.38	-7.63	58.87	34.58	-43.89
330	-2.62	2.62	2.71	59.30	24.24	-44.32
340	-12.62	12.62	12.97	57.93	13.98	-42.95
350	-22.62	22.62	22.83	54.80	4.12	-39.82
360	-32.62	32.62	32.00	50.00	-5.05	-35.02

Table A.2: List of the angles and coordinates required for detector rotation, regarding point P2, according to the detector angle.

Angle	P2				Coordinates P2 (cm)	
(deg.)	β_{P2} (deg.)	θ_{P2} (deg.)	X_{dist2} (cm)	Y_{dist2} (cm)	X_2	Y_2
10	22.62	22.62	22.83	54.80	49.78	-39.82
20	12.62	12.62	12.97	57.93	39.92	-42.95
30	2.62	2.62	2.71	59.30	29.66	-44.32
40	7.38	7.38	7.63	58.87	19.32	-43.89
50	17.38	17.38	17.73	56.65	9.22	-41.67
60	27.38	27.38	27.30	52.71	-0.35	-37.73
70	37.38	37.38	36.04	47.17	-9.09	-32.19
80	47.38	47.38	43.68	40.20	-16.73	-25.22
90	57.38	57.38	50.00	32.00	-23.05	-17.02
100	67.38	67.38	54.80	22.83	-27.85	-7.85
110	77.38	77.38	57.93	12.97	-30.98	2.01
120	87.38	87.38	59.30	2.71	-32.35	12.27
130	97.38	7.38	58.87	7.63	-31.92	22.61
140	107.38	17.38	56.65	17.73	-29.70	32.71
150	117.38	27.38	52.71	27.30	-25.76	42.28
160	127.38	37.38	47.17	36.04	-20.22	51.02
170	137.38	47.38	40.20	43.68	-13.25	58.66
180	147.38	57.38	32.00	50.00	-5.05	64.98
190	157.38	67.38	22.83	54.80	4.12	69.78
200	167.38	77.38	12.97	57.93	13.98	72.91
210	177.38	87.38	2.71	59.30	24.24	74.28
220	187.38	7.38	7.63	58.87	34.58	73.85
230	197.38	17.38	17.73	56.65	44.68	71.63
240	207.38	27.38	27.30	52.71	54.25	67.69
250	217.38	37.38	36.04	47.17	62.99	62.15
260	227.38	47.38	43.68	40.20	70.63	55.18
270	237.38	57.38	50.00	32.00	76.95	46.98
280	247.38	67.38	54.80	22.83	81.75	37.81
290	257.38	77.38	57.93	12.97	84.88	27.95
300	267.38	87.38	59.30	2.71	86.25	17.69
310	277.38	7.38	58.87	7.63	85.82	7.35
320	287.38	17,38	56.65	17.73	83.60	-2.75
330	297.38	27.38	52.71	27.30	79.66	-12.32
340	307.38	37.38	47.17	36.04	74.12	-21.06
350	317.38	47.38	40.20	43.68	67.15	-28.70
360	327.38	57.38	32.00	50.00	58.95	-35.02

Table A.3: List of the shift values regarding each axis, required for detector rotation.

Angle	P1				P2			
(deg.)	β_{P1} (deg.)	θ_{P1} (deg.)	X_1 (cm)	Y_1 (cm)	β_{P2} (deg.)	θ_{P2} (deg.)	X_2 (cm)	Y_2 (cm)
10	18.21	18.21	-11.05	-33.61	49.29	49.29	51.97	-44.72
20	28.21	28.21	-16.72	-31.18	39.29	39.29	43.42	-53.07
30	38.21	38.21	-21.88	-27.80	29.29	29.29	33.54	-59.80
40	48.21	48.21	-26.38	-23.58	19.29	19.29	22.65	-64.72
50	58.21	58.21	-30.07	-18.64	9.29	9.29	11.07	-67.67
60	68.21	68.21	-32.85	-13.14	0.71	0.71	-0.85	-68.56
70	78.21	78.21	-34.64	-7.23	10.71	10.71	-12.75	-67.37
80	88.21	88.21	-35.36	-1.11	20.71	20.71	-24.25	-64.14
90	98.21	8.21	-35.02	5.05	30.71	30.71	-35.02	-58.95
100	108.21	18.21	-33.61	11.05	40.71	40.71	-44.72	-51.97
110	118.21	28.21	-31.18	16.72	50.71	50.71	-53.07	-43.42
120	128.21	38.21	-27.80	21.88	60.71	60.71	-59.80	-33.54
130	138.21	48.21	-23.58	26.38	70.71	70.71	-64.72	-22.65
140	148.21	58.21	-18.64	30.07	80.71	80.71	-67.67	-11.07
150	158.21	68.21	-13.14	32.85	90.71	0.71	-68.56	0.85
160	168.21	78.21	-7.23	34.64	100.71	10.71	-67.37	12.75
170	178.21	88.21	-1.11	35.36	110.71	20.71	-64.14	24.25
180	188.21	8.21	5.05	35.02	120.71	30.71	-58.95	35.02
190	198.21	18.21	11.05	33.61	130.71	40.71	-51.97	44.72
200	208.21	28.21	16.72	31.18	140.71	50.71	-43.42	53.07
210	218.21	38.21	21.88	27.80	150.71	60.71	-33.54	59.80
220	228.21	48.21	26.38	23.58	160.71	70.71	-22.65	64.72
230	238.21	58.21	30.07	18.64	170.71	80.71	-11.07	67.67
240	248.21	68.21	32.85	13.14	180.71	0.71	0.85	68.56
250	258.21	78.21	34.64	7.23	190.71	10.71	12.75	67.37
260	268.21	88.21	35.36	1.11	200.71	20.71	24.25	64.14
270	278.21	8.21	35.02	-5.05	210.71	30.71	35.02	58.95
280	288.21	18.21	33.61	-11.05	220.71	40.71	44.72	51.97
290	298.21	28.21	31.18	-16.72	230.71	50.71	53.07	43.42
300	308.21	38.21	27.80	-21.88	240.71	60.71	59.80	33.54
310	318.21	48.21	23.58	-26.38	250.71	70.71	64.72	22.65
320	328.21	58.21	18.64	-30.07	260.71	80.71	67.67	11.07
330	338.21	68.21	13.14	-32.85	270.71	0.71	68.56	-0.85
340	348.21	78.21	7.23	-34.64	280.71	10.71	67.37	-12.75
350	358.21	88.21	1.11	-35.36	290.71	20.71	64.14	-24.25
360	368.21	8.21	-5.05	-35.02	300.71	30.71	58.95	-35.02

Table A.4: List of the rectification of the shift values, for both axis, according to the rotation angle of the detector.

Angle	Shift X Axis (cm)			Shift Y Axis (cm)		
(deg.)	X_{1shift}	X_{2shift}	Confirmation	Y_{1shift}	Y_{2shift}	Confirmation
10	-2.19	-2.19	0.00	4.91	4.91	0.00
20	-3.50	-3.50	0.00	10.12	10.12	0.00
30	-3.88	-3.88	0.00	15.48	15.48	0.00
40	-3.32	-3.32	0.00	20.83	20.83	0.00
50	-1.85	-1.85	0.00	26.00	26.00	0.00
60	0.50	0.50	0.00	30.83	30.83	0.00
70	3.66	3.66	0.00	35.18	35.18	0.00
80	7.52	7.52	0.00	38.92	38.92	0.00
90	11.97	11.97	0.00	41.93	41.93	0.00
100	16.88	16.88	0.00	44.12	44.12	0.00
110	22.09	22.09	0.00	45.43	45.43	0.00
120	27.45	27.45	0.00	45.81	45.81	0.00
130	32.80	32.80	0.00	45.25	45.25	0.00
140	37.97	37.97	0.00	43.78	43.78	0.00
150	42.80	42.80	0.00	41.43	41.43	0.00
160	47.15	47.15	0.00	38.27	38.27	0.00
170	50.89	50.89	0.00	34.41	34.41	0.00
180	53.90	53.90	0.00	29.96	29.96	0.00
190	56.09	56.09	0.00	25.05	25.05	0.00
200	57.40	57.40	0.00	19.84	19.84	0.00
210	57.78	57.78	0.00	14.48	14.48	0.00
220	57.22	57.22	0.00	9.13	9.13	0.00
230	55.75	55.75	0.00	3.96	3.96	0.00
240	53.40	53.40	0.00	-0.87	-0.87	0.00
250	50.24	50.24	0.00	-5.22	-5.22	0.00
260	46.38	46.38	0.00	-8.96	-8.96	0.00
270	41.93	41.93	0.00	-11.97	-11.97	0.00
280	37.02	37.02	0.00	-14.16	-14.16	0.00
290	31.81	31.81	0.00	-15.47	-15.47	0.00
300	26.45	26.45	0.00	-15.85	-15.85	0.00
310	21.10	21.10	0.00	-15.29	-15.29	0.00
320	15.93	15.93	0.00	-13.82	-13.82	0.00
330	11.10	11.10	0.00	-11.47	-11.47	0.00
340	6.75	6.75	0.00	-8.31	-8.31	0.00
350	3.01	3.01	0.00	-4.45	-4.45	0.00
360	0.00	0.00	0.00	0.00	0.00	0.00

Table A.5: List of the source position regarding both Coordinate Systems (Original and Rotational) and the respective geometry system (PMMA geometry and Computational Phantom geometry).

PMMA Source Angles (deg.)	Original Coordinate System		Rotational Coordinate System		Computational Phantom Source Angles (deg.)
	X (cm)	Y (cm)	X (cm)	Y (cm)	
190	17.36	98.48	44.31	113.46	10
200	34.20	93.97	61.15	108.95	20
210	50.00	86.60	76.95	101.58	30
220	64.28	76.60	91.23	91.58	40
230	76.60	64.28	103.55	79.26	50
240	86.60	50.00	113.55	64.98	60
250	93.97	34.20	120.92	49.18	70
260	98.48	17.36	125.43	32.34	80
270	100.00	0.00	126.95	14.98	90
280	98.48	17.36	125.43	-2.38	100
290	93.97	34.20	120.92	-19.22	110
300	86.60	50.00	113.55	-35.02	120
310	76.60	64.28	103.55	-49.30	130
320	64.28	76.60	91.23	-61.62	140
330	50.00	86.60	76.95	-71.62	150
340	34.20	93.97	61.15	-78.99	160
350	17.36	98.48	44.31	-83.50	170
360	0.00	100.00	26.95	-85.02	180
10	17.36	98.48	9.59	-83.50	190
20	34.20	93.97	-7.25	-78.99	200
30	50.00	86.60	-23.05	-71.62	210
40	64.28	76.60	-37.33	-61.62	220
50	76.60	64.28	-49.65	-49.30	230
60	86.60	50.00	-59.65	-35.02	240
70	93.97	34.20	-67.02	-19.22	250
80	98.48	17.36	-71.53	-2.38	260
90	100.00	0,00	-73.05	14.98	270
100	98.48	17.36	-71.53	32.34	280
110	93.97	34.20	-67.02	49.18	290
120	86.60	50.00	-59.65	64.98	300
130	76.60	64.28	-49.65	79.26	310
140	64.28	76.60	-37.33	91.58	320
150	50.00	86.60	-23.05	101.58	330
160	34.20	93.97	-7.25	108.95	340
170	17.36	98.48	9.59	113.46	350
180	0.00	100.00	26.95	114.98	360

Table A.6: Vector coordinates for establishing the source direction, according to the detector's rotation angle.

Angle	Vector Coordinates (cm)	
(deg.)	X	Y
10	-0.17	-0.98
20	-0.34	-0.94
30	-0.50	-0.87
40	-0.64	-0.77
50	-0.77	-0.64
60	-0.87	-0.50
70	-0.94	-0.34
80	-0.98	-0.17
90	-1.00	0.00
100	-0.98	0.17
110	-0.94	0.34
120	-0.87	0.50
130	-0.77	0.64
140	-0.64	0.77
150	-0.50	0.87
160	-0.34	0.94
170	-0.17	0.98
180	0.00	1.00
190	0.17	0.98
200	0.34	0.94
210	0.50	0.87
220	0.64	0.77
230	0.77	0.64
240	0.87	0.50
250	0.94	0.34
260	0.98	0.17
270	1.00	0.00
280	0.98	-0.17
290	0.94	-0.34
300	0.87	-0.50
310	0.77	-0.64
320	0.64	-0.77
330	0.50	-0.87
340	0.34	-0.94
350	0.17	-0.98
360	0.00	-1.00

Appendix B

PenEasy files for performing the Monte Carlo Simulations

B.1 PenEasy.geo File

```
XXXXXXXXXXXXXXXXXXXXXXXXXXXXXXXXXXXXXXXXXXXXXXXXXXXXXXXXXXXXXXXXXXXXXXXXXXX
geometry
0000000000000000000000000000000000000000000000000000000000000000000000000000
SURFACE ( 30) Plane X=-5.05
INDICES=( 0, 0, 0, 0, 0)
AX=(+1.000000000000000E+00, 0)
A0=(+5.050000000000000E+00, 0)
0000000000000000000000000000000000000000000000000000000000000000000000000000
SURFACE ( 31) Plane X=58.95
INDICES=( 0, 0, 0, 0, 0)
AX=(+1.000000000000000E+00, 0)
A0=(-5.895000000000000E+01, 0)
0000000000000000000000000000000000000000000000000000000000000000000000000000
SURFACE ( 34) Plane Y=-35.045
INDICES=( 0, 0, 0, 0, 0)
AY=(+1.000000000000000E+00, 0)
A0=(+3.504500000000000E+01, 0)
0000000000000000000000000000000000000000000000000000000000000000000000000000
SURFACE ( 35) Plane Y=-35.02
INDICES=( 0, 0, 0, 0, 0)
AY=(+1.000000000000000E+00, 0)
A0=(+3.502000000000000E+01, 0)
```

```
0000000000000000000000000000000000000000000000000000000000000000
SURFACE ( 32) Plane Z=110.0
INDICES=( 0, 0, 0, 1, 0)
Z-SHIFT=( 1.100000000000000E+02, 0)
0000000000000000000000000000000000000000000000000000000000000000
SURFACE ( 33) Plane Z=150
INDICES=( 0, 0, 0, 1, 0)
Z-SHIFT=(+1.500000000000000E+02, 0)
0000000000000000000000000000000000000000000000000000000000000000
BODY ( 1) Detector
MATERIAL( 57)
SURFACE ( 30), SIDE POINTER=( 1)
SURFACE ( 31), SIDE POINTER=(-1)
SURFACE ( 32), SIDE POINTER=( 1)
SURFACE ( 33), SIDE POINTER=(-1)
SURFACE ( 34), SIDE POINTER=( 1)
SURFACE ( 35), SIDE POINTER=(-1)
0000000000000000000000000000000000000000000000000000000000000000
SURFACE ( 37) Sphere R=0.7 sphere calcification left lung
INDICES=( 1, 1, 1, 0,-1)
X-SCALE=(+7.000000000000000E-01, 0)
Y-SCALE=(+7.000000000000000E-01, 0)
Z-SCALE=(+7.000000000000000E-01, 0)
X-SHIFT=(+3.287000000000000E+01, 0)
Y-SHIFT=(+1.554000000000000E+01, 0)
Z-SHIFT=(+1.317000000000000E+02, 0)
00000000000000000000000000000000000000000
00000000000000000000
BODY ( 2) sphere calcification left lung
MATERIAL( 58)
SURFACE ( 37), SIDE POINTER=(-1)
0000000000000000000000000000000000000000000000000000000000000000
SURFACE ( 38) Sphere R=0.4 sphere calcification left breast
INDICES=( 1, 1, 1, 0,-1)
X-SCALE=(+4.000000000000000E-01, 0)
Y-SCALE=(+4.000000000000000E-01, 0)
Z-SCALE=(+4.000000000000000E-01, 0)
X-SHIFT=(+3.412000000000000E+01, 0)
Y-SHIFT=(+6.430000000000000E+00, 0)
Z-SHIFT=(+1.306500000000000E+02, 0)
0000000000000000000000000000000000000000000000000000000000000000
```

```
BODY ( 3) sphere calcification left breast
MATERIAL( 54)
SURFACE ( 38), SIDE POINTER=(-1)
00000000000000000000000000000000000000000000000000000000000000000000
SURFACE ( 29) Sphere R=450
INDICES=( 1, 1, 1, 0,-1)
X-SCALE=(+4.500000000000000E+02, 0)
Y-SCALE=(+4.500000000000000E+02, 0)
Z-SCALE=(+4.500000000000000E+02, 0)
X-SHIFT=(+2.695000000000000E+01, 0)
Y-SHIFT=(+1.498000000000000E+01, 0)
Z-SHIFT=(+1.313000000000000E+02, 0)
00000000000000000000000000000000000000000000000000000000000000000000
BODY ( 4) ar sphere
MATERIAL( 56)
SURFACE ( 29), SIDE POINTER=(-1)
BODY ( 1)
BODY ( 2)
BODY ( 3)
00000000000000000000000000000000000000000000000000000000000000000000
SURFACE ( 36) Sphere R=600
INDICES=( 1, 1, 1, 0,-1)
X-SCALE=(+6.000000000000000E+02, 0)
Y-SCALE=(+6.000000000000000E+02, 0)
Z-SCALE=(+6.000000000000000E+02, 0)
X-SHIFT=(+2.695000000000000E+01, 0)
Y-SHIFT=(+1.498000000000000E+01, 0)
Z-SHIFT=(+1.313000000000000E+02, 0)
00000000000000000000000000000000000000000000000000000000000000000000
MODULE ( 5) sphere with transpmat and detector
MATERIAL( 55)
SURFACE ( 36), SIDE POINTER=(-1)
BODY ( 1)
11111111111111111111111111111111111111111111111111111111111111111111
OMEGA=(-1.000000000000000E+01, 0) DEG
THETA=(+0.000000000000000E+00, 0) DEG
PHI=(+0.000000000000000E+00, 0) DEG
X-SHIFT=(-2.191819000000000E+00, 0) (DEFAULT=0.0)
Y-SHIFT=(+4.907398000000000E+00, 0) (DEFAULT=0.0)
Z-SHIFT=(+0.000000000000000E+00, 0) (DEFAULT=0.0)
00000000000000000000000000000000000000000000000000000000000000000000
```

END
0000000000000000000000000000000000000000000000000000000000000000

B.2 PenEasy.in File

```
# »» CONFIG FILE FOR penEasy »»»»»»»»»»»»»»»»»»»»»»
#
# CASE DESCRIPTION:
# Sample config file adapted to the example described in the READM
# file. Before editing this file, read carefully the instructions
# provided here after the data sections and in the README file.
#
# LAST UPDATE:
# 2015-05-26 by JS

# »»»»»»»»»»»»»»»»»»»»»»»»»»»»»»»»»»»»»»»»»»»»»»»»>
# GENERAL INSTRUCTIONS
#
# * Lines starting with a '#' (in column 1) and blank lines are
#   comments. Comments are NOT allowed inside data sections.
#
# * Do not change the order in which sections appear, neither the
#   order of data fields in each section.
#
# * Each data section has a version number of the form yyyy-mm-dd that is
#   written in the corresponding section title. Should an incorrect
#   version be introduced an error message would be issued and the
#   execution halted.
#
# * Character strings (e.g. file names) are introduced in free-format
#   style, that is, leading and trailing blanks are allowed. Their
#   maximum extension (except when noted) is 80 characters and they must
#   not contain blanks. Thus, for instance, 'stainless steel' should be
#   introduced as 'stainlessSteel' or 'stainless_Steel'.
#
# * Most syntax errors can be easily identified by looking for error
#   messages or inconsistencies within the last lines of penEasy output.
#   It is always a good idea to check the output to make sure that the
#   information written after processing each section coincides with what
#   is expected from the input.

# »»»»»»»»»»»»»»»»»»»»»»»»»»»»»»»»»»»»»»»»»»»»»»»»>
# INSTRUCTIONS FOR SECTION CONFIG
#
# * Details on the simulation configuration are provided with their
#   documentation (see   /documentation/*).
[SECTION CONFIG v.2013-03-18]
1.0e12           NUMBER OF HISTORIES (1.0e15 MAX)
1.0e30           ALLOTTED TIME (s) (+ FOR REAL TIME; - FOR CPU TIME)
100.0            UPDATE INTERVAL (s)
1 1              INITIAL RANDOM SEEDS
-                SEEDS FILE; MUST ENTER SEEDS=0,0 TO APPLY
-                RESTART FILE; MUST ENTER SEEDS=-1,-1 TO APPLY
penEasy.dmp      OUTPUT DUMP FILE; ENTER '-' FOR 'NO DUMP'
1800.0           INTERVAL BETWEEN DUMPS (s)
[END OF CONFIG SECTION]

# »»»»»»»»»»»»»»»»»»»»»»»»»»»»»»»»»»»»»»»»»»»»»»»»>
# INSTRUCTIONS FOR SOURCE SECTIONS
#
# * Details on the features and configuration of each source model
#    are provided with their documentation (see  /documentation/*).
#    Notice that there must be one and only one active (status ON) source model.

[SECTION SOURCE BOX ISOTROPIC GAUSS SPECTRUM v.2014-12-21]
ON                       STATUS (ON or OFF)
```

```
2                        PARTICLE TYPE (1=ELECTRON, 2=PHOTON, 3=POSITRON)
  SUBSECTION FOR PHOTON POLARIZATION:
0                        ACTIVATE PHOTON POLARIZATION PHYSICS (0=NO, 1=YES)
0.0 0.0 0.0              STOKES PARAMETERS (UNUSED IF ACTIVATE POLARIZATION=0)
  SUBSECTION FOR PARTICLE POSITION:
44.314818 113.460775 130.0COORDINATES (cm) OF BOX CENTER
0.0 0.0 0.0              BOX SIDES (cm)
0.0 0.0                  FWHMs (cm) OF GAUSSIAN X,Y DISTRIBUTIONS
0.0 0.0 0.0              EULER ANGLES [OMEGA,THETA,PHI](deg) FOR BOX ROTATION Rz(PHI).Ry(THETA).Rz(OMEGA).r
0.0 0.0 0.0              TRANSLATION [DX,DY,DZ](cm) OF BOX CENTER POSITION
0                        SOURCE MATERIAL (0=DON’T CARE, >0 FOR LOCAL SOURCE, <0 FOR IN-FIELD BEAM)
  SUBSECTION FOR PARTICLE DIRECTION:
-0.173648 -0.984808 0.0  DIRECTION VECTOR; NO NEED TO NORMALIZE
0.0 25.0                 DIRECTION POLAR ANGLE INTERVAL [THETA0,THETA1], BOTH VALUES IN [0,180]deg
0.0 360.0                DIRECTION AZIMUTHAL ANGLE INTERVAL PHI0 IN [0,360)deg AND DeltaPHI IN [0,360]deg
1                        APPLY ALSO TO DIRECTION THE ROTATION USED FOR BOX POSITION (0=NO, 1=YES)
  SUBSECTION FOR PARTICLE ENERGY:
-                        ENERGY SPECTRUM FILE NAME; ENTER ’-’ TO ENTER SPECTRUM IN NEXT LINES
Energy(eV)  Probability   DUMMY SPECTRUM HEADER LINE; REMOVE HEADER AND TABLE IF A FILENAME WAS PROVIDED ABOVE
80000       1.0           Spectrum table, arbitrary normalization. Example: a single channel [10,10]MeV of null width
80000       -1.0          Enter a negative prob. to signal the end of the table
0.0                       FWHM(eV) OF GAUSSIAN ENERGY DISTRIB. [NOTE FWHM=SIGMA*sqrt(8*ln(2))]
[END OF BIGS SECTION]

[SECTION SOURCE PHASE SPACE FILE v.2009-06-15]
OFF            STATUS (ON or OFF)
0              PSF FORMAT (0=STANDARD penEasy ASCII, 1=IAEA BINARY)
particles.psf  PSF FILENAME, REMOVE EXTENSION IF PSF FORMAT=1
1              SPLITTING FACTOR
0.0 0.0 0.0    EULER ANGLES [Rz,Ry,Rz](deg) TO ROTATE POSITION AND DIRECTION
0.0 0.0 0.0    TRANSLATION [DX,DY,DZ](cm) OF POSITION
1              VALIDATE BEFORE SIMULATION (1=YES, MAY TAKE A WHILE; 0=NO)
0.000e0        MAX PSF ENERGY (eV) (UNUSED IF VALIDATE=1 OR IAEA FORMAT; ADD 1023 keV FOR e+)
[END OF SPSF SECTION]

# »»»»»»»»»»»»»»»»»»»»»»»»»»»»»»»»»>
# INSTRUCTIONS FOR SECTION PENGEOM+PENVOX
#
# * Enter either: (i) a file name in the QUADRICS FILE field and a dash ’-’ in
#   the VOXELS FILE field if you want to define only a quadric geometry model;
#   (ii) a file name in the VOXELS FILE field and a dash ’-’ in the QUADRICS
#   FILE field if you want to define only a voxelized geometry model; or (iii)
#   both a quadrics and a voxelized file names in the corresponding fields if
#   you want to define a combination of overlapping quadrics and voxelized models.
#
# * The TRANSPARENT QUADRIC MAT and GRANULARITY field are used only if both a
#   quadric and a voxel geometries are defined. Otherwise they are irrelevant.
#
# * Details on the use and configuration of these geometry models are provided
#   in the documentation (please refer to ˜/documentation/*).

[SECTION PENGEOM+PENVOX v.2009-06-15]
10regina.geo            QUADRICS FILE NAME, USE ’-’ IF NONE
regina.vox              VOXELS FILE NAME, USE ’-’ IF NONE
56                      TRANSPARENT QUADRIC MAT (USED ONLY IF QUAD&VOX)
10                      GRANULARITY TO SCAN VOXELS (USED ONLY IF QUAD&VOX)
[END OF GEO SECTION]

# »»»»»»»»»»»»»»»»»»»»»»»»»»»»»»»»»>
# INSTRUCTIONS FOR SECTION PENELOPE
#
# * Write one line of data per defined material. Each line starts with
#   the material index (MAT#), which should be an integer starting from 1.
#   Set MAT# to zero in the last line to denote the end of the list.
#
# * Use 20 characters at most to introduce the material data file name.
#   Blanks or special characters are not allowed in file names. Thus,
#   instead of "stainless steel.mat"use "stainlessSteel.mat".
#
```

```
# * If, for a certain material, the transport parameters after the file
#   name are left empty, then they are set automatically as follows:
#     -Eabs for charged particles are set to 1% of the
#     initial source energy (E), with the limiting values of 50 eV
#     (min) and 1 MeV (max).
#     -Eabs for photons is set to 0.1% E with the limiting values of
#     50 eV and 1 MeV.
#     -C1 and C2 are both set to 0.1.
#     -WCC is set to min(Eabs(e-),1% E).
#     -WCR is set to min(Eabs(phot),0.1% E).
#     -DSMAX is set to infinity.
#
# * Do not remove the line containing the table header "MAT# FILE...".

[SECTION PENELOPE v.2009-10-01]
MAT# FILE___(max 20 char) EABS(e-) EABS(ph) EABS(e+) C1   C2  WCC  WCR  DSMAX  COMMENTS
 1    Teeth.mat            8e4      5e3      8e4      0.2  0.2  5e3  4e3 1.0e30
 2    Mineralbone.mat      8e4      5e3      8e4      0.2  0.2  5e3  4e3 1.0e30
 3    Humeriupsponge.mat   8e4      5e3      8e4      0.2  0.2  5e3  4e3 1.0e30
 4    Humerilowsponge.mat  8e4      5e3      8e4      0.2  0.2  5e3  4e3 1.0e30
 5    LowArmsponge.mat     8e4      5e3      8e4      0.2  0.2  5e3  4e3 1.0e30
 6    Handsponge.mat       8e4      5e3      8e4      0.2  0.2  5e3  4e3 1.0e30
 7    Claviclesponge.mat   8e4      5e3      8e4      0.2  0.2  5e3  4e3 1.0e30
 8    Craniumsponge.mat    8e4      5e3      8e4      0.2  0.2  5e3  4e3 1.0e30
 9    Femurupsponge.mat    8e4      5e3      8e4      0.2  0.2  5e3  4e3 1.0e30
10    Femurlowsponge.mat   8e4      5e3      8e4      0.2  0.2  5e3  4e3 1.0e30
11    Legbones.mat         8e4      5e3      8e4      0.2  0.2  5e3  4e3 1.0e30
12    Footbones.mat        8e4      5e3      8e4      0.2  0.2  5e3  4e3 1.0e30
13    Mandible.mat         8e4      5e3      8e4      0.2  0.2  5e3  4e3 1.0e30
14    Pelvis.mat           8e4      5e3      8e4      0.2  0.2  5e3  4e3 1.0e30
15    Ribs.mat             8e4      5e3      8e4      0.2  0.2  5e3  4e3 1.0e30
16    Scapulae.mat         8e4      5e3      8e4      0.2  0.2  5e3  4e3 1.0e30
17    Cervicalspine.mat    8e4      5e3      8e4      0.2  0.2  5e3  4e3 1.0e30
18    Thoracicspine.mat    8e4      5e3      8e4      0.2  0.2  5e3  4e3 1.0e30
19    Lumbarspine.mat      8e4      5e3      8e4      0.2  0.2  5e3  4e3 1.0e30
20    Sacrum.mat           8e4      5e3      8e4      0.2  0.2  5e3  4e3 1.0e30
21    Sternum.mat          8e4      5e3      8e4      0.2  0.2  5e3  4e3 1.0e30
22    HumerFemupcavity.mat 8e4      5e3      8e4      0.2  0.2  5e3  4e3 1.0e30
23    HumerFemlocavity.mat 8e4      5e3      8e4      0.2  0.2  5e3  4e3 1.0e30
24    Armbonescavity.mat   8e4      5e3      8e4      0.2  0.2  5e3  4e3 1.0e30
25    Legbonescavity.mat   8e4      5e3      8e4      0.2  0.2  5e3  4e3 1.0e30
26    Cartilage.mat        8e4      5e3      8e4      0.2  0.2  5e3  4e3 1.0e30
27    Skin.mat             8e4      5e3      8e4      0.2  0.2  4e3  4e3 1.0e30
28    Blood.mat            8e4      5e3      8e4      0.2  0.2  4e3  4e3 1.0e30
29    MuscleTissue.mat     8e4      5e3      8e4      0.2  0.2  4e3  4e3 1.0e30
30    Liver.mat            8e4      5e3      8e4      0.2  0.2  4e3  4e3 1.0e30
31    Pancreas.mat         8e4      5e3      8e4      0.2  0.2  4e3  4e3 1.0e30
32    Brain.mat            8e4      5e3      8e4      0.2  0.2  4e3  4e3 1.0e30
33    Heart.mat            8e4      5e3      8e4      0.2  0.2  4e3  4e3 1.0e30
34    Eyes.mat             8e4      5e3      8e4      0.2  0.2  4e3  4e3 1.0e30
35    Kidney.mat           8e4      5e3      8e4      0.2  0.2  4e3  4e3 1.0e30
36    Stomach.mat          8e4      5e3      8e4      0.2  0.2  4e3  4e3 1.0e30
37    Smallintestine.mat   8e4      5e3      8e4      0.2  0.2  4e3  4e3 1.0e30
38    Largeintestine.mat   8e4      5e3      8e4      0.2  0.2  4e3  4e3 1.0e30
39    Spleen.mat           8e4      5e3      8e4      0.2  0.2  4e3  4e3 1.0e30
40    Thyroid.mat          8e4      5e3      8e4      0.2  0.2  4e3  4e3 1.0e30
41    Bladder.mat          8e4      5e3      8e4      0.2  0.2  4e3  4e3 1.0e30
42    Ovaries.mat          8e4      5e3      8e4      0.2  0.2  4e3  4e3 1.0e30
43    Adrenals.mat         8e4      5e3      8e4      0.2  0.2  4e3  4e3 1.0e30
44    Oesophagus.mat       8e4      5e3      8e4      0.2  0.2  4e3  4e3 1.0e30
45    Material45.mat       8e4      5e3      8e4      0.2  0.2  5e3  4e3 1.0e30
46    Uterus.mat           8e4      5e3      8e4      0.2  0.2  4e3  4e3 1.0e30
47    Lymph.mat            8e4      5e3      8e4      0.2  0.2  4e3  4e3 1.0e30
48    Breast.mat           8e4      5e3      8e4      0.2  0.2  4e3  4e3 1.0e30
49    AdiposeTissue.mat    8e4      5e3      8e4      0.2  0.2  4e3  4e3 1.0e30
50    LungTissue.mat       8e4      5e3      8e4      0.2  0.2  4e3  4e3 1.0e30
51    Intestincontent.mat  8e4      5e3      8e4      0.2  0.2  4e3  4e3 1.0e30
52    Urine.mat            8e4      5e3      8e4      0.2  0.2  4e3  4e3 1.0e30
53    Air.mat              8e4      5e3      8e4      0.2  0.2  4e3  4e3 1.0e30
```

```
54   Calbreast.mat       8e4      5e3      8e4     0.2  0.2  4e3  4e3 1.0e30
55   Airmodule.mat       8e4      5e3      8e4     0.2  0.2  4e3  4e3 1.0e30
56   Airtransp.mat       8e4      5e3      8e4     0.2  0.2  4e3  4e3 1.0e30
57   Se.mat              3e9      3e9      3e9     0.2  0.2  5e3  1e4 1.0e30
58   Calcification.mat   8e4      5e3      8e4     0.2  0.2  4e3  4e3 1.0e30
0
[END OF PEN SECTION]

# »»»»»»»»»»»»»»»»»»»»»»»»»»»»»»»»»>
# INSTRUCTIONS FOR THE TALLY SECTIONS
#
# * Details on the features and configuration of each tally are provided
#   with their documentation (see  /documentation/*.txt).
#
# * The required RELATIVE UNCERTAINTY that is specified for each tally
#   (except for those that do not have an associated uncertainty, e.g.
#   a phase-space file) is used as a condition to stop the simulation. Only
#   when the requested relative uncertainties of *all* the tallies have
#   been attained the uncertainty condition is considered fulfilled.
#   Recall that the simulation can also be halted because the allotted
#   time or the number of histories requested have been reached. Setting
#   the RELATIVE UNCERTAINTY of all tallies to zero will prevent the
#   execution from stopping for this cause.
#
# * Note for advanced users: when a certain tally scores nothing (i.e.
#   zero) the corresponding REPORT routine reports 0% uncertainty but, at
#   the same time, it reports that the requested uncertainty has not been
#   reached, irrespective of the value introduced in the config file.
#   This is to prevent the simulation from being stopped by a deceptive
#   impression of accuracy in highly inefficient simulations, where the
#   score and its standard deviation after a short period of time can be
#   null.

[SECTION TALLY VOXEL DOSE v.2014-12-27]
OFF              STATUS (ON or OFF)
0  0             ROI MIN,MAX X-INDEX (0 0 FOR ALL VOXELS)
0  0             ROI MIN,MAX Y-INDEX (0 0 FOR ALL VOXELS)
0  0             ROI MIN,MAX Z-INDEX (0 0 FOR ALL VOXELS)
0                PRINT VOXELS MASS IN REPORT (1=YES,0=NO)
1                PRINT COORDINATES IN REPORT (1=YES,0=NO,-1=NO&BINARYFORMAT)
0.0              RELATIVE UNCERTAINTY (%) REQUESTED
[END OF VDD SECTION]

[SECTION TALLY SPATIAL DOSE DISTRIB v.2009-06-15]
OFF              STATUS (ON or OFF)
0.0  0.0  0      XMIN,XMAX(cm),NXBIN (0 FOR DX=infty)
0.0  0.0  0      YMIN,YMAX(cm),NYBIN (0 FOR DY=infty)
0.0  7.0  40     ZMIN,ZMAX(cm),NZBIN (0 FOR DZ=infty)
1                PRINT COORDINATES IN REPORT (1=YES,0=NO,-1=NO&BINARYFORMAT)
1.0              RELATIVE UNCERTAINTY (%) REQUESTED
[END OF SDD SECTION]

[SECTION TALLY CYLINDRICAL DOSE DISTRIB v.2009-06-15]
OFF              STATUS (ON or OFF)
0.0  8.0  80     RMIN,RMAX(cm),NRBIN (>0)
0.0  7.0  40     ZMIN,ZMAX(cm),NZBIN (0 FOR DZ=infty)
1                PRINT COORDINATES IN REPORT (1=YES,0=NO)
0.0              RELATIVE UNCERTAINTY (%) REQUESTED
[END OF CDD SECTION]

[SECTION TALLY SPHERICAL DOSE DISTRIB v.2009-06-15]
OFF              STATUS (ON or OFF)
0.0  1.0  50     RMIN,RMAX(cm),NRBIN (>0)
1                PRINT COORDINATES IN REPORT (1=YES,0=NO)
0.0              RELATIVE UNCERTAINTY (%) REQUESTED
[END OF SPD SECTION]

[SECTION TALLY ENERGY DEPOSITION v.2012-06-01]
ON              STATUS (ON or OFF)
```

```
57              DETECTION MATERIAL
1.0             RELATIVE UNCERTAINTY (%) REQUESTED
[END OF EDP SECTION]

[SECTION TALLY PULSE HEIGHT SPECTRUM v.2012-06-01]
OFF              STATUS (ON or OFF)
1                DETECTION MATERIAL
0.0  1.0e9  100  EMIN,EMAX(eV), No. OF E BINS
0.0  0.0         A(eV2̂),B(eV) FOR GAUSSIAN CONVOLUTION FWHM[eV] sqrt(A+B*E[eV])
0.0              RELATIVE UNCERTAINTY (%) REQUESTED
[END OF PHS SECTION]

[SECTION TALLY PIXELATED IMAGING DETECTOR v.2015-02-06]
ON       STATUS (ON or OFF)
57       DETECTION MATERIAL
-1       FILTER PHOTON INTERACTION (0=NOFILTER, -1=UNSCATTERED, 1=RAYLEIGH, 2=COMPTON, 3=SECONDARIES, 9=MULTISCATTERED)
0  600   X-PIXEL SIZE(cm), No. X-PIXELS (ENTER 0 IN EITHER FIELD FOR AUTO)
0  500   Y-PIXEL SIZE(cm), No. Y-PIXELS (ENTER 0 IN EITHER FIELD FOR AUTO)
1        DETECTION MODE (1=ENERGY INTEGRATING, 2=PHOTON COUNTING, 3=PHOTON ENERGY DISCRIMINATING aka SPECTRUM)
1.0e3            ENERGY DEPOSITION THRESHOLD (eV) FOR MODE=2 (IGNORED FOR OTHER MODES)
0.0e0 1.0e9 100  EMIN,EMAX(eV), No. OF E BINS FOR MODE=3 (IGNORED FOR OTHER MODES)
0.0  0.0         ENERGY RESOLUTION, ENTER A(eV2̂),B(eV) FOR A GAUSSIAN WITH FWHM[eV]=sqrt(A+B*E[eV])
2                REPORT FORMAT (1=COLUMNAR, 2=MATRIX, 3=BINARY)
1.0              RELATIVE UNCERTAINTY (%) REQUESTED
[END OF PID SECTION]

[SECTION TALLY FLUENCE TRACK LENGTH v.2012-06-01]
OFF              STATUS (ON or OFF)
1                DETECTION MATERIAL
1.0e2 1.0e9 70 LOGEMIN,EMAX(eV), No. OF E BINS, APPEND 'LOG' FOR A LOG SCALE
0.0              RELATIVE UNCERTAINTY (%) REQUESTED
[END OF FTL SECTION]

[SECTION TALLY PHASE SPACE FILE v.2009-06-15]
OFF              STATUS (ON or OFF)
0                PSF FORMAT (0=STANDARD penEasy ASCII, 1=IAEA BINARY)
1                DETECTION MATERIAL (MUST BE A PERFECT ABSORBENT, EABS=+infty)
output.psf       PSF FILENAME, REMOVE EXTENSION IF FORMAT=1
[END OF PSF SECTION]

[SECTION TALLY PARTICLE CURRENT SPECTRUM v.2009-06-15]
OFF              STATUS (ON or OFF)
1                DETECTION MATERIAL
0.0  1.0e9  100  EMIN,EMAX(eV), No. OF E BINS
0.0              RELATIVE UNCERTAINTY (%) REQUESTED
[END OF PCS SECTION]

[SECTION TALLY PARTICLE TRACK STRUCTURE v.2009-06-15]
OFF              STATUS (ON or OFF)
100              NUMBER OF HISTORIES TO DISPLAY (1̃00 RECOMMENDED)
[END OF PTS SECTION]

# »»»»»»»»»»»»»»»»»»»»»»»»»»»»»»»»»»»»»»>
# INSTRUCTIONS FOR VARIANCE-REDUCTION SECTIONS
#
# * Details on the features and configuration of each VR technique are provided
#   with their documentation (see /̃documentation/*.txt).

[SECTION INTERACTION FORCING v.2009-06-15]
OFF                         STATUS (ON or OFF)
1.0                         DON'T APPLY BELOW THIS STATISTICAL WEIGHT
MAT   KPAR   ICOL   FORCING (SET MAT=-1 TO END LIST)
-1    0      0      1.0
[END OF VRIF SECTION]

[SECTION SPLITTING v.2015-05-30] |
OFF              STATUS (ON or OFF)
1.0              WGHTMIN, DO NOT SPLIT BELOW THIS STATISTICAL WEIGHT
1                SPLITTING MATERIAL
```

```
1               SPLITTING MODE (1=SIMPLE; 2=ROTATIONAL; 3=XY)
1               SPLITTING FACTOR, IGNORED FOR MODE=3
0.0  0.0  0.0   EULER ANGLES [Rz,Ry,Rz](deg), IGNORED FOR MODE=1
0.0  0.0  0.0   SHIFT (cm), IGNORED FOR MODE=1
0               SIGN OF W ('+', '-' OR '0'=BOTH), IGNORED FOR MODE=1
0.0  360.0      AZIMUTHAL INTERVAL PHI0 IN [0,360)deg AND DeltaPHI IN (0,360]deg, USED ONLY IF MODE=2
[END OF VRS SECTION]

[SECTION RUSSIAN ROULETTE v.2009-06-15]
OFF             STATUS (ON or OFF)
1.0             WGHTMAX, DO NOT PLAY ABOVE THIS STATISTICAL WEIGHT
1               RUSSIAN ROULETTE MATERIAL
1.0             SURVIVAL PROBABILITY

[END OF VRRR SECTION]

# »» END OF FILE ««««««««««««««««««««««««««
```

B.3 Description for each entry of the penEasy.in File

- `[SECTION CONFIG v.2013-03-18]`:
  - `NUMBER OF HISTORIES [1.0e12]`: Is the number of simulated particles and their track. For a minor statistical uncertainty and more reliable results a great number of histories must be simulated, but at the expense of the increase of computational time;
  - `ALLOTTED TIME [1.0e30]`: Is considered to be real time if it's a positive number, otherwise it's considered CPU time;
  - `UPDATE INTERVAL [100.0]`: Is the update time for when tallies write (or rewrite over) a report to the disk;
  - `INITIAL RANDOM SEEDS`: Which doesn't apply in this case and therefore the entry is `[1 1]`;
  - `OUTPUT DUMP FILE [penEasy.dmp]`: Where a filename for generating a dump file is established;
  - `INTERVAL BETWEEN DUMPS [1800.0]`: Elapsed time after which the dump file is written or updated.
- `[SECTION SOURCE BOX ISOTROPIC GAUSS SPECTRUM v.2014-12-21]`:
  - `STATUS [ON]`: Specification for using this section which can be ON or OFF;
  - `PARTICLE TYPE [2]`: Specification of the particle type that can be one of the following: 1=electron, 2=photon or 3=positron.

    `SUBSECTION FOR PHOTON POLARIZATION`
  - This subsection is for the use of polarized photons, which wasn't applied in this case therefore its entries were all considered to be `[0]`.

    `SUBSECTION FOR PARTICLE POSITION`

- `COORDINATES OF BOX CENTER`: Particles are, by default, generated inside a rectangular box and its position is given by these coordinates in cm. These coordinates were determined accordingly to the simulation in cause as described in section A.1.0.1 *Source Position Calculations* and are listed in Appendix A, Table A.5;
- `BOX SIDES`: The source box size is determined by three box sides, along the x, y and z directions, however for a point source we established these sides as `[0.0 0.0 0.0]`. Given that we are simulating an isotropic point source, the following input lines don't apply and therefore were considered `[0.0]`.

`SUBSECTION FOR PARTICLE DIRECTION`

- `DIRECTION VECTOR`: These are the coordinates of a vector that defines the direction of particle emission. These coordinates were determined accordingly to the source position, and therefore, to the angle in cause, as listed in Appendix A Table A.6;
- `DIRECTION POLAR ANGLE INTERVAL [0.0 25.0]`: Given that the direction of emission is isotropic within a spherical trapezoid, for a source limited to a cone, the base of the cone can be thought of as a particular case of a spherical trapezoid with `THETA0=0` and `THETA1` equal to the cone angular semi-aperture. The main concern is that the direction vector (cone axis) and the angular semi-aperture of the cone should be selected so that the simulated source fully 'illuminates' the irradiated object, and therefore the semi-aperture was considered 25°. This was taken into consideration when the detector dimensions were specified, as mentioned in section 3.1.1 *Geometry construction*;
- `DIRECTION AZIMUTHAL ANGLE INTERVAL [ 0.0 360.0]`: The direction azimuthal angle interval `PHI0` is irrelevant when dealing with a source limited to a cone, since the azimuthal interval covers a full circle, however `DeltaPHI` should be set for 360°;
- `APPLY ALSO TO DIRECTION THE ROTATION [1]`: When the reference system in which these spherical coordinates are given are different from the reference system used to define the geometry file, the direction vector previously introduced in the entry `DIRECTION VECTOR` is considered. Therefore, this entry is to assure that these spherical coordinates are applied to the direction vector.

`SUBSECTION FOR PARTICLE ENERGY`

- `ENERGY SPECTRUM FILE NAME`: For the case of uploading a pre-existing file with the energy spectrum of the simulated particle;
- `DUMMY SPECTRUM HEADER LINE`: The source's energy spectrum is introduced in this line. To simulate a monochromatic continuous beam of $80keV$ the energy and probability were set to `[80000 1.0]`.

- `[SECTION SOURCE PHASE SPACE FILE v.2009-06-15]`: This section is for the use of phase-space files, which doesn't apply to this case and therefore was considered `[OFF]`.

- `[SECTION PENGEOM+PENVOX v.2009-06-15]`:

  - `QUADRICS FILE NAME [geometry.geo]`: The name of the quadric geometry file is introduced. The geometrical model is introduced as described in the subsection 3.1.2.1 **Geometry Data File**;

  - `VOXELS FILE NAME [regina.vox]`: The voxelized geometry file, which is a geometry model in which the object to be simulated is described in terms of voxels is here introduced. The geometry model described in this file was the female reference computational phantom [62];

  - `TRANSPARENT QUADRIC MAT [56]`: The material index of which the transparent body is made of, as described in 3.1.2.1 **Geometry Data File**, is specified;

  - `GRANULARITY TO SCAN VOXELS [10]`: The computation of the masses of the voxels that may not be immersed within the `TRANSPARENT QUADRIC MATERIAL` is done by integrating the mass density over the voxel volume. By controlling the `GRANULARITY` the accuracy for which this integration is calculated can be set. A reasonably low value, recommended by the author is `[10]`.

- `[SECTION PENELOPE v.2009-10-01]`: In this section, all the materials used in the simulated geometry are listed as well as the cutoff energies for each material.

  - `MAT#`: The material's index are listed in ascending order and this index is the same as they were established in the voxelized geometry file;

  - `FILE____(max 20 char)`: The files for each material are listed according to their index;

  - `EABS(e-)`: All particles are transported until their kinetic energies fall below the absorption energy: EABS. This entry refers to that "limit"energy for electron particles;

  - `EABS(ph)`: This entry refers to the "limit"energy for photon particles;

  - `EABS(e+)`: This entry refers to the "limit"energy for positron particles;

  - `C1`: This parameter controls the cutoff energy for elastic collisions, for C1 is the average angular deflection due to all elastic collisions occurring along a given path length ($C_1 \simeq 1 - (\cos\theta_c)$, where θ_c is the cutoff angle). Therefore, it determines the mean free path between elastic interactions. C1 can assume values from 0 up to 0.2, being this the maximum value permitted;

  - `C2`: This parameter also influences the cutoff energy for elastic collisions for it establishes the maximum average fractional energy loss in a single step length;
  - `WCC`: This is the cutoff energy for inelastic interactions;
  - `WCR`: This is the cutoff energy for bremsstrahlung interactions;
  - `DSMAX`: This parameter defines the maximum step length for electrons and positrons, for photons it doesn't have effect. The step length is the distance traveled by a particle during the simulation.

- `[SECTION TALLY ENERGY DEPOSITION v.2012-06-01]`: This tally produces an output file in which the energy deposited per simulated history in each material is reported (tallyEnergyDeposition.dat).

  - `STATUS [ON]`: To activate this tally;
  - `DETECTION MATERIAL [57]`: The material of the detector, as described in 3.1.2.1 **Geometry Data File**, is specified;
  - `RELATIVE UNCERTAINTY [1.0]`: This uncertainty, which is specified in % is used as a criterion to decide to stop the simulation. This uncertainty, used to compute simulation efficiency, only refers to the detection material.

- `[SECTION TALLY PIXELATED IMAGING DETECTOR v.2015-02-06]`: As a result of the radiation reaching the detector, a pixelated image is developed. In this section the characteristics of the detector body are specified.

  - `STATUS [ON]`: To activate this tally;
  - `DETECTION MATERIAL [57]`: The detector is identified as the body or module that is made of the material introduced in the field `DETECTION MATERIAL` of the configuration file;
  - `FILTER PHOTON INTERACTION [-1]`: Photons arriving at the detector can be filtered according to the interactions they have suffered, for the entry `[-1]`, only unscattered photons are considered;
  - `X-PIXEL SIZE [0 600]`: This entry specifies the number of pixels along the x axis;
  - `Y-PIXEL SIZE [0 500]`: This entry specifies the number of pixels along the y axis;
  - `DETECTION MODE [1]`: This entry specifies the detection mode. In order to establish that the image will be a result of the energy deposited per unit pixel area and per simulated history, this must be set in energy integrating mode, which corresponds to `[1]`;
  - `ENERGY DEPOSITION THRESHOLD [1.0e3]`: This entry only applies if the entry `FILTER PHOTON INTERACTION` was set to mode `[2]`, which is not the case, and therefore it is ignored for other cases;

- `EMIN, EMAX, No. OF E BINS [0.0e0 1.0e9 100]`: This entry only applies if the entry `FILTER PHOTON INTERACTION` was set to mode `[3]`, which is not the case, and therefore it is ignored;
- `ENERGY RESOLUTION [0.0 0.0]`: This entry only applies to the case in which the `SUBSECTION FOR PARTICLE ENERGY` was set to simulate a Gaussian energy spectrum with `FWHM[eV]=sqrt(A+B*E[eV])`, which is not the case and therefore it is ignored;
- `REPORT FORMAT [2]`: The report format is set in this entry. For a matrix format report the entry is set to `[2]` and an output file containing the image signal for each pixel is written in plain text (tallyPixelImageDetectEI-matrix.dat);
- `RELATIVE UNCERTAINTY [1.0]`: This uncertainty, which is specified in % is used as a criterion to decide to stop the simulation.

Appendix C

PenEasy files for the PMMA Monte Carlo Simulations

The geometry and configuration files required to perform the simulations of the PMMA phantom model are listed in the following sections. However it's important to refer that the following sections only describe one case scenario, which is for a PMMA phantom with the ionization chamber positioned in the probe hole located at 180° . However all five case scenarios where simulated, in which the ionization chamber assumes 0° 90° 180° 270° and center position within the probe holes and each one was simulated for a source position of 0° 90° 180° and 270° .

C.1 The geometry file: PMMA.geo File

```
XXXXXXXXXXXXXXXXXXXXXXXXXXXXXXXXXXXXXXXXXXXXXXXXXXXXXXXXXXXXXXXXXXXXXXX
geometry
0000000000000000000000000000000000000000000000000000000000000000000000000
SURFACE ( 1) Plane Z=0.0
INDICES=( 0, 0, 0, 1, 0)
Z-SHIFT=(+0.000000000000000E+00, 0)
0000000000000000000000000000000000000000000000000000000000000000000000000
SURFACE ( 2) Plane Z=15.0
INDICES=( 0, 0, 0, 1, 0)
Z-SHIFT=(+1.500000000000000E+01, 0)
0000000000000000000000000000000000000000000000000000000000000000000000000
SURFACE ( 3) Cylinder probe hole R=0.655
INDICES=( 1, 1, 0, 0,-1)
X-SCALE=(+0.655000000000000E+00, 0)
```

```
Y-SCALE=(+0.655000000000000E+00, 0)
0000000000000000000000000000000000000000000000000000000000000000000000
BODY ( 1) Cylinder CENTER probe hole R=0.655
MATERIAL( 6)
SURFACE ( 1), SIDE POINTER=( 1)
SURFACE ( 2), SIDE POINTER=(-1)
SURFACE ( 3), SIDE POINTER=(-1)
0000000000000000000000000000000000000000000000000000000000000000000000
MODULE ( 2) 270° Cylinder side probe hole R=0.655
MATERIAL( 6)
SURFACE ( 1), SIDE POINTER=( 1)
SURFACE ( 2), SIDE POINTER=(-1)
SURFACE ( 3), SIDE POINTER=(-1)
1111111111111111111111111111111111111111111111111111111111111111111111
OMEGA=(+0.000000000000000E+00, 0) DEG
THETA=(+0.000000000000000E+00, 0) DEG
PHI=(+0.000000000000000E+00, 0) DEG
X-SHIFT=(+1.500000000000000E+01, 0) (DEFAULT=0.0)
Y-SHIFT=(+0.000000000000000E+00, 0) (DEFAULT=0.0)
Z-SHIFT=(+0.000000000000000E+00, 0) (DEFAULT=0.0)
0000000000000000000000000000000000000000000000000000000000000000000000
CLONE ( 3) 0° Cylinder side probe hole R=0.655
MODULE ( 2) ORIGINAL MODULE
1111111111111111111111111111111111111111111111111111111111111111111111
OMEGA=(-9.000000000000000E+01, 0) DEG (DEFAULT=0.0)
THETA=(+0.000000000000000E+00, 0) DEG (DEFAULT=0.0)
PHI=(+0.000000000000000E+00, 0) DEG (DEFAULT=0.0)
X-SHIFT=(+0.000000000000000E+00, 0) (DEFAULT=0.0)
Y-SHIFT=(+0.000000000000000E+00, 0) (DEFAULT=0.0)
Z-SHIFT=(+0.000000000000000E+00, 0) (DEFAULT=0.0)
0000000000000000000000000000000000000000000000000000000000000000000000
CLONE ( 4) 90° Cylinder side probe hole R=0.655
MODULE ( 2) ORIGINAL MODULE
1111111111111111111111111111111111111111111111111111111111111111111111
OMEGA=(-1.800000000000000E+02, 0) DEG (DEFAULT=0.0)
THETA=(+0.000000000000000E+00, 0) DEG (DEFAULT=0.0)
PHI=(+0.000000000000000E+00, 0) DEG (DEFAULT=0.0)
X-SHIFT=(+0.000000000000000E+00, 0) (DEFAULT=0.0)
Y-SHIFT=(+0.000000000000000E+00, 0) (DEFAULT=0.0)
Z-SHIFT=(+0.000000000000000E+00, 0) (DEFAULT=0.0)
0000000000000000000000000000000000000000000000000000000000000000000000
```

```
SURFACE ( 14) Cylinder R=0,025 ALUMINUM CHAMBER
INDICES=( 1, 1, 0, 0,-1)
X-SCALE=(+0.025000000000000E+00, 0)
Y-SCALE=(+0.025000000000000E+00, 0)
0000000000000000000000000000000000000000000000000000000000000000
SURFACE ( 15) Plane Z=2.5 FOR ALUMINUM AND AIR CHAMBERS
INDICES=( 0, 0, 0, 1, 0)
Z-SHIFT=(+2.500000000000000E+00, 0)
0000000000000000000000000000000000000000000000000000000000000000
SURFACE ( 16) Plane Z=12.5 FOR ALUMINUM AND AIR CHAMBERS
INDICES=( 0, 0, 0, 1, 0)
Z-SHIFT=(+1.250000000000000E+01, 0)
0000000000000000000000000000000000000000000000000000000000000000
BODY ( 5) CYLINDER ALUMINUM CHAMBER
MATERIAL( 3)
SURFACE ( 14), SIDE POINTER=(-1)
SURFACE ( 15), SIDE POINTER=( 1)
SURFACE ( 16), SIDE POINTER=(-1)
0000000000000000000000000000000000000000000000000000000000000000
SURFACE ( 17) Cylinder R=0,15 AIR CHAMBER
INDICES=( 1, 1, 0, 0,-1)
X-SCALE=(+0.150000000000000E+00, 0)
Y-SCALE=(+0.150000000000000E+00, 0)
0000000000000000000000000000000000000000000000000000000000000000
BODY ( 6) CYLINDER AIR CHAMBER
MATERIAL( 2)
SURFACE ( 17), SIDE POINTER=(-1)
SURFACE ( 15), SIDE POINTER=( 1)
SURFACE ( 16), SIDE POINTER=(-1)
BODY ( 5)
0000000000000000000000000000000000000000000000000000000000000000
SURFACE ( 18) Cylinder R=0,1875 FIBER CARBON CHAMBER
INDICES=( 1, 1, 0, 0,-1)
X-SCALE=(+0.187500000000000E+00, 0)
Y-SCALE=(+0.187500000000000E+00, 0)
0000000000000000000000000000000000000000000000000000000000000000
BODY ( 7) CYLINDER FIBER CARBON CHAMBER
MATERIAL( 5)
SURFACE ( 18), SIDE POINTER=(-1)
SURFACE ( 1), SIDE POINTER=( 1)
SURFACE ( 2), SIDE POINTER=(-1)
```

```
BODY ( 5)
BODY ( 6)
00000000000000000000000000000000000000000000000000000000000000000000
SURFACE ( 19) Cylinder R=0,3125 PMMA ADAPTOR
INDICES=( 1, 1, 0, 0,-1)
X-SCALE=(+0.312500000000000E+00, 0)
Y-SCALE=(+0.312500000000000E+00, 0)
00000000000000000000000000000000000000000000000000000000000000000000
MODULE ( 8) CYLINDER PMMA ADAPTOR 180° side probe hole
MATERIAL( 7)
SURFACE ( 19), SIDE POINTER=(-1)
SURFACE ( 1), SIDE POINTER=( 1)
SURFACE ( 2), SIDE POINTER=(-1)
BODY ( 5)
BODY ( 6)
BODY ( 7)
11111111111111111111111111111111111111111111111111111111111111111111
OMEGA=(+0.000000000000000E+00, 0) DEG
THETA=(+0.000000000000000E+00, 0) DEG
PHI=(+0.000000000000000E+00, 0) DEG
X-SHIFT=(+0.000000000000000E+00, 0) (DEFAULT=0.0)
Y-SHIFT=(+1.500000000000000E+01, 0) (DEFAULT=0.0)
Z-SHIFT=(+0.000000000000000E+00, 0) (DEFAULT=0.0)
00000000000000000000000000000000000000000000000000000000000000000000
SURFACE ( 13) Cylinder R=16 PHANTOM CILINDER
INDICES=( 1, 1, 0, 0,-1)
X-SCALE=(+1.600000000000000E+01, 0)
Y-SCALE=(+1.600000000000000E+01, 0)
00000000000000000000000000000000000000000000000000000000000000000000
MODULE ( 9) PHANTOM CYLINDER
MATERIAL( 4)
SURFACE ( 13), SIDE POINTER=(-1)
SURFACE ( 1), SIDE POINTER=( 1)
SURFACE ( 2), SIDE POINTER=(-1)
BODY ( 1)
MODULE ( 2)
MODULE ( 3)
MODULE ( 4)
MODULE ( 8)
11111111111111111111111111111111111111111111111111111111111111111111
OMEGA=(+0.000000000000000E+00, 0) DEG
```

```
THETA=(+0.000000000000000E+00, 0) DEG
PHI=(+0.000000000000000E+00, 0) DEG
X-SHIFT=(+0.000000000000000E+00, 0) (DEFAULT=0.0)
Y-SHIFT=(+0.000000000000000E+00, 0) (DEFAULT=0.0)
Z-SHIFT=(+1.325000000000000E+02, 0) (DEFAULT=0.0)
0000000000000000000000000000000000000000000000000000000000000000
SURFACE ( 20) Plane X=-25.75
INDICES=( 0, 0, 0, 0, 0)
AX=(+1.000000000000000E+00, 0)
A0=(+2.575000000000000E+01, 0)
0000000000000000000000000000000000000000000000000000000000000000
SURFACE ( 21) Plane X=25.75 largura 51.5cm
INDICES=( 0, 0, 0, 0, 0)
AX=(+1.000000000000000E+00, 0)
A0=(-2.575000000000000E+01, 0)
0000000000000000000000000000000000000000000000000000000000000000
SURFACE ( 24) Plane Y=16.0
INDICES=( 0, 0, 0, 0, 0)
AY=(+1.000000000000000E+00, 0)
A0=(-1.600000000000000E+01, 0)
0000000000000000000000000000000000000000000000000000000000000000
SURFACE ( 25) Plane Y=18.5 espessura 2.5cm
INDICES=( 0, 0, 0, 0, 0)
AY=(+1.000000000000000E+00, 0)
A0=(-1.850000000000000E+01, 0)
0000000000000000000000000000000000000000000000000000000000000000
SURFACE ( 22) Plane Z=0.0
INDICES=( 0, 0, 0, 1, 0)
Z-SHIFT=(+0.000000000000000E+00, 0)
0000000000000000000000000000000000000000000000000000000000000000
SURFACE ( 23) Plane Z=187.5 altura 40cm acima do PMMA
INDICES=( 0, 0, 0, 1, 0)
Z-SHIFT=(+1.875000000000000E+02, 0)
0000000000000000000000000000000000000000000000000000000000000000
BODY ( 10) Patient Table
MATERIAL( 9)
SURFACE ( 20), SIDE POINTER=( 1)
SURFACE ( 21), SIDE POINTER=(-1)
SURFACE ( 22), SIDE POINTER=( 1)
SURFACE ( 23), SIDE POINTER=(-1)
SURFACE ( 24), SIDE POINTER=( 1)
```

```
SURFACE ( 25), SIDE POINTER=(-1)
0000000000000000000000000000000000000000000000000000000000000000000000
SURFACE ( 26) Sphere R=450
INDICES=( 1, 1, 1, 0,-1)
X-SCALE=(+4.500000000000000E+02, 0)
Y-SCALE=(+4.500000000000000E+02, 0)
Z-SCALE=(+4.500000000000000E+02, 0)
X-SHIFT=(+0.000000000000000E+00, 0)
Y-SHIFT=(+0.000000000000000E+00, 0)
Z-SHIFT=(+1.325000000000000E+02, 0)
0000000000000000000000000000000000000000000000000000000000000000000000
MODULE ( 11) esfera envolvente
MATERIAL( 1) Material transparente
SURFACE ( 26), SIDE POINTER=(-1)
MODULE ( 9)
BODY ( 10)
0000000000000000000000000000000000000000000000000000000000000000000000
END
0000000000000000000000000000000000000000000000000000000000000000000000
```

C.2 The configuration file: PMMA.in File

```
# »» CONFIG FILE FOR penEasy »»»»»»»»»»»»»»»»»»»»»»
#
# CASE DESCRIPTION:
# Sample config file adapted to the example described in the READM
# file. Before editing this file, read carefully the instructions
# provided here after the data sections and in the README file.
#
# LAST UPDATE:
# 2015-05-26 by JS

# »»»»»»»»»»»»»»»»»»»»»»»»»»»»»»»»»»»»»»»»»»»»»»»»>
# GENERAL INSTRUCTIONS
#
# * Lines starting with a '#' (in column 1) and blank lines are
#   comments. Comments are NOT allowed inside data sections.
#
# * Do not change the order in which sections appear, neither the
#   order of data fields in each section.
#
# * Each data section has a version number of the form yyyy-mm-dd that is
#   written in the corresponding section title. Should an incorrect
#   version be introduced an error message would be issued and the
#   execution halted.
#
# * Character strings (e.g. file names) are introduced in free-format
#   style, that is, leading and trailing blanks are allowed. Their
#   maximum extension (except when noted) is 80 characters and they must
#   not contain blanks. Thus, for instance, 'stainless steel' should be
#   introduced as 'stainlessSteel' or 'stainless_Steel'.
#
# * Most syntax errors can be easily identified by looking for error
#   messages or inconsistencies within the last lines of penEasy output.
```

```
#   It is always a good idea to check the output to make sure that the
#   information written after processing each section coincides with what
#   is expected from the input.

# »»»»»»»»»»»»»»»»»»»»»»»»»»»»»»»»»>
# INSTRUCTIONS FOR SECTION CONFIG
#
# * Details on the simulation configuration are provided with their
#   documentation (see   /documentation/*).
[SECTION CONFIG v.2013-03-18]
1.0e11           NUMBER OF HISTORIES (1.0e15 MAX)
1.0e30           ALLOTTED TIME (s) (+ FOR REAL TIME; - FOR CPU TIME)
100.0            UPDATE INTERVAL (s)
1 1              INITIAL RANDOM SEEDS
-                SEEDS FILE; MUST ENTER SEEDS=0,0 TO APPLY
-                RESTART FILE; MUST ENTER SEEDS=-1,-1 TO APPLY
penEasy.dmp      OUTPUT DUMP FILE; ENTER '-' FOR 'NO DUMP'
1800.0           INTERVAL BETWEEN DUMPS (s)
[END OF CONFIG SECTION]

# »»»»»»»»»»»»»»»»»»»»»»»»»»»»»»»»»>
# INSTRUCTIONS FOR SOURCE SECTIONS
#
# * Details on the features and configuration of each source model
#    are provided with their documentation (see  /documentation/*).
#    Notice that there must be one and only one active (status ON) source model.

[SECTION SOURCE BOX ISOTROPIC GAUSS SPECTRUM v.2014-12-21]
ON                        STATUS (ON or OFF)
2                         PARTICLE TYPE (1=ELECTRON, 2=PHOTON, 3=POSITRON)
  SUBSECTION FOR PHOTON POLARIZATION:
0                         ACTIVATE PHOTON POLARIZATION PHYSICS (0=NO, 1=YES)
0.0 0.0 0.0               STOKES PARAMETERS (UNUSED IF ACTIVATE POLARIZATION=0)
  SUBSECTION FOR PARTICLE POSITION:
0.0 -100.0 140.0          COORDINATES (cm) OF BOX CENTER
0.0 0.0 0.0               BOX SIDES (cm)
0.0 0.0                   FWHMs (cm) OF GAUSSIAN X,Y DISTRIBUTIONS
0.0 0.0 0.0               EULER ANGLES [OMEGA,THETA,PHI](deg) FOR BOX ROTATION Rz(PHI).Ry(THETA).Rz(OMEGA).r
0.0 0.0 0.0               TRANSLATION [DX,DY,DZ](cm) OF BOX CENTER POSITION
0                         SOURCE MATERIAL (0=DON'T CARE, >0 FOR LOCAL SOURCE, <0 FOR IN-FIELD BEAM)
  SUBSECTION FOR PARTICLE DIRECTION:
0.0 1.0 0.0               DIRECTION VECTOR; NO NEED TO NORMALIZE
0.0 25.0                  DIRECTION POLAR ANGLE INTERVAL [THETA0,THETA1], BOTH VALUES IN [0,180]deg
0.0 360.0                 DIRECTION AZIMUTHAL ANGLE INTERVAL PHI0 IN [0,360)deg AND DeltaPHI IN [0,360]deg
1                         APPLY ALSO TO DIRECTION THE ROTATION USED FOR BOX POSITION (0=NO, 1=YES)
  SUBSECTION FOR PARTICLE ENERGY:
-                         ENERGY SPECTRUM FILE NAME; ENTER '-' TO ENTER SPECTRUM IN NEXT LINES
Energy(eV)  Probability   DUMMY SPECTRUM HEADER LINE; REMOVE HEADER AND TABLE IF A FILENAME WAS PROVIDED ABOVE
8000        0             Spectrum table, arbitrary normalization. Example: a single channel [10,10]MeV of null width
9000        1.34227E-36
10000       2.28433E-25
11000 6.89591E-19
12000 8.3039E-14
13000 8.8427E-10
14000 1.91415E-06
15000 0.000778841
16000 0.03852808
17000 0.934731394
18000 12.13670435
19000 108.3011025
20000 692.531851
21000 2260.488039
22000 6561.372175
23000 17018.29289
24000 38939.4887
25000 81220.44065
26000 154223.7205
27000 274039.4898
28000 454350.0718
```

```
29000 716382.9809
30000 1058982.621
31000 1359330.239
32000 1699784.282
33000 2093194.47
34000 2512223.254
35000 2968494.282
36000 3444823.374
37000 3948715.492
38000 4472095.401
39000 5017415.915
40000 5539890.795
41000 5891288.377
42000 6235118.772
43000 6578710.086
44000 6884225.493
45000 7164548.614
46000 7472123.42
47000 7766766.878
48000 7958485.892
49000 8125492.12
50000 8308542.657
51000 8372289.905
52000 8425786.993
53000 8461419.901
54000 8543654.011
55000 8613291.755
56000 12173343.33
57000 15908734.19
58000 19258914.43
59000 22729261.5
60000 16414349.83
61000 9699382.211
62000 8845960.556
63000 7958150.465
64000 7821509.33
65000 7655078.503
66000 10245564.93
67000 12896733.38
68000 10636236.06
69000 8261894.173
70000 7015023.413
71000 5742050.876
72000 5531892.281
73000 5294817.428
74000 5266129.026
75000 5248216.672
76000 5143328.728
77000 5012530.809
78000 4939013.348
79000 4798301.143
80000 4718945.82
81000 4547868.521
82000 4529644.827
83000 4380397.959
84000 4245040.101
85000 4107028.71
86000 4034981.867
87000 3963955.132
88000 3823975.782
89000 3681170.502
90000 3578054.703
91000 3470911.323
92000 3351214.843
93000 3218706.557
94000 3108181.918
95000 2997206.772
96000 2901696.742
97000 2806421.334
```

```
98000 2709297.284
99000 2611071.498
100000 2506389.851
101000 2393398.573
102000 2299818.589
103000 2184873.179
104000 2071647.056
105000 1960432.606
106000 1836564.472
107000 1714468.483
108000 1612392.196
109000 1503783.106
110000 1380892.15
111000 1258504
112000 1203315.836
113000 1145890.969
114000 1022679.082
115000 885779.0168
116000 806045.2228
117000 727642.879
118000 638215.3136
119000 538945.5547
120000 458960.8035
121000 349783.7282
122000 240573.1158
123000 166316.9318
124000 79589.65114
125000 7742.149526
126000      -1.0         Enter a negative prob. to signal the end of the table
0.0                      FWHM(eV) OF GAUSSIAN ENERGY DISTRIB. [NOTE FWHM=SIGMA*sqrt(8*ln(2))]
[END OF BIGS SECTION]

[SECTION SOURCE PHASE SPACE FILE v.2009-06-15]
OFF             STATUS (ON or OFF)
0               PSF FORMAT (0=STANDARD penEasy ASCII, 1=IAEA BINARY)
particles.psf   PSF FILENAME, REMOVE EXTENSION IF PSF FORMAT=1
1               SPLITTING FACTOR
0.0 0.0 0.0     EULER ANGLES [Rz,Ry,Rz](deg) TO ROTATE POSITION AND DIRECTION
0.0 0.0 0.0     TRANSLATION [DX,DY,DZ](cm) OF POSITION
1               VALIDATE BEFORE SIMULATION (1=YES, MAY TAKE A WHILE; 0=NO)
0.000e0         MAX PSF ENERGY (eV) (UNUSED IF VALIDATE=1 OR IAEA FORMAT; ADD 1023 keV FOR e+)
[END OF SPSF SECTION]

# »»»»»»»»»»»»»»»»»»»»»»»»»»»»»»»»»>
# INSTRUCTIONS FOR SECTION PENGEOM+PENVOX
#
# * Enter either: (i) a file name in the QUADRICS FILE field and a dash '-' in
#   the VOXELS FILE field if you want to define only a quadric geometry model;
#   (ii) a file name in the VOXELS FILE field and a dash '-' in the QUADRICS
#   FILE field if you want to define only a voxelized geometry model; or (iii)
#   both a quadrics and a voxelized file names in the corresponding fields if
#   you want to define a combination of overlapping quadrics and voxelized models.
#
# * The TRANSPARENT QUADRIC MAT and GRANULARITY field are used only if both a
#   quadric and a voxel geometries are defined. Otherwise they are irrelevant.
#
# * Details on the use and configuration of these geometry models are provided
#   in the documentation (please refer to ~/documentation/*).

[SECTION PENGEOM+PENVOX v.2009-06-15]
phantom180position.geo            QUADRICS FILE NAME, USE '-' IF NONE
-           VOXELS FILE NAME, USE '-' IF NONE
-           TRANSPARENT QUADRIC MAT (USED ONLY IF QUAD&VOX)
10          GRANULARITY TO SCAN VOXELS (USED ONLY IF QUAD&VOX)
[END OF GEO SECTION]

# »»»»»»»»»»»»»»»»»»»»»»»»»»»»»»»»»>
# INSTRUCTIONS FOR SECTION PENELOPE
#
```

```
# * Write one line of data per defined material. Each line starts with
#   the material index (MAT#), which should be an integer starting from 1.
#   Set MAT# to zero in the last line to denote the end of the list.
#
# * Use 20 characters at most to introduce the material data file name.
#   Blanks or special characters are not allowed in file names. Thus,
#   instead of "stainless steel.mat"use "stainlessSteel.mat".
#
# * If, for a certain material, the transport parameters after the file
#   name are left empty, then they are set automatically as follows:
#    -Eabs for charged particles are set to 1% of the
#    initial source energy (E), with the limiting values of 50 eV
#    (min) and 1 MeV (max).
#    -Eabs for photons is set to 0.1% E with the limiting values of
#    50 eV and 1 MeV.
#    -C1 and C2 are both set to 0.1.
#    -WCC is set to min(Eabs(e-),1% E).
#    -WCR is set to min(Eabs(phot),0.1% E).
#    -DSMAX is set to infinity.
#
# * Do not remove the line containing the table header "MAT# FILE...".

[SECTION PENELOPE v.2009-10-01]
MAT# FILE___(max 20 char) EABS(e-) EABS(ph) EABS(e+) C1   C2  WCC  WCR  DSMAX  COMMENTS
 1   Airtransp.mat            8e4      5e3      8e4     0.2  0.2  4e3  4e3 1.0e30
 2   Airchamber.mat           8e4      5e3      8e4     0.2  0.2  4e3  4e3 1.0e30
 3   AirAluminum.mat          8e4      5e3      8e4     0.2  0.2  4e3  4e3 1.0e30
 4   PMMA.mat                 8e4      5e3      8e4     0.2  0.2  5e3  4e3 1.0e30
 5   AirCarbFiber.mat         8e4      5e3      8e4     0.2  0.2  4e3  4e3 1.0e30
 6   PMMAchamber2.mat         8e4      5e3      8e4     0.2  0.2  4e3  4e3 1.0e30
 7   PMMAadaptor.mat          8e4      5e3      8e4     0.2  0.2  4e3  4e3 1.0e30
 8   Se.mat                   3e9      3e9      3e9     0.2  0.2  5e3  1e4 1.0e30
 9   Teflon.mat               8e4      5e3      8e4     0.2  0.2  4e3  4e3 1.0e30
10   Airprobehole.mat         8e4      5e3      8e4     0.2  0.2  4e3  4e3 1.0e30
0
[END OF PEN SECTION]

# »»»»»»»»»»»»»»»»»»»»»»»»»»»»»»»»»>
# INSTRUCTIONS FOR THE TALLY SECTIONS
#
# * Details on the features and configuration of each tally are provided
#   with their documentation (see  /documentation/*.txt).
#
# * The required RELATIVE UNCERTAINTY that is specified for each tally
#   (except for those that do not have an associated uncertainty, e.g.
#   a phase-space file) is used as a condition to stop the simulation. Only
#   when the requested relative uncertainties of *all* the tallies have
#   been attained the uncertainty condition is considered fulfilled.
#   Recall that the simulation can also be halted because the allotted
#   time or the number of histories requested have been reached. Setting
#   the RELATIVE UNCERTAINTY of all tallies to zero will prevent the
#   execution from stopping for this cause.
#
# * Note for advanced users: when a certain tally scores nothing (i.e.
#   zero) the corresponding REPORT routine reports 0% uncertainty but, at
#   the same time, it reports that the requested uncertainty has not been
#   reached, irrespective of the value introduced in the config file.
#   This is to prevent the simulation from being stopped by a deceptive
#   impression of accuracy in highly inefficient simulations, where the
#   score and its standard deviation after a short period of time can be
#   null.

[SECTION TALLY VOXEL DOSE v.2014-12-27]
OFF              STATUS (ON or OFF)
0  0             ROI MIN,MAX X-INDEX (0 0 FOR ALL VOXELS)
0  0             ROI MIN,MAX Y-INDEX (0 0 FOR ALL VOXELS)
0  0             ROI MIN,MAX Z-INDEX (0 0 FOR ALL VOXELS)
0                PRINT VOXELS MASS IN REPORT (1=YES,0=NO)
1                PRINT COORDINATES IN REPORT (1=YES,0=NO,-1=NO&BINARYFORMAT)
```

```
0.0             RELATIVE UNCERTAINTY (%) REQUESTED
[END OF VDD SECTION]

[SECTION TALLY SPATIAL DOSE DISTRIB v.2009-06-15]
OFF             STATUS (ON or OFF)
0.0  0.0  0     XMIN,XMAX(cm),NXBIN (0 FOR DX=infty)
0.0  0.0  0     YMIN,YMAX(cm),NYBIN (0 FOR DY=infty)
0.0  7.0  40    ZMIN,ZMAX(cm),NZBIN (0 FOR DZ=infty)
1               PRINT COORDINATES IN REPORT (1=YES,0=NO,-1=NO&BINARYFORMAT)
1.0             RELATIVE UNCERTAINTY (%) REQUESTED
[END OF SDD SECTION]

[SECTION TALLY CYLINDRICAL DOSE DISTRIB v.2009-06-15]
OFF             STATUS (ON or OFF)
0.0  8.0  80    RMIN,RMAX(cm),NRBIN (>0)
0.0  7.0  40    ZMIN,ZMAX(cm),NZBIN (0 FOR DZ=infty)
1               PRINT COORDINATES IN REPORT (1=YES,0=NO)
0.0             RELATIVE UNCERTAINTY (%) REQUESTED
[END OF CDD SECTION]

[SECTION TALLY SPHERICAL DOSE DISTRIB v.2009-06-15]
OFF             STATUS (ON or OFF)
0.0  1.0  50    RMIN,RMAX(cm),NRBIN (>0)
1               PRINT COORDINATES IN REPORT (1=YES,0=NO)
0.0             RELATIVE UNCERTAINTY (%) REQUESTED
[END OF SPD SECTION]

[SECTION TALLY ENERGY DEPOSITION v.2012-06-01]
ON              STATUS (ON or OFF)
2               DETECTION MATERIAL
1.0             RELATIVE UNCERTAINTY (%) REQUESTED
[END OF EDP SECTION]

[SECTION TALLY PULSE HEIGHT SPECTRUM v.2012-06-01]
OFF             STATUS (ON or OFF)
1               DETECTION MATERIAL
0.0  1.0e9  100  EMIN,EMAX(eV), No. OF E BINS
0.0  0.0        A(eV$\hat{2}$),B(eV) FOR GAUSSIAN CONVOLUTION FWHM[eV] sqrt(A+B*E[eV])
0.0             RELATIVE UNCERTAINTY (%) REQUESTED
[END OF PHS SECTION]

[SECTION TALLY PIXELATED IMAGING DETECTOR v.2015-02-06]
OFF       STATUS (ON or OFF)
57        DETECTION MATERIAL
-1        FILTER PHOTON INTERACTION (0=NOFILTER, -1=UNSCATTERED, 1=RAYLEIGH, 2=COMPTON, 3=SECONDARIES, 9=MULTISCATTERED)
0  600    X-PIXEL SIZE(cm), No. X-PIXELS (ENTER 0 IN EITHER FIELD FOR AUTO)
0  500    Y-PIXEL SIZE(cm), No. Y-PIXELS (ENTER 0 IN EITHER FIELD FOR AUTO)
1         DETECTION MODE (1=ENERGY INTEGRATING, 2=PHOTON COUNTING, 3=PHOTON ENERGY DISCRIMINATING aka SPECTRUM)
1.0e3           ENERGY DEPOSITION THRESHOLD (eV) FOR MODE=2 (IGNORED FOR OTHER MODES)
0.0e0 1.0e9 100 EMIN,EMAX(eV), No. OF E BINS FOR MODE=3 (IGNORED FOR OTHER MODES)
0.0  0.0        ENERGY RESOLUTION, ENTER A(eV$\hat{2}$),B(eV) FOR A GAUSSIAN WITH FWHM[eV]=sqrt(A+B*E[eV])
2               REPORT FORMAT (1=COLUMNAR, 2=MATRIX, 3=BINARY)
1.0             RELATIVE UNCERTAINTY (%) REQUESTED
[END OF PID SECTION]

[SECTION TALLY FLUENCE TRACK LENGTH v.2012-06-01]
OFF             STATUS (ON or OFF)
1               DETECTION MATERIAL
1.0e2 1.0e9 70 LOGEMIN,EMAX(eV), No. OF E BINS, APPEND 'LOG' FOR A LOG SCALE
0.0             RELATIVE UNCERTAINTY (%) REQUESTED
[END OF FTL SECTION]

[SECTION TALLY PHASE SPACE FILE v.2009-06-15]
OFF             STATUS (ON or OFF)
0               PSF FORMAT (0=STANDARD penEasy ASCII, 1=IAEA BINARY)
1               DETECTION MATERIAL (MUST BE A PERFECT ABSORBENT, EABS=+infty)
output.psf      PSF FILENAME, REMOVE EXTENSION IF FORMAT=1
[END OF PSF SECTION]
```

```
[SECTION TALLY PARTICLE CURRENT SPECTRUM v.2009-06-15]
OFF              STATUS (ON or OFF)
1                DETECTION MATERIAL
0.0  1.0e9  100  EMIN,EMAX(eV), No. OF E BINS
0.0              RELATIVE UNCERTAINTY (%) REQUESTED
[END OF PCS SECTION]

[SECTION TALLY PARTICLE TRACK STRUCTURE v.2009-06-15]
OFF              STATUS (ON or OFF)
100              NUMBER OF HISTORIES TO DISPLAY (1̃00 RECOMMENDED)
[END OF PTS SECTION]

# »»»»»»»»»»»»»»»»»»»»»»»»»»»»»»»»»»»»»»>
# INSTRUCTIONS FOR VARIANCE-REDUCTION SECTIONS
#
# * Details on the features and configuration of each VR technique are provided
#   with their documentation (see /̃documentation/*.txt).

[SECTION INTERACTION FORCING v.2009-06-15]
OFF                         STATUS (ON or OFF)
1.0                         DON’T APPLY BELOW THIS STATISTICAL WEIGHT
MAT   KPAR  ICOL   FORCING (SET MAT=-1 TO END LIST)
-1    0     0      1.0
[END OF VRIF SECTION]

[SECTION SPLITTING v.2015-05-30] |
OFF              STATUS (ON or OFF)
1.0              WGHTMIN, DO NOT SPLIT BELOW THIS STATISTICAL WEIGHT
1                SPLITTING MATERIAL
1                SPLITTING MODE (1=SIMPLE; 2=ROTATIONAL; 3=XY)
1                SPLITTING FACTOR, IGNORED FOR MODE=3
0.0  0.0  0.0    EULER ANGLES [Rz,Ry,Rz](deg), IGNORED FOR MODE=1
0.0  0.0  0.0    SHIFT (cm), IGNORED FOR MODE=1
0                SIGN OF W (’+’, ’-’ OR ’0’=BOTH), IGNORED FOR MODE=1
0.0  360.0       AZIMUTHAL INTERVAL PHI0 IN [0,360)deg AND DeltaPHI IN (0,360]deg, USED ONLY IF MODE=2
[END OF VRS SECTION]

[SECTION RUSSIAN ROULETTE v.2009-06-15]
OFF              STATUS (ON or OFF)
1.0              WGHTMAX, DO NOT PLAY ABOVE THIS STATISTICAL WEIGHT
1                RUSSIAN ROULETTE MATERIAL
1.0              SURVIVAL PROBABILITY

[END OF VRRR SECTION]

# »» END OF FILE »»»»»»»»»»»»»»»»»»»»»»»»»»»»»
```

Appendix D

Code system used in the Image Reconstruction milestone

D.1 Import data matrix

The code used to import the data matrix from each Pixelated Imaging Detector tallie file for each angle to the MATLAB workspace in listed:

```
Matriz10 = importdata('tallyPixelImageDetectEI-matrix10.txt', ',');
Matriz10(:,1)=[];
TM10 = transpose(Matriz10);
Matriz20 = importdata('tallyPixelImageDetectEI-matrix20.txt', ',');
Matriz20(:,1)=[];
TM20 = transpose(Matriz20);
Matriz30 = importdata('tallyPixelImageDetectEI-matrix30.txt', ',');
Matriz30(:,1)=[];
TM30 = transpose(Matriz30);
Matriz40 = importdata('tallyPixelImageDetectEI-matrix40.txt', ',');
Matriz40(:,1)=[];
TM40 = transpose(Matriz40);
Matriz50 = importdata('tallyPixelImageDetectEI-matrix50.txt', ',');
Matriz50(:,1)=[];
TM50 = transpose(Matriz50);
Matriz60 = importdata('tallyPixelImageDetectEI-matrix60.txt', ',');
Matriz60(:,1)=[];
TM60 = transpose(Matriz60);
Matriz70 = importdata('tallyPixelImageDetectEI-matrix70.txt', ',');
Matriz70(:,1)=[];
```

```
TM70 = transpose(Matriz70);
Matriz80 = importdata('tallyPixelImageDetectEI-matrix80.txt', ',');
Matriz80(:,1)=[];
TM80 = transpose(Matriz80);
Matriz90 = importdata('tallyPixelImageDetectEI-matrix90.txt', ',');
Matriz90(:,1)=[];
TM90 = transpose(Matriz90);
Matriz100 = importdata('tallyPixelImageDetectEI-matrix100.txt', ',');
Matriz100(:,1)=[];
TM100 = transpose(Matriz100);
Matriz110 = importdata('tallyPixelImageDetectEI-matrix110.txt', ',');
Matriz110(:,1)=[];
TM110 = transpose(Matriz110);
Matriz120 = importdata('tallyPixelImageDetectEI-matrix120.txt', ',');
Matriz120(:,1)=[];
TM120 = transpose(Matriz120);
Matriz130 = importdata('tallyPixelImageDetectEI-matrix130.txt', ',');
Matriz130(:,1)=[];
TM130 = transpose(Matriz130);
Matriz140 = importdata('tallyPixelImageDetectEI-matrix140.txt', ',');
Matriz140(:,1)=[];
TM140 = transpose(Matriz140);
Matriz150 = importdata('tallyPixelImageDetectEI-matrix150.txt', ',');
Matriz150(:,1)=[];
TM150 = transpose(Matriz150);
Matriz160 = importdata('tallyPixelImageDetectEI-matrix160.txt', ',');
Matriz160(:,1)=[];
TM160 = transpose(Matriz160);
Matriz170 = importdata('tallyPixelImageDetectEI-matrix170.txt', ',');
Matriz170(:,1)=[];
TM170 = transpose(Matriz170);
Matriz180 = importdata('tallyPixelImageDetectEI-matrix180.txt', ',');
Matriz180(:,1)=[];
TM180 = transpose(Matriz180);
Matriz190 = importdata('tallyPixelImageDetectEI-matrix190.txt', ',');
Matriz190(:,1)=[];
TM190 = transpose(Matriz190);
Matriz200 = importdata('tallyPixelImageDetectEI-matrix200.txt', ',');
Matriz200(:,1)=[];
TM200 = transpose(Matriz200);
Matriz210 = importdata('tallyPixelImageDetectEI-matrix210.txt', ',');
```

```
Matriz210(:,1)=[];
TM210 = transpose(Matriz210);
Matriz220 = importdata('tallyPixelImageDetectEI-matrix220.txt', ',');
Matriz220(:,1)=[];
TM220 = transpose(Matriz220);
Matriz230 = importdata('tallyPixelImageDetectEI-matrix230.txt', ',');
Matriz230(:,1)=[];
TM230 = transpose(Matriz230);
Matriz240 = importdata('tallyPixelImageDetectEI-matrix240.txt', ',');
Matriz240(:,1)=[];
TM240 = transpose(Matriz240);
Matriz250 = importdata('tallyPixelImageDetectEI-matrix250.txt', ',');
Matriz250(:,1)=[];
TM250 = transpose(Matriz250);
Matriz260 = importdata('tallyPixelImageDetectEI-matrix260.txt', ',');
Matriz260(:,1)=[];
TM260 = transpose(Matriz260);
Matriz270 = importdata('tallyPixelImageDetectEI-matrix270.txt', ',');
Matriz270(:,1)=[];
TM270 = transpose(Matriz270);
Matriz280 = importdata('tallyPixelImageDetectEI-matrix280.txt', ',');
Matriz280(:,1)=[];
TM280 = transpose(Matriz280);
Matriz290 = importdata('tallyPixelImageDetectEI-matrix290.txt', ',');
Matriz290(:,1)=[];
TM290 = transpose(Matriz290);
Matriz300 = importdata('tallyPixelImageDetectEI-matrix300.txt', ',');
Matriz300(:,1)=[];
TM300 = transpose(Matriz300);
Matriz310 = importdata('tallyPixelImageDetectEI-matrix310.txt', ',');
Matriz310(:,1)=[];
TM310 = transpose(Matriz310);
Matriz320 = importdata('tallyPixelImageDetectEI-matrix320.txt', ',');
Matriz320(:,1)=[];
TM320 = transpose(Matriz320);
Matriz330 = importdata('tallyPixelImageDetectEI-matrix330.txt', ',');
Matriz330(:,1)=[];
TM330 = transpose(Matriz330);
Matriz340 = importdata('tallyPixelImageDetectEI-matrix340.txt', ',');
Matriz340(:,1)=[];
TM340 = transpose(Matriz340);
```

```
Matriz350 = importdata('tallyPixelImageDetectEI-matrix350.txt', ',');
Matriz350(:,1)=[];
TM350 = transpose(Matriz350);
Matriz360 = importdata('tallyPixelImageDetectEI-matrix360.txt', ',');
Matriz360(:,1)=[];
TM360 = transpose(Matriz360);
```

D.2 Cube data matrix

The code used to load the data matrices into a structure of matrices, resembling a cube is listed below:

```
MATRIZ3D = zeros (600,36,500);
for i= 1:500
Linhai = [TM360(:,i) TM10(:,i) TM20(:,i) TM30(:,i) TM40(:,i)
TM50(:,i) TM60(:,i) TM70(:,i) TM80(:,i) TM90(:,i) TM100(:,i)
TM110(:,i) TM120(:,i) TM130(:,i) TM140(:,i) TM150(:,i)
TM160(:,i) TM170(:,i) TM180(:,i) TM190(:,i) TM200(:,i)
TM210(:,i) TM220(:,i) TM230(:,i) TM240(:,i) TM250(:,i)
TM260(:,i) TM270(:,i) TM280(:,i) TM290(:,i) TM300(:,i)
TM310(:,i) TM320(:,i) TM330(:,i) TM340(:,i) TM350(:,i)];
MATRIZ3D(:,:,i) = Linhai;
end
```

D.3 Division of the cube matrices

The code used to load the data matrices into a structure of matrices, resembling a cube is listed below:

```
Div_voxelavoxel = log(MATRIZ3D_AR./MATRIZ3D);
```

D.4 Reconstruction Algorithm

The code used to obtain the reconstructed axial slices is listed below:

```
MATRIZifanbeam_IIo = zeros (342,36,500);
for t = 1:500
IR _FANBEAM = ifanbeam(Div _voxelavoxel(:,:,t), 937.5,'FanCoverage',
'cycle','FanRotationIncrement', 10 ,'FanSensorGeometry','line','Filter',
'Ram-Lak','Interpolation','linear');
end
```

This function has several entries where the following parameters can be specified: 'FanCoverage'; 'FanRotationIncrement'; 'FanSensorGeometry'; 'Filter' and 'Interpolation'

- `Div _voxelavoxel(:,:,t)` is the fan-beam projection data;
- `937.5` is the distance from the fan-beam source to the center of rotation, in pixels. Given that there are 600 pixels in the detector's length and it measures 64 cm, then for the distance from the source to the center of rotation, that is 100 cm, corresponds to 937.5 pixels;
- `'FanCoverage'` is the range of the fan-beam, and was set to `'cycle'` to establish that the rotation was accomplished through a full range [0 to 360] degrees;
- `'FanRotationIncrement'` is the fan-beam rotation angle increment, and was set for 10 degrees;
- `'FanSensorGeometry'` is the fan-beam sensor positioning, and was set to `'line'` to establish that it was a flat-panel detector and not an arc shaped detector;
- `'Filter'` is the filter used in the reconstruction, and it can be set to `'Ram-Lak'`, `'Shepp-Logan'`, `'Cosine'`, `'Hamming'` or `'Hanning'`, depending on the implementation chosen for the reconstruction;
- `'Interpolation'` is the interpolation method chosen between the parallel-beam and fan-beam data. It was set to `'linear'` for a linear interpolation or `'pchip'` for a cubic interpolation, depending on the implementation chosen for the reconstruction.

The code used to open and save each axial slice, for further image possessing and analysis, from the reconstruction is listed below:

```
imshow(IR _FANBEAM,'DisplayRange' , [min(IR _FANBEAM(:))
max(IR _FANBEAM(:))]);
Name = 'reconst _ifanbeam _%d.txt';
str = sprintf(Name,t);
csvwrite(str, IR _FANBEAM);
```

APPENDIX E

CODE SYSTEM USED IN THE VALIDATION OF THE RECONSTRUCTION ALGORITHM USING CATPHAN

E.1 Import data matrix file

To access the data matrix files where the projection data was stored, the code function `ReadXim` available online [66] was employed. The complete code system used to access the data and to transform the acquired files into a format adequate to be imported into the MATLAB workspace and the is listed:

```
cd '\home\FC\ddantonio\Desktop\730074246';
ficheiros=dir('*.xim')
for i= 1:10;
projeccao = ficheiros(i).name;
token =strtok (projeccao,'Proj_'); token2 = strtok (token, '.xim')
img00000 = ReadXim (projeccao);
value00000 = getfield(img00000,'pixel_data');
csvwrite(strcat('image','_', token2,'.txt'), value00000);
end
```

E.2 Import data into cube data matrix

The code used to load the data matrices into a structure of matrices, resembling a cube is listed below:

```
MATRIZ3D_HeadFull = zeros (1024,891,768);
for i=1:892 %i=1:321 this was applied given that file 321 was corrupted
j=i-1
Name = 'image_%05d.txt';
```

```
matrixCAT_HeadFull = sprintf(Name,j);
MatrixCAT_HeadFull =
importdata(matrixCAT_HeadFull, ',');
TraspMatrixCAT_HeadFull =
transpose(MatrixCAT_HeadFull);
MATRIZ3D_HeadFull(:,i,:) =
TraspMatrixCAT_HeadFull;
end
```

E.3 Catphan Reconstruction Algorithm

The code used to obtain each one of the reconstructed axial slices of the Catphan phantom is listed below. The code wasn't set in a loop because it was a large amount of data that was being processed what made it very time consuming. Therefore the images were reconstructed independently.

```
MATRIZifanbeamCATPHAN_HeadFull = zeros (708,708,768);
t = 1:768
ifanbeamcatphan_HeadFull = ifanbeam(MATRIZ3D_HeadFull(:,:,t),
2392.5 , 'FanCoverage', 'cycle', 'FanRotationIncrement', 0.406 ,
'FanSensorGeometry', 'line', 'Filter', 'Ram-Lak', 'Interpolation',
'linear');
imshow (ifanbeamcatphan_HeadFull(:,:,a),'DisplayRange',
[ min ( ifanbeamcatphan_HeadFull ( : ))
max ( ifanbeamcatphan_HeadFull (:)) ] );
name = 'reconstCATPHAN_ifanbeam_%d.txt';
str = sprintf(name,t);
csvwrite(str,ifanbeamcatphan_HeadFull);
```

E.4 Catphan Algorithm for information acquisition

This code was developed in order to access other content within the obtained files from the acquisition using the *Catphan 504*. This code was latter added into the loop described in D.1.

```
value00001 = getfield(img00000, 'properties');
csvwrite(strcat('image_properties','_', token2,'.txt'), value00001);
```

ANNEX I

Annex 1. List of media and their elemental compositions

For the purpose of radiation transport calculations, each organ/tissue must have a certain material composition as listed in Table I.1 and Table I.2, which is the continuation of the first. For each organ/tissue, which are a total of 53 different tissues/organs, of the adult female reference computational phantom, the elemental compositions are described and each has been assigned an ID number [53].

Table I.1: List of the elemental compositions (percentage by mass) and densities for each organ/tissue of the adult female reference computational phantom.

Medium no.		H_1	C_6	N_7	O_8	Na_{11}	Mg_{12}	P_{15}	S_{16}	Cl_{17}	K_{19}	Ca_{20}	Fe_{26}	I_{53}	Density (g.cm^{-3})
1	Teeth	2.2	9.5	2.9	42.1		0.7	13.7				28.9			2.750
2	Mineral bone	3.6	15.9	4.2	44.8	0.3	0.2	9.4	0.3			21.3			1.920
3	Humeri, upper half, spongiosa	8.7	36.6	2.5	42.2	0.2	0.1	3.0	0.3	0.1	0.1	6.2			1.185
4	Humeri, lower half, spongiosa	9.6	47.3	1.7	34.1	0.2		2.2	0.2	0.1					1.117
5	Lower arm bones, spongiosa	9.6	47.3	1.7	34.1	0.2		2.2	0.2	0.1					1.117
6	Hand bones, spongiosa	9.6	47.3	1.7	34.1	0.2		2.2	0.2	0.1					1.117
7	Clavicles, spongiosa	8.7	36.1	2.5	42.4	0.2	0.1	2.2	0.3	0.1	0.1				1.191
8	Cranium, spongiosa	8.1	31.7	2.8	45.1	0.2	0.1	3.1	0.3	0.1	0.1				1.245
9	Femora, upper half, spongiosa	10.4	49.6	1.8	34.9	0.1		3.7	0.2	0,1	0.1				1.046
10	Femora, lower half, spongiosa	9.6	47.3	1.7	34.1	0.2		0.9	0.2	0.1					1.117
11	Lower leg bones, spongiosa	9.6	47.3	1.7	34.1	0.2		2.2	0.2	0.1					1.117
12	Foot bones, spongiosa	9.6	47.3	1.7	34.1	0.2		2.2	0.2	0.1					1.117
13	Mandible, spongiosa	8.7	35.7	2.6	42.9	0.2	0.1	3.0	0.3	0.1	0.1				1.189
14	Pelvis, spongiosa	9.6	40.6	2.5	41.2	0.1		1.8	0.2	0.1	0.1				1.109
15	Ribs, spongiosa	9.7	38.1	2.8	44.5	0.1		1.4	0.2	0.2	0.1		0.1		1.092
16	Scapulae, spongiosa	9.4	40.6	2.4	40.4	0.1		2.2	0.2	0.1	0.1				1.128
17	Cervical spine, spongiosa	9.2	35.1	2.9	45.8	0.1		2.1	0.2	0.2	0.1				1.135
18	Thoracic spine, spongiosa	9.8	38.6	2.8	44.2	0.1		1.3	0.2	0.2	0.1		0.1		1084
19	Lumbar spine, spongiosa	8.8	32.9	3.0	46.6	0.1	0.1	2.6	0.3	0.1	0.1				1.171
20	Sacrum, spongiosa	10.2	41.0	2.7	43.3	0.1		0.7	0.2	0.2	0.1		0.1		1.052
21	Sternum, spongiosa	9.9	39.2	2.8	43.9	0.1		1.2	0.2	0.2	0.1		0.1		1.076
22	Humeri and femora, upper halves, medullary cavity	11.5	63.7	0.7	23.8	0.1			0.1	0.1					0.980
23	Humeri and femora, lower halves, medullary cavity	11.5	63.7	0.7	23.8	0.1			0.1	0.1					0.980
24	Lower arm bones, medullary cavity	11.5	63.7	0.7	23.8	0.1			0.1	0.1					0.980
25	Lower leg bones, medullary cavity	11.5	63.7	0.7	23.8	0.1			0.1	0.1					0.980
26	Cartilage	9.6	9.9	2.2	74.4	0.5		2.2	0.9	0.3					1.100

Table I.2: Continuation of the previous Table I.1.

Medium no.		H_1	C_6	N_7	O_8	Na_{11}	Mg_{12}	P_{15}	S_{16}	Cl_{17}	K_{19}	Ca_{20}	Fe_{26}	I_{53}	Density (g/cm^3)
27	Skin	10.0	19.9	4.2	65.0	0.2		0.1	0.2	0.3	0.1				1.090
28	Blood	10.2	11.0	3.3	74.5	0.1		0.1	0.2	0.3	0.2		0.1		1.060
29	Muscle tissue	10.2	14.2	3.4	71.1	0.1		0.2	0.3	0.1	0.4				1.050
30	Liver	10.2	13.1	3.1	72.4	0.2		0.2	0.3	0.2	0.3				1.050
31	Pancreas	10.5	15.7	2.4	70.5	0.2		0.2	0.1	0.2	0.2				1.050
32	Brain	10.7	14.4	2.2	71.3	0.2		0.4	0.2	0.3	0.3				1.050
33	Heart	10.4	13.8	2.9	71.9	0.1		0.2	0.2	0.2	0.3				1.050
34	Eyes	9.7	18.3	5.4	66.0	0.1		0.1	0.3	0.1					1.050
35	Kidneys	10.3	12.5	3.1	73.0	0.2		0.2	0.2	0.2	0.2	0.1			1.050
36	Stomach	10.5	11.4	2.5	75.0	0.1		0.1	0.1	0.2	0.1				1.040
37	Small intestine	10.5	11.4	2.5	75.0	0.1		0.1	0.1	0.2	0.1				1.040
38	Large intestine	10.5	11.4	2.5	75.0	0.1		0.1	0.1	0.2	0.1				1.040
39	Spleen	10.3	11.2	3.2	74.3	0.1		0.2	0.2	0.2	0.3				1.040
40	Thyroid	10.4	11.8	2.5	74.5	0.2		0.1	0.1	0.2	0.1			0.1	1.040
41	Urinary bladder	10.5	9.6	2.6	76.1	0.2		0.2	0.2	0.3	0.3				1.040
42	Ovaries	10.5	9.4	2.5	76.6	0.2		0.2	0.2	0.2	0.2				1.040
43	Adrenals	10.4	22.8	2.8	63.0	0.1		0.2	0.3	0.2	0.2				1.030
44	Oesophagus	10.4	22.2	2.8	63.6	0.1		0,2	0.3	0.2	0.2				1.030
45	Gall bladder, pituitary gland, trachea, thymus, tonsils, ureters	10.5	23.5	2.8	62.2	0.1		0.2	0.3	0.2	0.2				1.030
46	Uterus	10.5	28.6	2.5	57.6	0.1		0.2	0.2	0.1	0.2				1.030
47	Lymph	10.8	4.2	1.1	83.1	0.3			0.1	0.4					1.030
48	Breast (mammary gland)	11.4	46.1	0.5	42.0	0.0									1.020
49	Adipose tissue	11.4	58.9	0.7	28.7	0.1			0.1	0.1					0.950
50	Lung tissue (compressed lungs)	10.3	10.7	3.2	74.6	0.2		0.2	0.3	0.3	0.2				0.385
51	Gastro-intestinal tract-contents	10.0	22.2	2.2	64.4	0.1		0.2	0.3	0.1	0.4	0.1			1.040
52	Urine	10.7	0.3	1.0	87.3	0.4		0.1			0.2				1.040
53	Air			80.0	20.0										0.001